Photophysique des molécules polycycliques aromatiques hydrogénées d'intérêt interstellaire avec l'expérience PIRENEA

Francesca Useli Bacchitta

▶ To cite this version:

Francesca Useli Bacchitta. Photophysique des molécules polycycliques aromatiques hydrogénées d'intérêt interstellaire avec l'expérience PIRENEA. Planète et Univers [physics]. Université Paul Sabatier - Toulouse III, 2009. Français. NNT : . tel-00469704

HAL Id: tel-00469704
https://tel.archives-ouvertes.fr/tel-00469704

Submitted on 2 Apr 2010

HAL is a multi-disciplinary open access archive for the deposit and dissemination of scientific research documents, whether they are published or not. The documents may come from teaching and research institutions in France or abroad, or from public or private research centers.

L'archive ouverte pluridisciplinaire **HAL**, est destinée au dépôt et à la diffusion de documents scientifiques de niveau recherche, publiés ou non, émanant des établissements d'enseignement et de recherche français ou étrangers, des laboratoires publics ou privés.

Université Toulouse III - Paul Sabatier
U.F.R. Physique, Chimie, Automatique
THESE
presentée au Centre d'Etude Spatiale des Rayonnements par

Francesca Useli Bacchitta

pour obtenir le grade de

Docteur de l'Université de Toulouse

Délivré par: UNIVERSITE TOULOUSE III - PAUL SABATIER

Spécialité: ASTROCHIMIE EXPERIMENTALE

Photophysique des molécules polycycliques aromatiques hydrogénées d'intérêt interstellaire avec l'expérience PIRENEA

Soutenue le devant la commission d'examen

Adam WALTERS (Président)
Philippe DUGOURD (Rapporteur)
Louis D'HENDECOURT (Rapporteur)
Farid SALAMA (Rapporteur)
Giacomo MULAS (Examinateur)
Thomas PINO (Examinateur)
Christine JOBLIN (Directrice de thèse)

Ecole doctorale: SDU2E
Unité de recherche: CESR

Directeur de Thèse: Christine Joblin

T*o my parents*
To my sisters

Remerciements

Pendant ces trois ans à Toulouse j'ai eu l'occasion de rencontrer des personnes formidables qui ont contribué au bon déroulement de mon travail de thèse et qui ont enrichi, par leur présence, cette expérience en la rendant unique. Je voudrais remercier ici toutes ces personnes ainsi que tous ceux qui m'ont soutenue d'une manière ou d'une autre au cours de cette experience.

Je tiens tout d'abord à exprimer ma reconnaissance à ma directrice de thèse, Christine Joblin, pour m'avoir fait confiance tout au long de ces années, pour son enthousiasme, sa disponibilité et pour toutes ses qualités tant scientifiques que humaines. Je remercie ensuite l'ensemble de l'équipe PIRENEA au sein de laquelle mon travail s'est déroulé. En premier les membres qui n'en font plus partie mais qui m'ont beaucoup aidée, surtout au tout début de ma thèse.
Merci donc à Michel Armengaud pour sa compétence, à Patrick Frabel pour son aide et sa patience lors de nombreux tests d'axialisation (ainsi que pour m'avoir initié à l'art de la boulangerie) et merci du fond du coeur à ma Natounette chérie pour tout ce qu'elle m'a appris et pour tous les bons moments qu'on a vécu ensemble. Un énorme merci à Loïc et Anthony pour leur bonne humeur constante, leur capacité d'être très performants dans le boulot et au même temps toujours prêts à rigoler et à faire des blagues. Travailler avec vous a été un vrai plaisir! Merci à Aude pour sa gentillesse et sa disponibilité et à Baptiste pour son humour et ses précieux enseignements sur la langue française! Merci aussi à Dominique Toublanc pour l'aide qu'il m'a apporté avec le modèle Monte Carlo.

Je tiens également à remercier les membres de mon jury. Je remercie Farid Salama, Louis d'Hendecourt et Philippe Dugourd pour l'intérêt qu'ils ont porté à ce travail ainsi que pour leurs rapports, Thomas Pino pour l'ensemble de ses remarques et Adam Walters pour avoir présidé ce jury. Un merci spécial à Giacomo Mulas qui a su me pousser à entreprendre cette "aventure" et qui m'a toujours soutenue depuis mon master.

Merci aux garçons avec qui j'ai partagé le bureau 307 pendant ces trois ans: Olivier, d'abord, grâce à qui je me suis vite intégrée à la vie dans le labo, ensuite Paolo avec qui on est désormais inséparables (ou presque...) depuis le master et qui est un copain de bureau et un ami extraordinaire et merci à Julien qui contribue à la bonne humeur générale qui caractérise notre bureau. Merci aussi à Giuliano, qui a été le pionnier de la "colonie sarde" du CESR, pour ses précieux calculs et pour l'enthousiasme qu'il met dans son travail.

Je tiens encore à remercier l'ensemble du département Univers Froid qui m'a chaleureusement accueilli et où j'ai pris du plaisir à réaliser ma thèse. Plus particulièrement, merci à Claude Meny pour sa gentillesse et pour ses "bonjours en passant", à Ludo pour les soirées "musicucina", les soirées ciné et pour l'aide avec IDL, à Mauro pour égayer nos repas à la cantine et nos pauses thé avec son humour et son charme tout italien, à Ayoub pour tous les intérêts communs qu'on a pu partager (la salsa, les recettes au cumin, la peinture...) et pour être vraiment un pote super, à Jean-Philippe Bernard, Martin Giard et Emmanuel Caux pour leur soutien et leur disponibilité, à Isabelle Ristorcelli pour ses encouragements, à Anne pour sa bonne humeur débordante et aux autres filles du département, Karine, Charlotte et Sandrine, pour être toujours prêtes à offrir leur sourire ainsi que leur aide.

Merci à Max pour m'avoir remonté le moral plusieurs fois et pour m'avoir fait connaître et apprécier la musique électronique. Merci encore à tous les thésards du CESR que je n'ai pas cité avant pour avoir souvent rempli mes journées et mes soirées de bonheur avec leurs blagues, leurs sourires ou leur simple présence: Robert, Nico, Martin, Khalil, Julien, Nadège, Agnès, Renaud, Joseph, Nathalie, Damien, Céline, Benoit, Yongfen, Florent. Merci pour les mêmes raisons aux ex-thésards du labo: Bénédicte, Valerio, Christophe, Pat, Mat, Deb, Gilles, Romain, Nicolas, Pierre, Yannis, Pierrick, Philippe, Erwann, William, Denis. Merci aussi aux post-docs et CDD que j'ai pu côtoyer au sein du labo: Jonathan, Yann, Guillaume, Thomas, Renaud, Clément.

Merci à tout le personnel du CESR.

Je tiens à remercier encore tous mes amis qui m'ont donné leur support moral et affectif de loin: Serenella, Michela, Gessica, Stefano, Giannina, Nadia, Alessandro, Virginia, Fabio, Zizzu, Sebastiano et Molière.

Un grand merci à mes tantes préférées Pina e Ester, à ma marraine Rosaria et à mon parrain Mario. Merci enfin à ma famille qui constamment me supporte et m'encourage dans mes choix parfois difficiles et à laquelle je veux dédier ce travail. Grazie mamma, papà, Anna e Anto!

Contents

Remerciements **5**

Contents **7**

List of Figures **11**

List of Tables **15**

Introduction [en] **17**

Introduction [fr] **19**

1 Scientific context **21**

- 1.1 The components of the interstellar matter 21
  - 1.1.1 The gas component 22
  - 1.1.2 The dust component 23
    - 1.1.2.1 Extinction and emission of dust 24
- 1.2 Interstellar polycyclic aromatic hydrocarbons (PAHs) 25
  - 1.2.1 The PAH model 25
  - 1.2.2 Expected physical state of interstellar PAHs and observational constraints 27
  - 1.2.3 Towards the identification of interstellar PAHs 30
- 1.3 Laboratory approach 31
  - 1.3.1 Photophysics 31
  - 1.3.2 Reactivity 32
  - 1.3.3 Electronic spectroscopy 32
    - 1.3.3.1 Matrix Isolation Spectroscopy (MIS) 32
    - 1.3.3.2 Photoelectron spectroscopy (PES) 33
    - 1.3.3.3 Resonantly Enhanced Multi-Photon Ionization (REMPI) spectroscopy 33
    - 1.3.3.4 Cavity Ring-Down Spectroscopy (CRDS) 34

1.3.3.5 Dissociation spectroscopy of van der Waals PAH^+ - rare gas complexes 34
1.3.3.6 Our technique: Multiphoton dissociation spectroscopy 35
1.3.4 Vibrational spectroscopy 35
1.4 Objectives of this work 36

2 Set-up description **37**
2.1 Introduction 37
2.2 Specificities of the system 38
2.2.1 The cryogenic - ultra-high vacuum environment 38
2.2.2 The magnetic field 38
2.2.3 The ICR cell 38
2.3 Experimental procedures 41
2.3.1 Sample preparation and ion production 41
2.3.2 Trapping of ions 43
2.3.3 Description of ion motions inside the cell 44
2.3.4 Excitation and detection of ions 47
2.4 Performance of the ICR trap 49
2.4.1 Number of ions in the cell 50
2.4.2 Mass resolution and mass accuracy 51
2.4.3 Detectable mass range 52
2.5 Chemical interface 52
2.6 Photophysical interface 53
2.6.1 The Xe arc lamp 53
2.6.2 Lasers 53
2.6.2.1 The Minilite II laser (*C*ontinuum) 54
2.6.2.2 Introduction to optical parametric oscillators (O.P.O.) 54

3 Photofragmentation of isolated PAH cations **57**
3.1 Introduction 57
3.2 Study of the photodissociation pathways 58
3.2.1 Objectives 58
3.2.2 Fragmentation by multiple photon absorption 59
3.2.3 Experimental methods 59
3.3 Results 61
3.3.1 The Pyrene cation ($C_{16}H_{10}{}^+$, m/z = 202) 61
3.3.2 The Perylene cation ($C_{20}H_{12}{}^+$, m/z = 252) 63
3.3.3 The Pentacene cation ($C_{22}H_{14}{}^+$, m/z = 278) 65

3.3.4 The Naphtho[2,3-a]Pyrene cation ($C_{24}H_{14}{}^{+}$, m/z = 302) 67
3.4 Discussion 69

4 Visible photodissociation spectroscopy of PAH^{+} 73
4.1 Diffuse Interstellar Bands and PAHs: the astrophysical problem 73
4.2 Presentation of the study 74
4.2.1 Objectives 74
4.2.2 Experimental procedure 76
4.2.3 Computational details 77
4.3 Results 78
4.3.1 The pyrene cation ($C_{16}H_{10}{}^{+}$) 78
4.3.2 The 1–methylpyrene cation ($CH_3 - C_{16}H_9{}^{+}$) 79
4.3.3 The coronene cation ($C_{24}H_{12}{}^{+}$) 81
4.3.4 Simply dehydrogenated coronene cation ($C_{24}H_{11}{}^{+}$) 83
4.3.5 Doubly dehydrogenated coronene cation ($C_{24}H_{10}{}^{+}$) 85
4.3.6 Completely dehydrogenated coronene cation (C_{24}^{+}) 87
4.4 Modelling the photophysics of PAH cations 91
4.5 General remarks and astrophysical implications 97

5 Summary and perspectives 99
5.1 Summary of the results 99
5.1.1 Photofragmentation of isolated PAH ions 99
5.1.2 Visible photodissociation spectroscopy of $PAHs^{+}$ 100
5.2 Perspectives 101

Conclusions [en] 103

Conclusions [fr] 105

Bibliography 107

List of Acronyms 117

Abstract 119

Resume 121

List of Figures

1.1 Classification of interstellar cloud types (Figure taken from Snow & McCall (2006)). In the table A_V is the total visual extinction, n_H the total number density of hydrogen and f^n the local fraction of a molecule in terms of number densities (for instance f^n_{CO} = n(CO)/n_C). T(K) is the temperature of the gas. 23

1.2 Extinction curve of the diffuse ISM in the visible and UV with the contribution of three dust populations (PAHs, VSGs, BGs) derived by Désert et al. (1990). The crosses represent the observed average extinction curve of the ISM from Savage & Mathis (1979). 24

1.3 Dust emission spectrum in the IR with the contribution of each dust component (Figure taken from Désert et al. (1990)). Observations (crosses) are for the emission of the "cirrus" in the interstellar diffuse medium. 25

1.4 Diffuse Interstellar Bands (DIBs). (Figure from Draine (2003) based on Jenniskens & Désert (1994)). The values indicate the positions of the DIBs in Å. . 26

1.5 Schematic energy level diagram for a ionised PAH showing the various radiative and nonradiative channels (from Léger et al. (1989)). 27

1.6 Structures of some representative pericondensed and catacondensed polycyclic aromatic hydrocarbons. (Figure from Salama et al. (1996)). 28

2.1 Picture of the PIRENEA experimental set-up 39

2.2 Schematic view of PIRENEA 40

2.3 Representation of the ICR cell with the magnetic field oriented along the z axis. 41

2.4 Examples of different trap geometries: cubic (*a*), cylindrical (*b*) and hyperbolic (*c*). Excitation, detection and trapping plates are indicated respectively with the letters E, D and T (figure taken from Grosshans et al. (1991)). 42

2.5 Picture of the ICR cell of PIRENEA showing the different groups of electrodes. 43

2.6 Target on its metal support with a coronene deposit. 44

2.7 SIMION generated equipotential contours (red lines) of the electrostatic field inside the cylindrical ICR cell of PIRENEA. In the example shown, trapping potentials are set equal to 9 V on the external electrodes and equal to 2 V on the intermediate ones. Top: view of a longitudinal section of the cell (x-z plane). Bottom: 3D view of the section represented in the top panel. 45

2.8 ICR orbital frequency in Hz as a function of ionic mass-to-charge ratio, m/z, for different magnetic field strengths (Figure taken from Marshall et al. (1998)). . . 46

2.9 Motions followed by an ion trapped in the ICR cell. 48

2.10 Incoherent cyclotron movement of an ion packet (on the left) converted into a coherent movement (on the right) by resonant radio-frequency excitation at frequency ν_c'. 48

2.11 Example of a detection sequence: detection of coronene ions $C_{24}H_{12}^{+}$ and its ^{13}C isotopes. 50

2.12 Illustration of the relationship between the length of the transient and the resolution that can be achieved: in the top mass spectrum resolution is $\sim$ 90000 while in the bottom spectrum $\sim$12000 (Figure taken from Amster (1996)). . . . 51

2.13 Xe arc lamp spectrum between 200 and 800 nm given by the constructor. . . . 54

2.14 An optical parametric process. 55

2.15 Panther EX OPO output mean energy per pulse measured in the visible range as a function of wavelength. 56

3.1 Representation of the calculated internal energy distribution (curve a), the fragmentation rate (k_{DISS}) and the IR cooling rate (k_{IR}) for a population of anthracene cations irradiated by 1.73 eV photons. Figure adapted from Boissel et al. (1997). 60

3.2 Left panel: detection of pentacene ions, $C_{22}H_{14}^{+}$, and its ^{13}C isotopes. Right panel: isolation of $^{12}C_{22}H_{14}{}^{+}$ parent ions after ejection of the isotopes. 61

3.3 Top: FT-ICR mass spectrum of the pyrene cation after 10 s of irradiation with the Xe arc lamp. Bottom: identified pyrene photodissociation paths. 62

3.4 Normalised intensities of $C_{16}H_8{}^{+}$ (m/z = 200) and its photofragments as a function of irradiation time. 63

3.5 Top left: FT-ICR mass spectrum of the perylene cation (m/z 252) after 1 s of irradiation with the Xe arc lamp. Top right: Investigation of the fragmentation pathways of ${C_{20}H_{12}}^+$ parent ions through ejection of particular fragment ions during the lamp irradiation; FT-ICR spectrum taken after 1 s of irradiation with simultaneous ejection of the m/z = 251 ions. Bottom: FT-ICR spectrum taken after 8 s of irradiation with simultaneous ejection of the m/z = 251 and m/z = 250 ions. The m/z = 226 peak indicates the loss of an acetylene (C_2H_2) molecule from the parent ions. 64

3.6 Perylene photodissociation patterns. 65

3.7 Top: FT-ICR mass spectrum of the pentacene cation after 1 minute of irradiation with the Xe arc lamp. The zoom on the spectrum evidences the presence of two separate peaks at slightly different m/z values: m/z = 252.00 (C_{21}^+) and m/z = 252.09 (${C_{20}H_{12}}^+$). Bottom: identified pentacene photodissociation paths. . . . 66

3.8 Top: FT-ICR mass spectrum of the naphtho[2,3-a]pyrene cation after 1 minute of irradiation with the Xe arc lamp. Bottom: proposed photodissociation pathways for the naphtho[2,3-a]pyrene cation. 68

3.9 FT-ICR mass spectrum of ${C_{24}H_{14}}^+$, naphtho[2,3-a]pyrene cation, after 10 s of irradiation with the Xe arc lamp. Formation of the ${C_{22}H_{12}}^+$ fragment species is observed. 69

4.1 Electronic state peak positions and band widths of cold gas-phase PAH ions measured in the laboratory and compared to the characteristics of the strong 4428 Å DIB (Figure taken from Salama (2008)). 75

4.2 Structures of the studied molecules: (a) pyrene cation; (b) coronene cation; (c) simply dehydrogenated coronene cation; (d) doubly dehydrogenated coronene cation; (e) and (f) the two stable conformations of the 1–methylpyrene cation, each viewed from two different angles to better show the 3–D configuration of the methyl group. 76

4.3 MPD spectrum of gas-phase pyrene cation isolated in the ICR cell of PIRENEA. Computed transitions are superimposed on the experimental spectrum and represented by vertical bars with an height proportional to the computed oscillator strength. 79

4.4 MPD spectrum of gas-phase 1–methylpyrene cation measured with the PIRENEA set-up. The electronic transitions calculated for the two different isomers (e) and (f) (see Fig. 4.2) are represented in continuous and dashed lines, respectively. 80

4.5 MPD spectrum of the coronene cation measured with the PIRENEA set-up. Only the electronic transitions calculated with D_{2h} symmetry are shown. 85
4.6 MPD spectrum of the simply-dehydrogenated coronene cation measured with the PIRENEA set-up. 86
4.7 MPD spectrum of doubly-dehydrogenated coronene cation measured with the PIRENEA set-up. 87
4.8 MPD spectrum of completely dehydrogenated coronene cation measured with the PIRENEA set-up. 88
4.9 Calculated electronic transitions, with corresponding oscillator strengths, of four different isomers of ${C_{24}}^{+}$, whose geometry is represented in Fig. 4.10, which seem to be plausible structures produced in our experiment. 89
4.10 Structures and energies of the isomers of C_{24} (Figure taken from Jones & Seifert (1999)). 91
4.11 Intensity mean profiles (averaged over 50 laser shots) of the Panther EX OPO laser beam along the x and y directions measured with a LaserCam-HR beam profiler (*C*oherent) at 1 m from the laser. 93
4.12 Image of the OPO laser beam mean profile (averaged over 50 laser shots) in the x-y plane. The different colours corresponds to decreasing laser intensities going from the centre of the spot to the edges. 93
4.13 Relative dissociation counts as a function of the photon flux density obtained from the model considering different values for the absorption cross-sections, for pyrene cation (left panel) and coronene cation (right panel). 94
4.14 Photoabsorption events (abs_n is the fraction of events with n absorbed photons, abs_n+ with more than n photons) and total dissociation yield (Ydiss) calculated with the model as a function of the photon flux density. The left panel shows the results obtained for the pyrene cation for $\sigma_{abs} = 1.6 \times 10^{-16} cm^2$ while the right panel shows the results obtained for the coronene cation for $\sigma_{abs} = 0.6 \times 10^{-16} cm^2$. 95
4.15 Relative dissociation yields measured experimentally (dots) and normalised to the lowest value, compared with the results obtained from the model considering different values for the absorption cross-sections (lines), for pyrene cation (left panel) and coronene cation (right panel). 96

List of Tables

3.1 List of the fragments detected in the photodissociation cascade of each of the four considered PAH cations: pyrene ${C_{16}H_{10}}^+$, perylene ${C_{20}H_{12}}^+$, pentacene ${C_{22}H_{14}}^+$ and naphtho[2,3-a]pyrene ${C_{24}H_{14}}^+$. 72

4.1 Positions of the bands (expressed in nm) as measured in the MPD experiments with PIRENEA for the pyrene cation (${C_{16}H_{10}}^+$) and the 1-methylpyrene cation ($CH_3 - {C_{16}H_9}^+$). Band origins are identified through the comparison with the electronic transitions and the corresponding oscillator strengths (within parentheses) as computed using the split valence polarization (SVP) basis set in conjunction with the BP86 exchange-correlation functional. For comparison we list also previous experimental and theoretical data. 82

4.2 Positions of the bands (expressed in nm) as measured in the PIRENEA experiment in the wavelength range 430 - 480 nm for the coronene cation (${C_{24}H_{12}}^+$) and two of its dehydrogenated derivatives (${C_{24}H_{11}}^+$ and ${C_{24}H_{10}}^+$). Electronic transitions and the corresponding oscillator strengths (within parentheses) are computed using the split valence polarization (SVP) basis set in conjunction with the BP86 exchange-correlation functional. Previous experimental and theoretical data are reported, for comparison, in the case of coronene cation. . . . 84

4.3 Calculated electronic transitions and corresponding oscillator strengths for ten different isomers of the ${C_{24}}^+$ cation compared to the spectral features measured in the PIRENEA experiment. All the calculations are made using the split valence polarization (SVP) basis set in conjunction with the BP86 exchange-correlation functional. 90

4.4 Measurements of the dissociation yield of coronene and pyrene cations as a function of the OPO laser energy. For a given energy the mean and maximum values of the dissociation yield are calculated over a series of 20 dissociation spectra. 96

Introduction [en]

Advances in infrared and submillimetre observations have led, in recent years, to a better understanding of the composition of the interstellar matter and of the physical and chemical processes in the interstellar medium (ISM). These observations give evidence for polycyclic aromatic hydrocarbons (PAHs) being an ubiquitous component of matter in the ISM. Interstellar PAHs are key species to describe the transition between molecules and dust particles and are major actors in the physics and chemistry of the ISM.

In order to understand the formation mechanisms and the evolution of these species in astrophysical environments, combined theoretical, experimental and modelling studies are needed. From the experimental point of view these studies are challenging as they require to reproduce in the laboratory the physical conditions that prevail in the interstellar space, cold environment and absence of collisions on long time scales.

The PIRENEA experiment, installed at CESR in Toulouse, takes up this challenge combining the electromagnetic trapping and the mass spectrometry performances of an ion cyclotron resonance cell with cryogenic cooling. In addition, it presents specific interfaces for photophysical and chemical studies on molecules and nanograins of astrophysical interest.

In this thesis I have used this original set-up to study the photophysical properties of different PAHs and derivatives, with the aim to provide insight into the following questions:

- how do these species fragment when exposed to irradiation with UV photons?
- is the carbon skeleton affected by fragmentation?
- which species are the most photostable?
- what can we learn from their spectroscopic signatures?
- how can we identify PAHs in the ISM?

We are going to show to what extent PIRENEA can be used to contribute to these subjects.

Introduction [fr]

Les observations dans le domaine infrarouge et sub-millimetrique ont permis, ces dernières années, de progresser dans la compréhension de la composition de la matière interstellaire et des processus physico-chimiques qui se déroulent au sein du milieu interstellaire (MIS). Ces observations suggèrent fortement que les molécules polycycliques aromatiques hydrogénées (PAH) sont omniprésentes dans le MIS. Les PAH interstellaires sont des espèces clés dans la transition entre molécules et grains et jouent un rôle important dans la physique et la chimie du MIS. Afin de caractériser les mécanismes qui sont à la base de la formation et de l'évolution de ces espèces dans les milieux astrophysiques, il est nécessaire de combiner des études théoriques, expérimentales et des modèles de physico-chimie. D'un point de vue expérimental, cela demande de recréer en laboratoire des conditions proches de celles présentes dans le milieux interstellaires: basse température et isolation des espèces sur des échelles de temps longues.
Le dispositif PIRENEA, installé au CESR à Toulouse, a l'originalité de coupler les performances d'un instrument de spectrométrie de masse à résonance cyclotronique ionique et à transformée de Fourier avec un environnement cryogénique. Il présente de plus des interfaces spécifiques pour étudier la photophysique et la chimie de macromolécules et nanograins d'intérêt astrophysique.

Dans ce travail de thèse j'ai utilisé ce dispositif pour effectuer une étude expérimentale sur les PAH et leurs derivés, avec l'objectif d'aborder les questions suivantes:
- quelle est la fragmentation de ces espèces induite par l'irradiation avec des photons UV?
- le squelette carboné est-il affecté par le processus de fragmentation?
- quelles sont les espèces le plus resistantes à la photodissociation?
- que peut-on apprendre des signatures spectroscopiques de ces espèces?
- comment peut-on identifier les PAH dans le MIS?

Au cours de ce travail nous montrerons dans quelle mesure les expériences avec PIRENEA peuvent contribuer à apporter une réponse à ces questions.

Chapter 1

Scientific context

Inter sidera versor...
I move through stars...

The understanding of physical and chemical processes in the interstellar medium (ISM) is currently an important challenge for our knowledge of the Universe since these processes play a key role in star and planet formation and the evolution of galaxies.

At the end of its life a massive star explodes violently in a supernova event. These explosions eject large amounts of material from the interiors of stars into interstellar space and enrich interstellar matter with heavy elements produced by thermonuclear burning. Less massive stars also contribute, through stellar winds, to the enrichment of the ISM by the injection of molecules and dust, including polycyclic aromatic hydrocarbons (PAHs) that are the subject of our study. The ISM itself is, in turn, the birthplace of future generations of stars. This complex feedback involving the cycle of matter drives the evolution of our Galaxy and determines the structure, composition and observational characteristics of the interstellar matter.

1.1 The components of the interstellar matter

The ISM consists of gas (99%) and grain particles (1%) and contains about 10% of the mass of our galaxy. Its chemical composition is dominated by hydrogen (70.4% in mass) and helium (28.1%), whereas heavier elements (C, N, O, Fe, Mg, Si...) contribute for the remaining 1.5%.

1.1.1 The gas component

The interstellar gas is organised in a variety of phases characterised by different temperatures, hydrogen densities and ionisation states. Early models, McKee & Ostriker (1977), classify the ISM into three phases: the cold neutral medium (CNM), the warm ionised or warm neutral medium (WIM or WNM) and the hot ionised medium (HIM), which is sometimes referred to as the intercloud medium or the coronal gas. These phases appear to contain a variety of cloud types, spanning a wide range of physical and chemical conditions. The table reported in Fig. 1.1 summarises the classification of the different cloud types proposed by Snow & McCall (2006). We can distinguish:

- **Diffuse clouds**: these are the most tenuous clouds, fully exposed to the interstellar radiation field. Typical temperatures are in the range 30-100 K. In diffuse *atomic* clouds hydrogen is mainly in neutral atomic form and atoms with ionisation potentials less than that of hydrogen (e.g. carbon) are almost fully ionised providing abundant electrons. Nearly all molecules are quickly destroyed by photodissociation in these clouds so very little chemistry occurs.
  In diffuse *molecular* clouds, instead, the radiation field is sufficiently attenuated to have a substantial fraction of hydrogen in molecular form ($\mathrm{f}^{\mathrm{n}}_{\mathrm{H}_2} > 0.1$). Enough interstellar radiation is however present to ionise atomic carbon or photodissociate CO so that carbon is predominantly still in the form of C^+. Small molecules, like for instance CO, CH, CN, C_2, C_3, are observed in these clouds.

- **Translucent clouds**: in these clouds C^+ is no longer the dominant form of carbon which is mostly present in neutral atomic or molecular form. They can represent the outer edges of dense molecular clouds and their characteristics (temperature, density) fall in between diffuse and dense molecular clouds.

- **Dense molecular clouds**: densest regions of the ISM ($10^4 - 10^6$ cm^{-3}) in which H_2 is the dominant molecular species. The reactive C is replaced by the stable CO, which is commonly used to trace the interstellar molecular gas. Star formation occurs within these regions as a natural consequence of their high densities and low temperatures (10-50 K). These clouds offer also a UV-shielded environment for the formation and survival of complex molecules. Many of the approximately 150 currently known interstellar molecules were found through observations of microwave rotational transitions in such clouds.

Other regions exist among the above described environments. HII regions, for example, are regions in which hydrogen is ionised and has a temperature of about 10^4 K. They are formed by

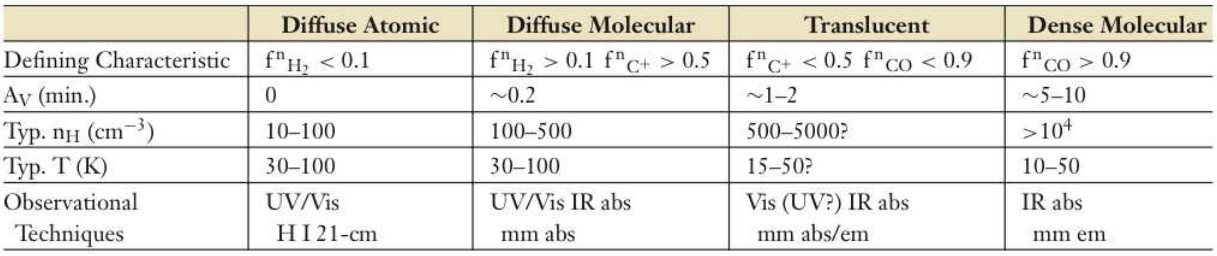

	Diffuse Atomic	Diffuse Molecular	Translucent	Dense Molecular
Defining Characteristic	$f^n{}_{H_2} < 0.1$	$f^n{}_{H_2} > 0.1$ $f^n{}_{C+} > 0.5$	$f^n{}_{C+} < 0.5$ $f^n{}_{CO} < 0.9$	$f^n{}_{CO} > 0.9$
A_V (min.)	0	~0.2	~1–2	~5–10
Typ. n_H (cm^{-3})	10–100	100–500	500–5000?	$>10^4$
Typ. T (K)	30–100	30–100	15–50?	10–50
Observational Techniques	UV/Vis H I 21-cm	UV/Vis IR abs mm abs	Vis (UV?) IR abs mm abs/em	IR abs mm em

Figure 1.1: Classification of interstellar cloud types (Figure taken from Snow & McCall (2006)). In the table A_V is the total visual extinction, n_H the total number density of hydrogen and f^n the local fraction of a molecule in terms of number densities (for instance $f^n{}_{CO} = n(CO)/n_C$). T(K) is the temperature of the gas.

young massive stars that emit large amounts of UV photons beyond the Lyman limit ($h\nu > 13.6$ eV) ionising and heating their surroundings. As such they can be considered signposts of sites of massive star formation in the Galaxy.
Other interesting environments are the so-called photodissociation regions (PDRs, sometimes also called photon-dominated regions). The term PDRs is used nowadays to designate all regions of the ISM where far-ultraviolet (FUV) photons dominate the physical and chemical processes. In these regions penetrating FUV photons (with energies between 6 and 13.6 eV) dissociate and ionise molecular species. They are well observed near bright stars.

1.1.2 The dust component

Dust is formed at high densities and high temperatures in the envelopes of evolved stars. The interstellar dust component embodies only 1% of the interstellar medium mass but it plays a key role through its effects on radiation, heating the gas by photoelectric effect and acting as catalyst for the formation of molecules. There is some direct and indirect evidence for the existence of small solid particles in the ISM. Direct evidence is supplied by the observation of the increasing extinction of radiation coming from stars with the path length through the ISM and by the observation of thermal infrared emission. Indirect evidence is provided by data on the abundance of elements in the interstellar gas showing that the elements that are most likely to form refractory solids are generally underabundant with respect to solar values. The dust absorbs UV-visible light coming from stars and re-emit it in the infrared. Due to strong absorption bands in the Earth atmosphere, only a few spectral windows in the IR can be observed with ground-based telescopes and most of the available information in this spectral range comes from space telescopes.

1.1.2.1 Extinction and emission of dust

In the model of Désert et al. (1990), three main dust components have been identified to account for both the extinction curve (cf. Fig. 1.2) and the IR emission features (cf. Fig. 1.3):

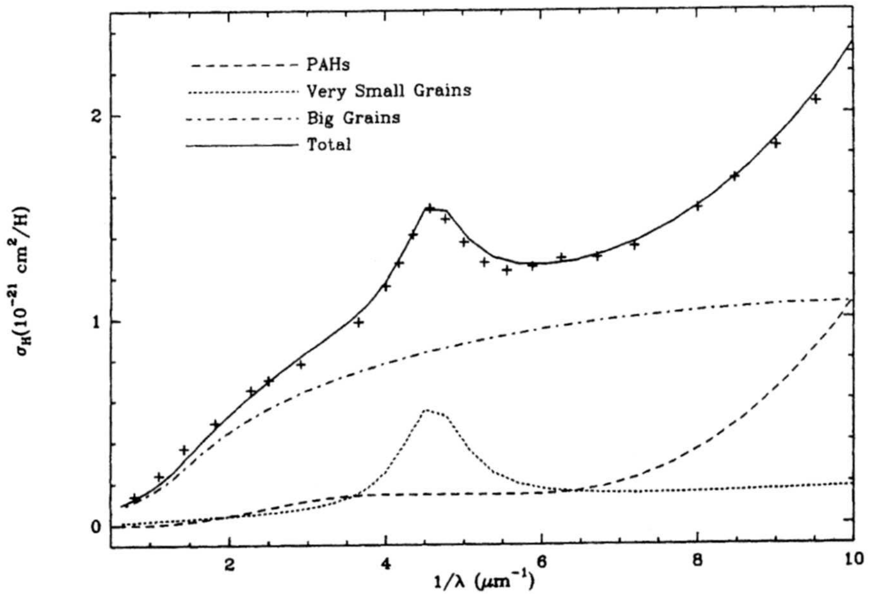

Figure 1.2: Extinction curve of the diffuse ISM in the visible and UV with the contribution of three dust populations (PAHs, VSGs, BGs) derived by Désert et al. (1990). The crosses represent the observed average extinction curve of the ISM from Savage & Mathis (1979).

1. Big Grains (BGs): mainly silicate grains ($\sim 0.1\mu$m) which dominate the far-IR to submillimeter emission in our Galaxy;
2. Very Small Grains (VSGs): carbon-based nanoparticles that are responsible for the continuum emission between 20 and $\sim$ 80 μm;
3. Polycyclic Aromatic Hydrocarbons (PAHs): large aromatic molecules composed of carbon rings saturated with hydrogen atoms responsible for the mid-IR emission. These molecules can reach a size of a few nanometers and are stochastically heated (undergo fluctuations in their temperature) upon the absorption of a single UV photon. Désert et al. (1990) attributed to PAHs the far-UV rise of the extinction curve (cf. Fig. 1.2). Laboratory measurements suggest that PAHs contribute also to the so called UV "bump" (Joblin et al. 1992).

This dust model has been improved, in recent years, thanks to the studies performed by Draine & Li (2001, 2007).

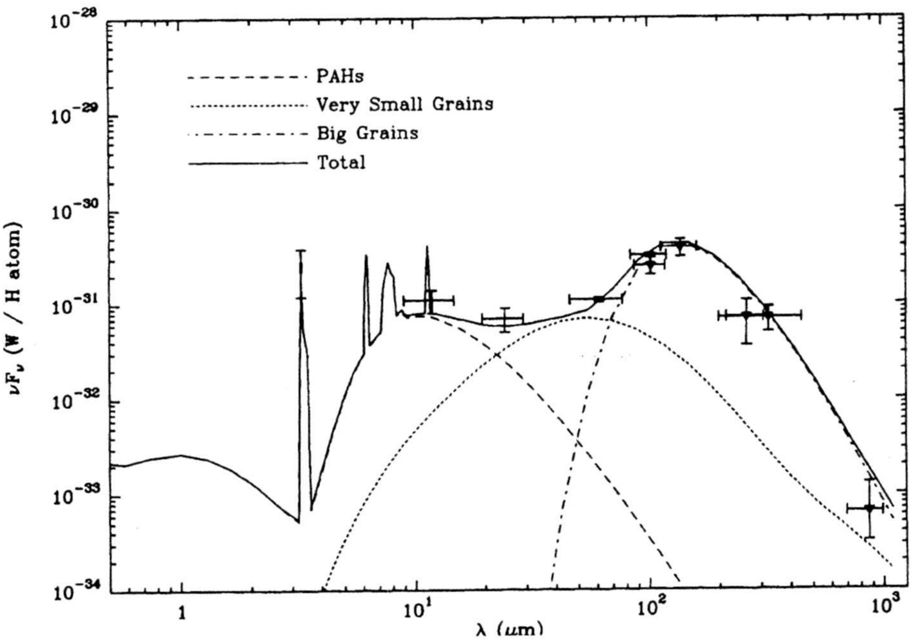

Figure 1.3: Dust emission spectrum in the IR with the contribution of each dust component (Figure taken from Désert et al. (1990)). Observations (crosses) are for the emission of the "cirrus" in the interstellar diffuse medium.

The visible extinction curve also shows weak fine structures, called the diffuse interstellar bands (DIBs) (cf. Fig. 1.4), which span the wavelength range from the near UV ($\sim$ 0.4 μm) to the near infrared ($\sim$ 1.3 μm) (Herbig 1995). Historically they are called "diffuse" because of their widths (typically between 0.4 and 40 Å), that are broad compared to the narrow atomic lines. Here again PAH molecules are considered as good candidates to account at least for some of the DIBs (see chapter 4).

1.2 Interstellar polycyclic aromatic hydrocarbons (PAHs)

1.2.1 The PAH model

The presence of PAHs in astrophysical environments was proposed by Léger & Puget (1984) and Allamandola et al. (1985) to account for the so-called unidentified infrared (UIR) bands, a set of emission bands observed in many dusty environments excited by UV photons whose major features are located at 3.3, 6.2, 7.7, 8.6, 11.3 and 12.7 μm. These bands are attributed to the vibrations of aromatic C–H and C–C bonds, for this reason they are also called aromatic

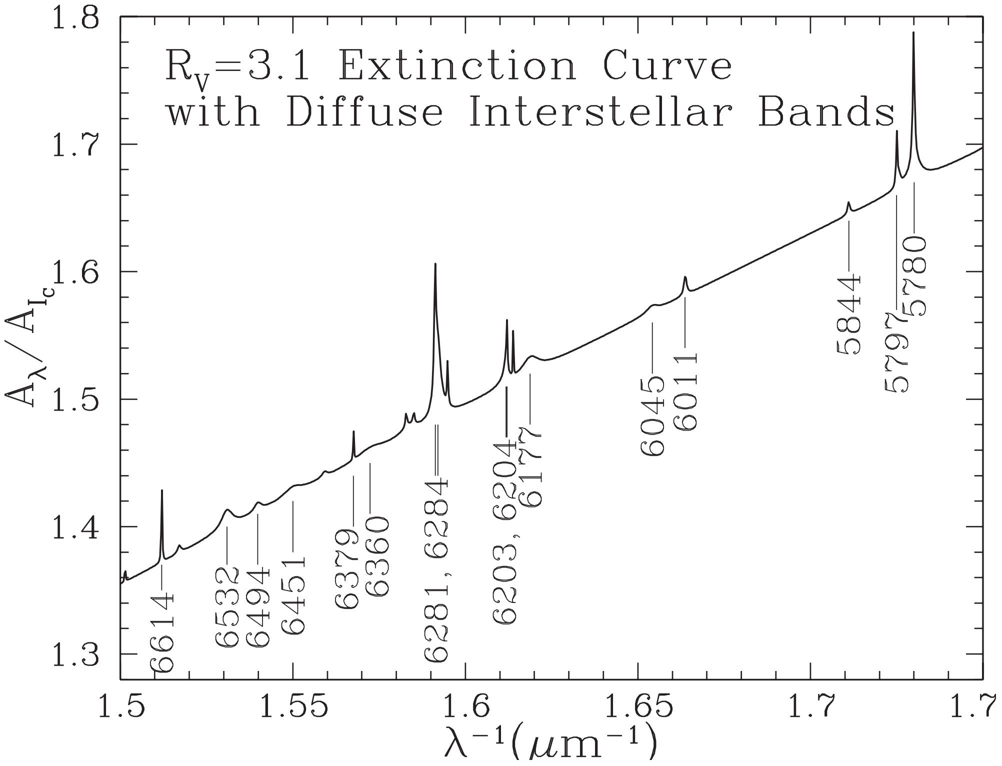

Figure 1.4: Diffuse Interstellar Bands (DIBs). (Figure from Draine (2003) based on Jenniskens & Désert (1994)). The values indicate the positions of the DIBs in Å.

infrared bands (AIBs). The emission mechanism at the origin of these bands is a stochastic heating process as initially proposed by Andriesse (1978) and Sellgren (1984). The molecules reach high temperatures after the absorption of a single UV photon and then cool down through the emission of IR photons giving rise to the AIBs.

PAH emission mechanism

The absorption of a UV photon corresponds to an electronic transition between the electronic ground state and an excited electronic state. Fig. 1.5 represents the case of an ion which is relevant for PAH molecules because these species are expected to be at least partly ionised in the astronomical environments where they are observed (Allamandola et al. 1985; D'Hendecourt & Léger 1987; Omont 1986). The electronic states are doublets (D_0, D_1, D_2...) in the case of fully hydrogenated cation species but partially hydrogenated ones (radicals) can have higher multiplicity. This electronic excitation can be followed by a variety of de-excitation processes:

- ionisation

- photodissociation
- electronic radiative transitions, either fluorescence when they take place between states of the same multiplicity or phosphorescence between states of different multiplicity
- IR emission ($t_{1/2} \sim 5$ s).

In general, the electronic excitation is isoenergetically converted in a very short time ($10^{-12} - 10^{-8}$ s) into a highly vibrationally excited level of the electronic ground state (process called internal conversion, IC). Fast ($10^{-12} - 10^{-10}$ s) internal vibrational redistribution (IVR) leads then to a statistical distribution of the energy between the vibrational modes and the slow IR emission takes place (Léger et al. 1989).

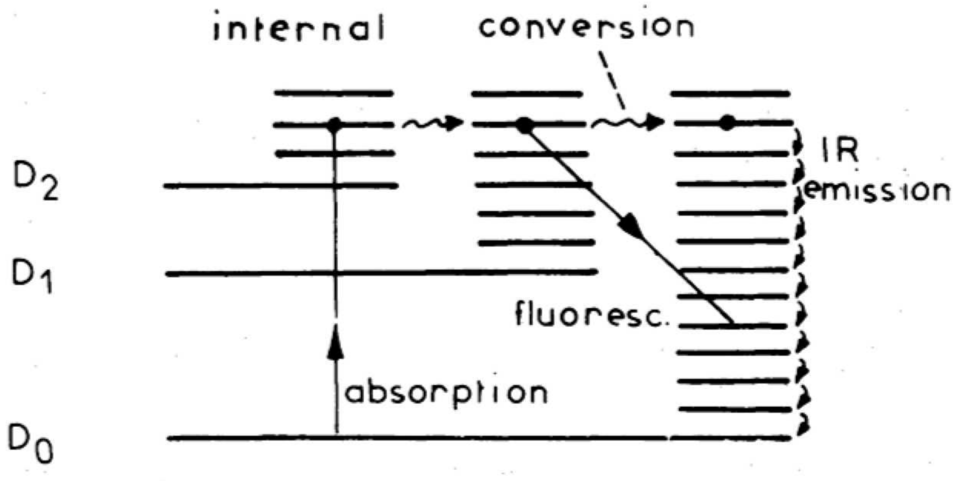

Figure 1.5: Schematic energy level diagram for a ionised PAH showing the various radiative and nonradiative channels (from Léger et al. (1989)).

1.2.2 Expected physical state of interstellar PAHs and observational constraints

PAHs can be divided into two main classes: pericondensed (compact structure) and catacondensed PAHs (more open structure). The class of pericondensed PAHs contains C atoms that are members of three separate rings (e.g. coronene). If, on the contrary, no C atom in the PAH belongs to more than two rings, the PAH is classified as catacondensed (cf. Fig. 1.6).

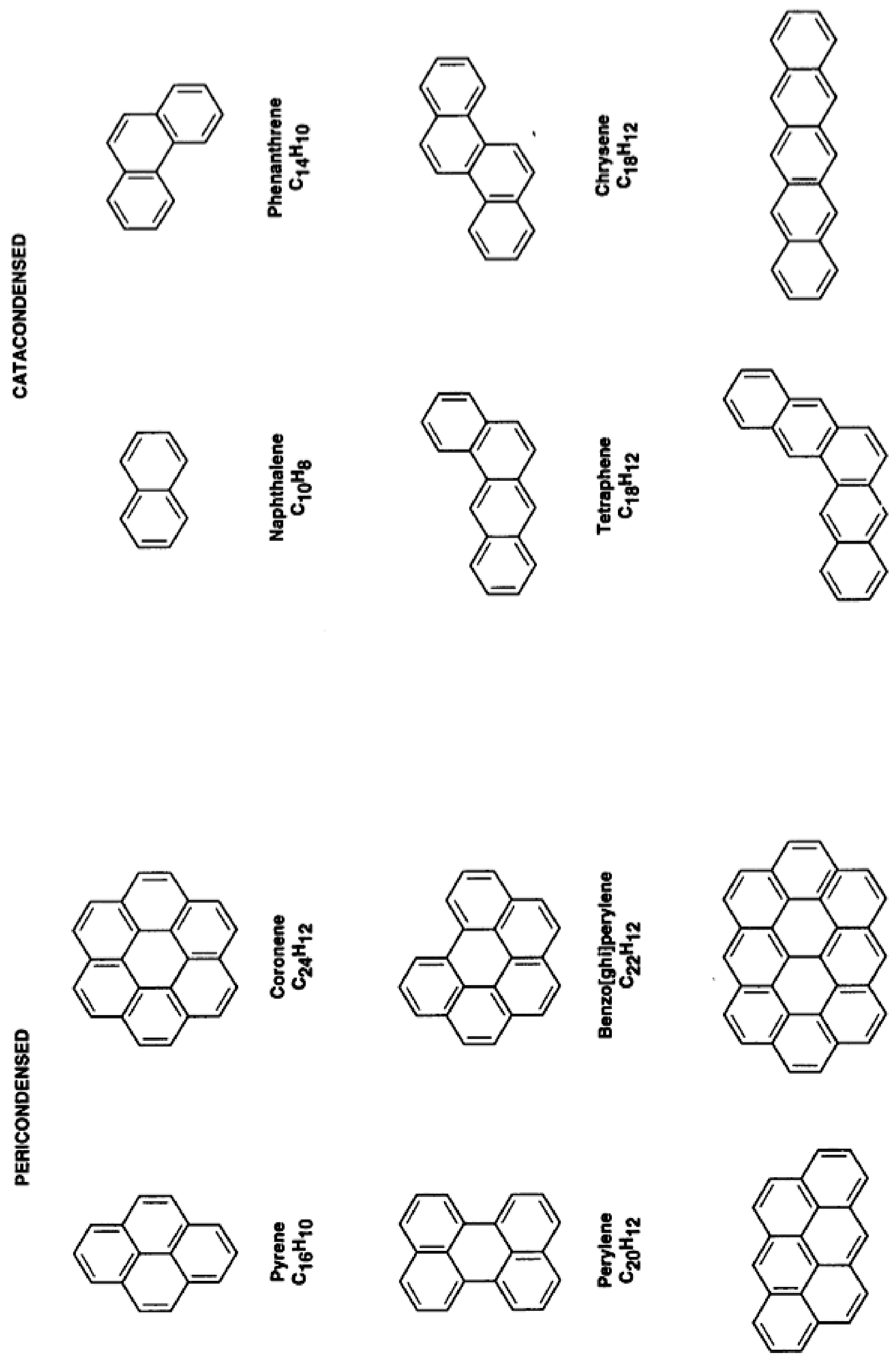
CATACONDENSED
Naphthalene
$C_{10}H_8$
Phenanthrene
$C_{14}H_{10}$
Tetraphene
$C_{18}H_{12}$
Chrysene
$C_{18}H_{12}$
Pentaphene
$C_{22}H_{14}$
Pentacene
$C_{22}H_{14}$
PERICONDENSED
Pyrene
$C_{16}H_{10}$
Coronene
$C_{24}H_{12}$
Perylene
$C_{20}H_{12}$
Benzo[ghi]perylene
$C_{22}H_{12}$
Antanthrene
$C_{22}H_{12}$
Ovalene
$C_{32}H_{14}$

Figure 1.6: Structures of some representative pericondensed and catacondensed polycyclic aromatic hydrocarbons. (Figure from Salama et al. (1996)).

PAHs are estimated to account for a substantial fraction of the total interstellar carbon budget (up to 20% according to Joblin et al. (1992)) and are seen as an intermediate stage between the gas and dust carbon phases of interstellar matter. They are expected to exist in a wide variety of environments, in a complex statistical equilibrium of different charge and hydrogenation states (Joblin et al. 1996b; Bakes et al. 2001a,b; Le Page et al. 2001, 2003). Observational studies on PDRs by Rapacioli et al. (2005) and Berné et al. (2007), in particular, have evidenced that the mid-IR emission in these regions can be accounted for by three different populations, namely neutral PAH^0, cationic PAH^+ and VSGs. It was suggested that VSGs are in fact made of PAHs in a condensed form, and that these VSGs are photodestroyed at the surface of UV-irradiated clouds. PAH clusters were investigated as plausible candidates for these VSGs by Rapacioli et al. (2006).

The previous observational studies also imply that free PAHs are only present at the surface of clouds, which is consistent with previous studies (Bernard et al. 1992; Boulanger et al. 1990). The spectral decomposition between PAH^0 and PAH^+ from Rapacioli et al. (2005) was used by Flagey et al. (2006) to analyse the galactic diffuse ISM emission and derive a fraction of 50% of PAH cations in this medium. The ionisation state of these species is governed by the "ionisation parameter", $\gamma = G_0\sqrt{T}/n_H$, with G_0 the intensity of the UV radiation field in Habing's units, T the gas temperature and n_H the total hydrogen nuclei density (Tielens 2005). PAHs are also expected to contribute to the heating of the gas through photoelectric effect (Verstraete et al. 1990; Bakes & Tielens 1994).

The population of PAHs is expected to include derivatives such as dehydrogenated and hydrogenated species and PAHs with substituents at the periphery (see for instance Joblin et al. (1996a); Bernstein et al. (1996)). The composition and structure of PAHs can reflect, in a more complicated way, the history of formation and processing of these species.

The size of interstellar PAH molecules is still unclear. Allain et al. (1996) derived a minimum size of about 50 carbon atoms for interstellar PAHs based on the loss of C_2H_2 whereas Hudgins & Allamandola (1999) have proposed that PAHs with 50-80 carbon atoms dominate the mid-IR emission. Geballe et al. (1994) derived a size of 60 carbon atoms based on the observation of the overtone of the 3.3 μm band observed at 1.68 μm. Studies testing the photo-physical stability of PAHs have pointed to the presence of even larger molecules depending on the surrounding environments (Schutte et al. 1993; Le Page et al. 2003).

PAHs are thought to be formed in the outflows of evolved carbonaceous stars, however the detailed mechanisms leading to their formation and growing are not well understood yet. Some studies suggest that the pyrolysis of hydrocarbon molecules can lead to the formation of PAHs in a process analogous to soot formation in combustion processes (Frenklach & Feigelson 1989; Cherchneff et al. 1992). They could also be formed from the fragmentation of C dust particles in shocked regions and from photosputtering in diffuse IS clouds (Scott et al. 1997). Cernicharo et al. (2001) have suggested that photon-driven polymerisation of acetylene could lead to the formation of benzene (C_6H_6). Other observational studies have also emphasised that PAHs are efficiently produced by UV destruction of VSGs in photo-dissociation regions (Rapacioli et al. 2005; Berné et al. 2007).

Concerning destruction, photofragmentation by UV radiation is considered as the main destruction process for PAH molecules (Allain et al. 1996). This process has been proposed in PDRs as a mechanism for the production of small hydrocarbons (Pety et al. 2005).

1.2.3 Towards the identification of interstellar PAHs

The identification of interstellar PAHs relies on the match between their spectroscopic fingerprints and the astronomical spectra. The radio range is commonly used to identify new molecules but, unfortunately, PAHs are usually very symmetrical and present very low (or zero) permanent dipole moments, therefore they do not have a pure rotational spectrum. An exception is corannulene, $C_{20}H_{10}$, which has a large dipole moment of 2.07 D. This species has recently been searched for using the IRAM 30 m radiotelescope. An upper limit for the fraction of carbon locked in corannulene of about 1.0×10^{-5} , relative to the total abundance of carbon in PAHs, has been obtained by Pilleri et al. (2009).

Transitions in the region of the AIBs, near and medium-IR, reflect mainly the vibrations of C–H and C–C chemical bonds so they are common to the whole class of PAHs. The observed spectra in this range likely result from the emission of a mixture of PAH molecules, therefore they are not suited to identify individual species. Spectral features in the far-IR range, on the other hand, are much more specific to the exact molecular identity (Joblin et al. 2002; Mulas et al. 2006; Mattioda et al. 2009). These bands arise at the end of the cooling cascade of the UV-excited molecules and contain the low-frequency vibrational modes associated with collective oscillations of the carbon skeleton. These far-IR bands will be searched for by the recently launched Herschel Space Observatory.

It should be also possible to identify PAHs through their electronic transitions in the near-UV to near-IR ranges as carriers of some of the DIBs. Several laboratory measurements have been performed on PAH cations in an attempt to identify among them the DIB carriers (see for instance Salama et al. (1999) and Halasinski et al. (2005)). The search for the identification of individual PAH molecules has not been successful so far. Only Iglesias-Groth et al. (2008) recently claimed a tentative identification of ionised naphthalene, ${C_{10}H_8}^+$, along one line of sight in the ISM. The number of species that has to be considered is extremely large as the electronic spectrum is quite sensitive to the molecular structure (for instance different degrees of hydrogenation have to be studied for a given carbon skeleton), so it would be impractical to perform laboratory measurements on all of the possible species. Before selecting the most appropriate candidates for their study as potential DIB carriers, it is useful to analyse the physical and chemical properties of PAH cations in order to predict which of these species are most likely to survive in the interstellar environments where the DIBs are formed.

An important step to accomplish is then to understand the nature of PAHs: where they come from and how they evolve due to environmental conditions (UV irradiation, gas and dust interactions). To provide such information a detailed modelling of the photophysics of these species is mandatory. This modelling requires experimental studies and complementary theoretical studies to get an accurate description of the different processes involved such as the absorption of UV photons, the photofragmentation and the IR emission. These requirements lead to fundamental studies on laboratory analogues of interstellar PAHs and the development of specific laboratory set-ups, such as the PIRENEA experiment, that has been used in this work.

1.3 Laboratory approach

To characterise the properties of analogues of interstellar PAHs and related species, laboratory experiments try to reproduce the physical conditions prevailing in interstellar space: cold environment (10 - 50 K), very low densities (50 to 10^6 species / cm^3) and presence of UV photons ($h\nu \leq 13.6$ eV). We can distinguish three main kind of laboratory studies that have been performed so far on PAHs for applications in astrochemistry: i) experiments on the photophysics (involving study of the radiative exchanges, IR emission, photodissociation...), ii) reactivity experiments, iii) spectroscopic studies.

1.3.1 Photophysics

Because of the isolation conditions present in space, processes that occur on long time scales are of prime interest when studying interstellar molecules, in particular slow IR emission and photofragmentation at the dissociation threshold. These processes are difficult to study in many experimental set-ups due to the presence of collisions or to the lifetime intrinsic to the technique. In experiments with molecules travelling in jets, for instance, species can be fully isolated only for milliseconds. Face to these difficulties different trapping techniques have been developed in the last years. In the present work we make use of a technique called Fourier transform ion cyclotron resonance mass spectrometry (FT-ICR MS), discussed in detail in the following chapter, to study the photodissociation of several PAH cations. A review of previous photodissociation / photostability studies performed so far on PAHs will be presented in chapter 3.

1.3.2 Reactivity

To understand the chemistry of PAHs it is necessary to study experimentally and theoretically reactions of these species with atoms, radicals and molecules involved in the chemistry of astrophysical environments. The selected ion flow tube (SIFT) technique allows the study of the reactivity of positive or negative ions with atoms and molecules under thermalised conditions over a wide range of temperature. PAH / gas reactions have been studied with this method by Le Page et al. (1999) and Betts et al. (2006).

Another method to investigate chemical reactions taking place at the very low temperatures of molecular clouds, is the CRESU (Cinétique de Réaction en Ecoulement Supersonique Uniforme) technique. This latter involves the expansion of a gas or mixture of gases through a Laval nozzle from a high pressure reservoir into a vacuum chamber. As it expands, the nozzle collimates the gas into a supersonic beam, which is axially and radially uniform in temperature, density and velocity. The density of the flow ($10^{16} - 10^{18} cm^{-3}$) is large enough to ensure local thermal equilibrium This technique has been used to study the reactivity of the anthracene ion ($C_{14}H_{10}{}^{+}$) with OH and CH radicals by Goulay et al. (2005, 2006).

Reactivity studies have been performed also using ion trap techniques. Keheyan (2001) has studied the reactivity at room temperature of naphtalene ($C_{10}H_8{}^{+}$), pyrene ($C_{16}H_{10}{}^{+}$) and coronene ($C_{24}H_{12}{}^{+}$) radical cations and derivatives with small molecules of interstellar interest. Recently the reactivity of dehydrogenated coronene cation ($C_{24}H_{11}{}^{+}$) with H_2O molecules at low temperatures (between 30 and 300 K) has been investigated by Bruneleau (2007) using the PIRENEA set-up.

1.3.3 Electronic spectroscopy

Spectroscopic signatures are the only direct diagnostics to identify the presence of a particular species in interstellar space. The second part of this work focuses on the visible spectroscopy of ionised PAHs so we summarise here the main spectroscopic techniques that have been developed and used so far on PAHs to study their electronic properties either in the solid or in the gas phase. Each one of these techniques presents its specificities, advantages and limitations so they can be considered complementary to each other in the information they provide.

1.3.3.1 Matrix Isolation Spectroscopy (MIS)

In this technique, molecules are co-deposited at low temperature (4-10 K) with rare gas atoms. When dilution is high, molecules are well separated and have no short range interaction one with another (Joblin et al. 1995). This allows the simulation of the cold temperatures and isolation conditions present in space. Among the rare gases commonly used as matrix-cage materials

(Ne, Ar, Kr and Xe), solid neon provides the best (less polarizable) medium for the study of the electronic spectra of ions (Salama & Allamandola 1991).

Many PAH cation absorption spectra have been obtained so far using matrix isolation spectroscopy (MIS) (Salama et al. 1994; Szczepanski et al. 1995; Ruiterkamp et al. 2002). Two major limitations must, however, be taken into account with the MIS data: spectral shifts and band broadening induced by the interaction with the matrix and the difficulty to control the species that are present in the matrix.

The predicted limit for the neon-matrix to gas-phase shift is $\sim$ 0.5% in energy (Romanini et al. 1999; Salama et al. 1999). Shifts and broadenings are therefore a minor problem in infrared spectra while in the UV-visible range, where the energies involved are higher, matrix-induced perturbations are stronger. Another concern is related to the procedure that is usually applied to produce ions in the matrix. It consists in irradiating the deposit made of PAHs and rare-gas atoms with a VUV source. This results in the production of cations but other fragment species could be produced as well. The MIS technique has the advantage of being quite easy to perform and remains essential for selecting species which are the most promising interstellar candidates.

1.3.3.2 Photoelectron spectroscopy (PES)

This is the first technique that has been used to obtain some information on the electronic transitions of cations. The energy of an electronic state can be related to the kinetic energy of the photoelectrons emitted by photoionisation of the neutral precursor. Conservation of energy then requires that :

$$E(A) + h\nu = E(A^+) + E_c$$

where E(A) and E(A^+) are respectively the energies of the neutral and ionised molecules, $h\nu$ is the photon energy and E_c the kinetic energy of the emitted photoelectron. The number of emitted photoelectrons as a function of their kinetic energy can be measured using any appropriate electron energy analyser and a photoelectron spectrum can thus be recorded. Photoelectron spectroscopy (PES) has been extensively applied to study PAHs mainly in the seventies (Schmidt 1977; Bosci et al. 1974; Maier & Turner 1972). One of the major limitations of this technique is the low resolution on the photoelectron kinetic energy, typically in the order of $\sim$ 100 cm^{-1}. The method used to produce neutral species can also limit the attainable spectral resolution.

1.3.3.3 Resonantly Enhanced Multi-Photon Ionization (REMPI) spectroscopy

A REMPI experiment uses two lasers applied in sequence. The first laser promotes the molecules of interest into an excited intermediate electronic state, a second probe laser is then used to ionize the excited species. Mass spectrometry is generally used to identify the produced species. To achieve low temperatures, the molecules can be produced in a supersonic expansion.

REMPI provides spectroscopic information that can be unavailable to single photon spectroscopic methods (cf. Hager & Wallace (1988)), however, only neutral species with suitable excited electronic states can be detected. The spectra of different PAH species have been measured with this technique (Güthe et al. 2001; Kokkin et al. 2008).

1.3.3.4 Cavity Ring-Down Spectroscopy (CRDS)

CRDS is based on the measurement of the exponential decay, $I_0\ exp(-\gamma t)$, or "ring down", of photons trapped inside an optical cavity. The ring down rate, γ, is proportional to the cavity losses per round trip. A pulsed laser is normally used to inject photons in the cavity by transmission through one of the mirrors and the photon ring down is monitored by detecting the light leaking out through the other cavity mirror. As the laser wavelength is tuned, measuring the ring down rate allows a direct determination of the sample absorption (Romanini et al. 1997, 1999). The high sensitivity of this method rests upon the long residence time of the photons inside the cavity. Another important feature of CRDS is that it is insensitive to the large intensity fluctuations typical of pulsed lasers.

CRDS measurements are often combined with a jet expansion to achieve low molecular temperatures by cooling down the molecular vibrational and rotational degrees of freedom. They provide electronic spectra of cold isolated gas phase cations that can be directly compared to astronomical observations (Biennier et al. 2003; Biennier 2004; Sukhorukov et al. 2004; Tan & Salama 2006).

1.3.3.5 Dissociation spectroscopy of van der Waals PAH^+ - rare gas complexes

This technique consists in studying the dissociation spectrum of van der Waals (vdW) complexes PAH^+-rare gas produced in a supersonic molecular beam. The recording of the spectra involves the use of a multiphoton laser ionization step, of a second delayed laser pulse to excite electronic transitions in the ionised complex and of a time of flight (TOF) mass spectrometer to detect the PAH^+ fragment produced by ejection of the rare gas atom. The recording of this PAH^+ fragment ion signal versus the visible laser wavelength, while scanning it, provides the action spectrum of the complex cation at low temperature because of the low binding energy of the complex. This spectrum differs however from the spectrum of PAH^+ by a small vdW red-shift.

This method has been successfully applied for the study of several PAH cations (Pino et al. 1999, 2001, 2007; Bréchignac & Pino 1999; Bréchignac et al. 2001; Boudin et al. 2001).

1.3.3.6 Our technique: Multiphoton dissociation spectroscopy

Another approach to study PAH cation spectroscopy in the gas-phase is the coupling of an ion trap, where ions can be easily collected and thermalised, with multiphoton dissociation (MPD) spectroscopy. Molecular ions are formed *in situ* from the neutral precursors in an isolated environment and mass-selected, thus removing any ambiguity on the identity of the recorded species, with the exception of possible simultaneously produced isomers which are not distinguishable with mass spectrometry. The technique is based on the fragmentation of a specific cation by multiphoton absorption. Fragmentation occurs when the laser wavelength is tuned on an absorption band, the obtained action spectrum (ion yield as a function of the laser wavelength), can then be related to the absorption spectrum of the ionic species.

Compared to the previous technique, this one offers the advantage of studying directly the species of interest (not a complex). The disadvantage is that a chemical bond has to be broken and this requires significant energy that leads to hot dissociating ions. It also requires powerful multiphoton sources, especially in the IR where free electron lasers have to be used. In the visible spectral range, Rolland et al. (2003) have performed MPD spectroscopy of the phenanthrene and anthracene cations.

1.3.4 Vibrational spectroscopy

It is worth to mention here also some of the numerous studies performed to characterise the PAH absorption and emission spectra in the IR in the attempt to reproduce the AIB interstellar features. The IR spectra of several neutral PAHs have been studied by Kurtz (1992) and Joblin et al. (1994, 1995) in the gas phase. Most available IR spectra, however, come from laboratory experiments in cold solid inert-gas matrices (cf. for instance Szczepanski et al. (1992), Szczepanski & Vala (1993), Hudgins & Allamandola (2000), Mattioda et al. (2005)).

As explained above, the major limitation of this technique is the interaction of species with the atoms of the matrix, that induces spectral shifts. Furthermore the low temperatures (4K in Ne, 10K in Ar matrices) do not allow emission measurements.

Absorption IR spectra of PAH cations isolated in an ion trap have also been measured using multiphoton dissociation technique at the FELIX facility (Free Electron Laser for Infrared Experiment) by Oomens et al. (2006, 2000, 2001, 2003).

The best approach to study the IR spectroscopy of PAHs in the laboratory for astrophysical applications should be to record their IR emission following the absorption of UV photons. Very few studies have been performed so far on the IR emission spectra of excited PAHs (Shan et al. 1991; Brenner & Barker 1992; Cook et al. 1998; Kim & Saykally 2003), and none of them provides well-characterised excitation conditions. Such experiments remain challenging.

1.4 Objectives of this work

The aim of this work is to meet the two following targets:

- provide information on the behaviour of PAHs under UV photon irradiation;
- characterise the visible spectroscopic properties of several PAH cations and derivatives as an identification tool of these molecules in space;

Both studies have been carried out using the PIRENEA experiment that provides the possibility to isolate gas-phase ions in physical conditions that mimic those found in interstellar space. After a description of the PIRENEA set-up and its main characteristics in the second chapter, the manuscript will be divided into two parts. The first part is devoted to the study of the photodissociation cascade of different PAH cations. The general question is which are their main dissociation channels and how the photodissociation process contributes to the production of smaller species such as small hydrocarbons and carbon chains. The results of these experiments can provide guidelines to infer which type of hydrocarbon species can be searched for in the interstellar medium.

In the second part of the manuscript, the visible spectroscopy of several gas-phase PAH cations and derivatives is studied. Due to the low density of trapped ions, a MPD technique is used to indirectly obtain the visible absorption spectrum of these species. The validity of our experimental method is confirmed by comparison with available gas-phase spectra of cold PAHs. Theoretical calculations and modelling are also used to complement experimental data.

The last chapter finally summarises the main results and presents some perspectives.

Chapter 2

Set-up description

Quidquid agis, prudenter agas et respice finem!
Whatever you do, do it wisely and consider the goal!

2.1 Introduction

PIRENEA (Piège à Ions pour la Recherche et l'Etude de Nouvelles Espèces Astrochimiques) is an original home-built experimental set-up conceived to perform photo-physical and chemical studies on large molecules and nano-sized particles of astrophysical interest in isolation conditions approaching those of interstellar space in terms of collisions and interactions with photons (i.e. low temperatures (10-50 K), low density (50 to 10^6 species/cm^3) and presence of UV photons.

The beginning of the project dates 1998, when the team composed by C. Joblin, M. Armengaud and P. Frabel at the CESR (Centre d'Etude Spatiale des Rayonnements) in Toulouse, with the collaboration of P. Boissel, conceived and implemented the central part of the experiment. The set-up is based on a Fourier Transform Ion Cyclotron Resonance (FT-ICR) ion trap mass spectrometer with the additional characteristics of a cryogenic environment.

In the following sections we will describe the experimental set-up with its different sub-systems, the experimental sequence that includes the production, trapping and detection of the ions and the performances of the system. Theoretical aspects on FT-ICR mass spectrometry reported later rest on an extensive literature available on this subject (Amster 1996; Guan & Marshall 1995; Marshall & Schweikhard 1992; Marshall et al. 1998). The photophysical interface (Xe arc lamp and lasers), used in this work, and the chemical interface will be described in details at the end of the chapter.

2.2 Specificities of the system

2.2.1 The cryogenic - ultra-high vacuum environment

The ion trap, central core of the experiment, is enclosed in a vacuum chamber with a total volume of 35 l (cf. Fig. 2.1). Ultra-high vacuum is provided by a pumping group composed of

- a primary pump, (*Pfeiffer*) with a limit pressure of about 10^{-3} mbar measured by a Pirani gauge;
- a turbo-molecular pump (*Pfeiffer*) for the secondary pump. The pressure is measured by a cold-cathode Penning gauge, down to 10^{-11} mbar.

A set of copper cryogenic shields, cooled down by a two-stage cryogenerator (*Coolpak*, *Leybold*), provides a low temperature environment that is important to limit the ion excitation by the thermal background. The actual performances of the shields are a temperature of 80 K on the external shield and 35 K on the ICR cell for a residual pressure $\leq 10^{-10}$ mbar (at room temperature this residual pressure is $\sim 10^{-9}$ mbar).

2.2.2 The magnetic field

A magnetic field of 5 Teslas, oriented along the z axis of the cell (see Fig. 2.3), is generated by an unshielded superconducting magnet. The magnet (*Oxford Instrument*) is composed of several coaxial solenoids and cooled down by a two-stage cryostat. Liquid Helium (4.2 K) is used as a coolant in the inner stage while liquid Nitrogen (77 K) is contained in the outer jacket of the cryostat. The magnetic field is homogeneous at the centre of the cell over a cylindrical volume of internal diameter 5 cm and length 10 cm (cf. Pech (2001)). A cartography of the magnetic field in PIRENEA has shown that the achieved homogeneity is of the order of ~ 30 ppm. The whole system (vacuum chamber, cryogenic shields, trap etc.) can be moved along tracks to facilitate insertion in the magnet bore.

2.2.3 The ICR cell

The ICR cell of PIRENEA has an opened cylindrical geometry. The open-cell design offers some practical advantages like the elimination of charging and contamination on trap plates and both simplified and more efficient introduction of charged particle beams. This latter factor is particularly important for mass spectrometers having external ion sources and is essential in our set-up in which ions are formed outside the cell and the region of homogeneous magnetic field. Moreover this geometry has been chosen in PIRENEA to provide wide optical access to the center of the trap to the laser beam and to the lamp used to perform photophysical experiments.

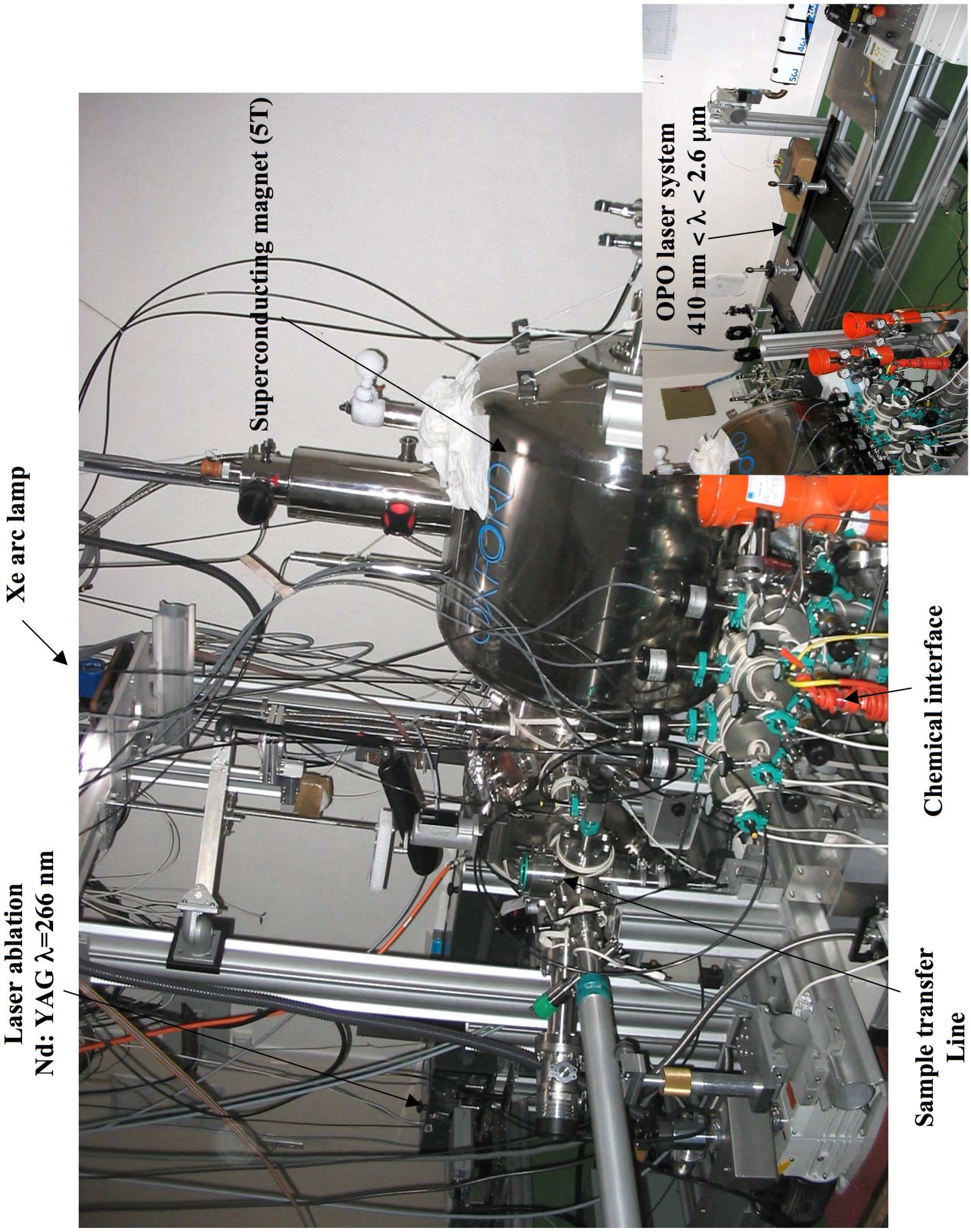
Laser ablation
Nd: YAG λ=266 nm
Xe arc lamp
Superconducting magnet (5T)
OPO laser system
410 nm < λ < 2.6 µm
Sample transfer
Line
Chemical interface

Figure 2.1: Picture of the PIRENEA experimental set-up

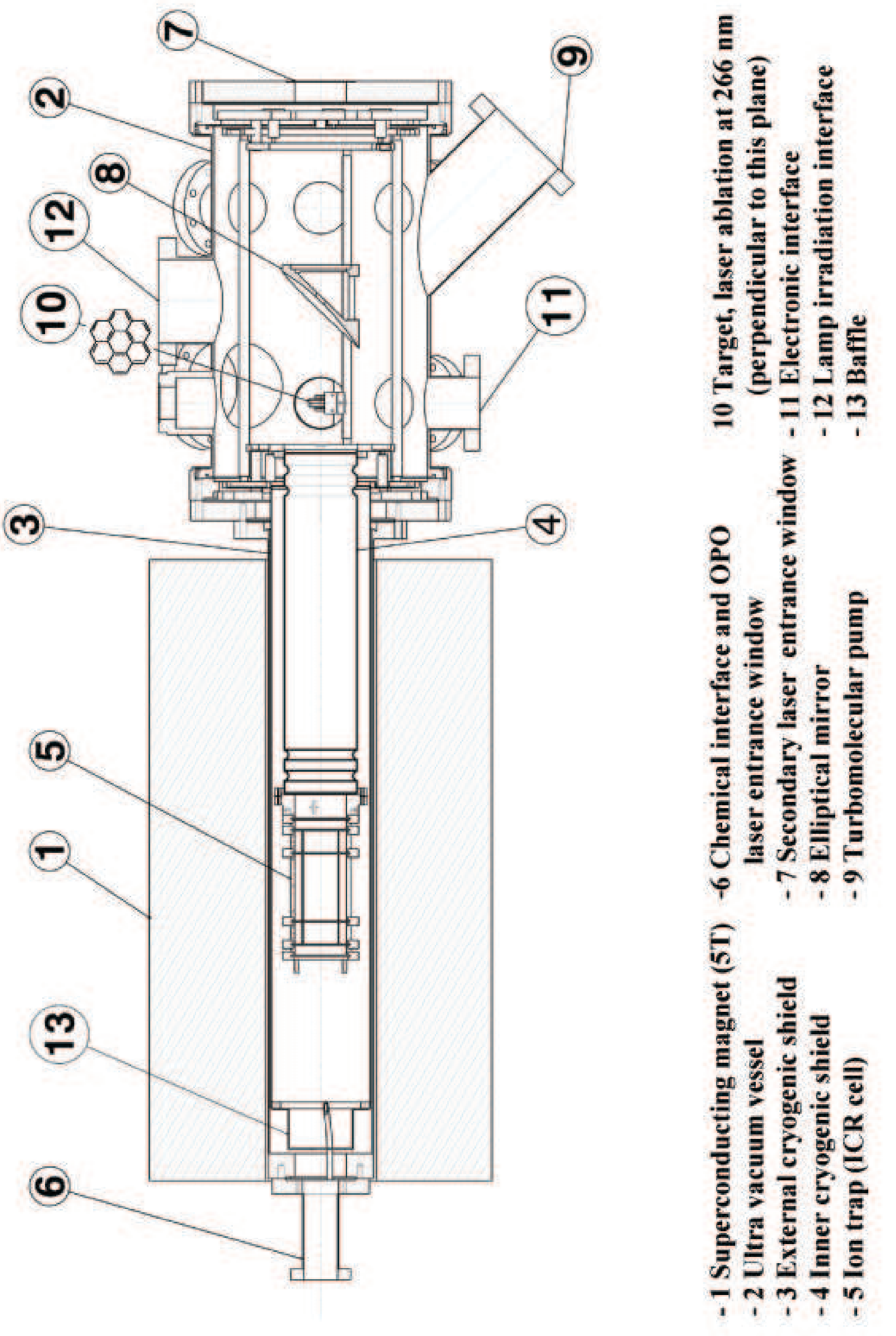
7
2
12
8
10
9
11
3
4
5
1
13
6
- 1 Superconducting magnet (5T)
- 2 Ultra vacuum vessel
- 3 External cryogenic shield
- 4 Inner cryogenic shield
- 5 Ion trap (ICR cell)
-6 Chemical interface and OPO laser entrance window
- 7 Secondary laser entrance window
-8 Elliptical mirror
-9 Turbomolecular pump
10 Target, laser ablation at 266 nm (perpendicular to this plane)
- 11 Electronic interface
- 12 Lamp irradiation interface
- 13 Baffle

Figure 2.2: Schematic view of PIRENEA

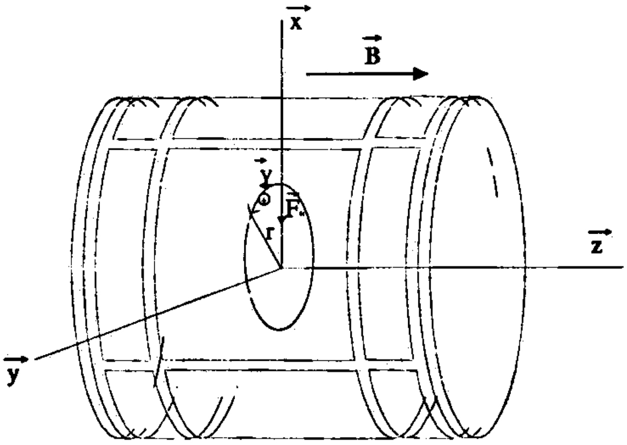

Figure 2.3: Representation of the ICR cell with the magnetic field oriented along the z axis.

The trap has a diameter of 62 mm and a linear length of 160 mm and is composed of three groups of electrodes, each one devoted to a different function: trapping, excitation and detection of ions. The different groups of electrodes are shown in Fig. 2.5. Trapping electrodes consist of two external rings (T_1 and T_4) and of two intermediate segmented rings (T_2 and T_3) while the central electrode, segmented in 4 plates, includes the detection and the excitation electrodes (D_1, D_2 and E_1, E_2). This particular configuration differs from classical trap geometries in which trapping electrodes are usually perpendicular to the other groups of electrodes (cf. Fig. 2.4). The electrodes are made of a non-magnetic material called "ARCAP", which is an alloy of copper and nickel. Electric isolation between the electrodes is obtained by ceramics rings.

2.3 Experimental procedures

2.3.1 Sample preparation and ion production

PAH samples are prepared using commercially available PAH powders (*Sigma-Aldrich*, purity 97 %) diluted in toluene. Powder and solvent are mixed using a magnetic beater until an homogeneous solution is obtained. The solution is then dripped on a solid target (shown in Fig. 2.6) which is subsequently heated until a solid uniform deposit is obtained by evaporation of the solvent. The solid target is put on a metal holder and admitted in the vacuum chamber through a transfer line after pumping in an intermediate chamber (cf. Fig. 2.1).

To be sure that the sample will not undergo evaporation inside the vacuum chamber, the

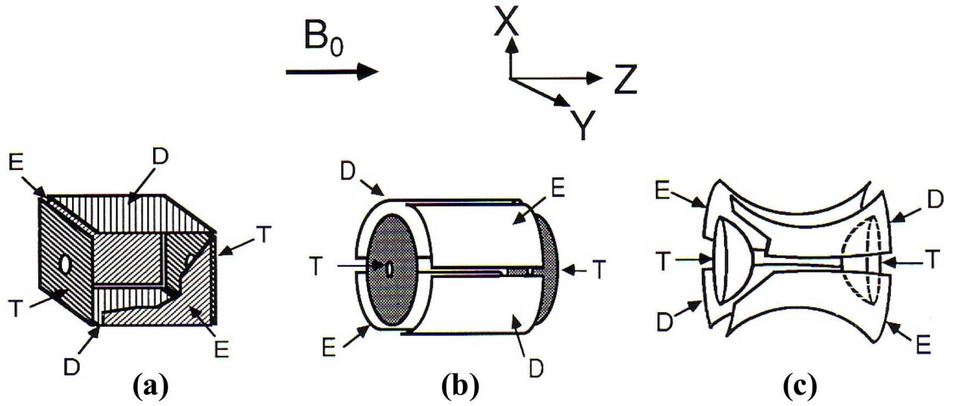

Figure 2.4: Examples of different trap geometries: cubic (*a*), cylindrical (*b*) and hyperbolic (*c*). Excitation, detection and trapping plates are indicated respectively with the letters E, D and T (figure taken from Grosshans et al. (1991)).

saturated vapour pressure of the studied molecules has to be determined using, for instance, the Clapeyron law

$$P_{sat} = P_0 \, exp \left(\frac{-\Delta H}{k_B T} \right) \tag{2.1}$$

where P_0 is the reference pressure, $\Delta\, H$ is the enthalpy variation, k_B the Boltzmann constant and T the temperature. In the case of coronene ($C_{24}H_{12}$), for example, using the empirical values determined by Verstraete (1990), P_0 = 10^{11} torr and $\Delta\, H$ = 3060 + 39.8 M, we obtain at room temperature (300 K) a vapour pressure of about 1.9 10^{-11} mbar. The residual pressure in the chamber being about 10^{-10} mbar, the evaporation of the sample is not a concern for the quality of the vacuum in the chamber. Furthermore, the samples that are feeded into the central chamber are cooled down radiatively by the cold environment. This further decreases their vapor pressure so that even in the case of smaller PAHs (higher vapour pressure), like pyrene, the residual pressure is not an issue.

The target is located outside the magnetic field (z = 537 mm relative to the trap center) and outside the z axis (radial distance r = 30 mm) in order to provide optical access for the laser and lamp beams. Desorption and ionisation of molecular species result from laser ablation of the solid target using the fourth harmonics, λ = 266 nm, of a Nd:YAG laser (Minilite II, Continuum). Neutral PAHs have strong absorption transitions at this wavelength so they can easily absorb the laser photons and get ionised. A variable optical attenuator is used to reduce

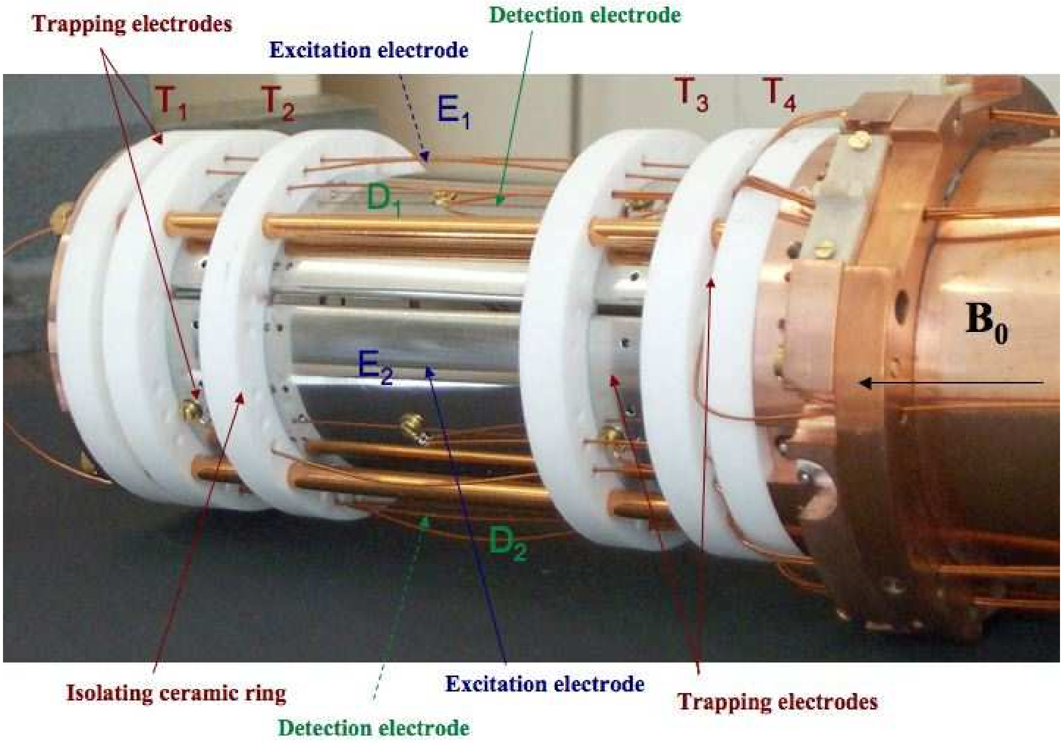
Trapping electrodes
Detection electrode
Excitation electrode
T1
T2
E1
T3
T4
D1
B0
E2
D2
Isolating ceramic ring
Excitation electrode
Trapping electrodes
Detection electrode

Figure 2.5: Picture of the ICR cell of PIRENEA showing the different groups of electrodes.

the laser beam intensity and optimise ablation conditions depending on the sample. The neutral species, evaporated by the laser shot, are immediately condensed on the low-temperature walls, while some of the ions enter the trap guided by the magnetic field.

In each experiment time sequencing and data collection are controlled through a LabView-based data acquisition interface.

2.3.2 Trapping of ions

The magnetic field applied along the z-direction confines the ions in the x and y directions according to their cyclotron motion (see the following section). To trap them along the z-axis an electrostatic potential, either positive or negative depending on the charge of the species, is applied on the trapping electrodes. Typical potential values used in our experiments are between 9 and 18 V on the external trapping electrodes, T_1 and T_4 (cf. Fig.2.5), and between 2 and 4 V on the intermediate electrodes, T_2 and T_3. In Fig. 2.7 we show a representation of the three-dimensional quadrupolar electrostatic field created inside the cell for applied trapping potentials of respectively 2 and 9 V. We can observe that this leads to a potential of 0.13 V at the centre of

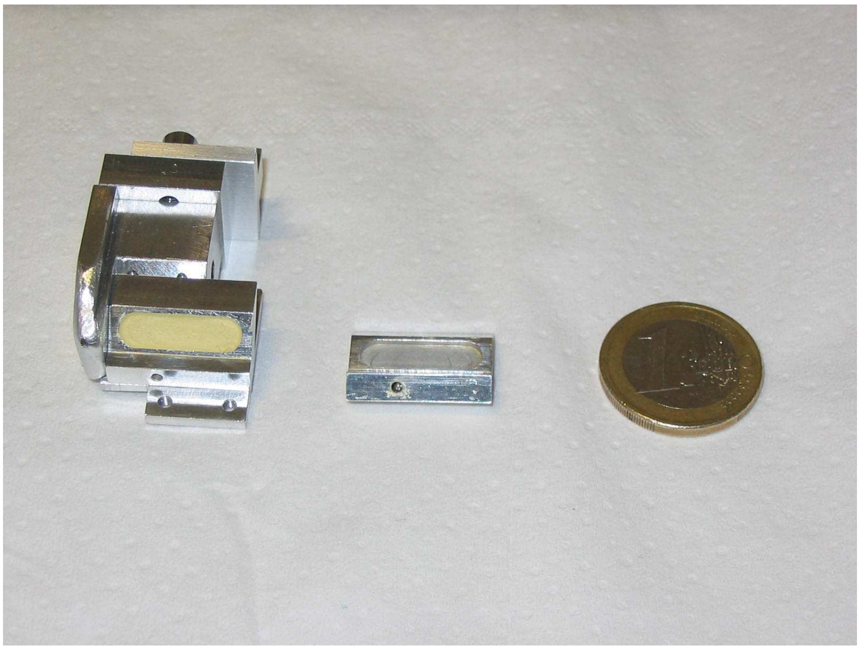

Figure 2.6: Target on its metal support with a coronene deposit.

the cell. Equipotential contours have been generated with the ion modelling software SIMION (version 8.0).
To empty the cell at the end of an acquisition sequence, negative potentials (if the studied species are cations or positive otherwise) are applied on the trapping electrodes to eject the ions.

2.3.3 Description of ion motions inside the cell

An ion of mass m and charge $q = ze$ moving with a velocity v in the presence of a spatially uniform magnetic field B, is subject to a force given by:

$$m\frac{dv}{dt} = qv \times B \tag{2.2}$$

Let $v_{xy} = \sqrt{{v_x}^2 + {v_y}^2}$ denote the ion velocity in the xy plane (i.e. the plane perpendicular to B). Because of angular acceleration $dv/dt = {v_{xy}}^2/r$, the previous equation becomes

$$\frac{m{v_{xy}}^2}{r} = qv_{xy}B \tag{2.3}$$

Angular velocity, ω (in rad/s) about the z axis is defined by $\omega = v_{xy}/r = 2\pi\nu_c$. Using this relation in the last equation we obtain the cyclotron frequency, ν_c, associated to the ion motion:

$$\nu_c = \frac{qB}{2\pi m} = \frac{zeB}{2\pi m} \tag{2.4}$$

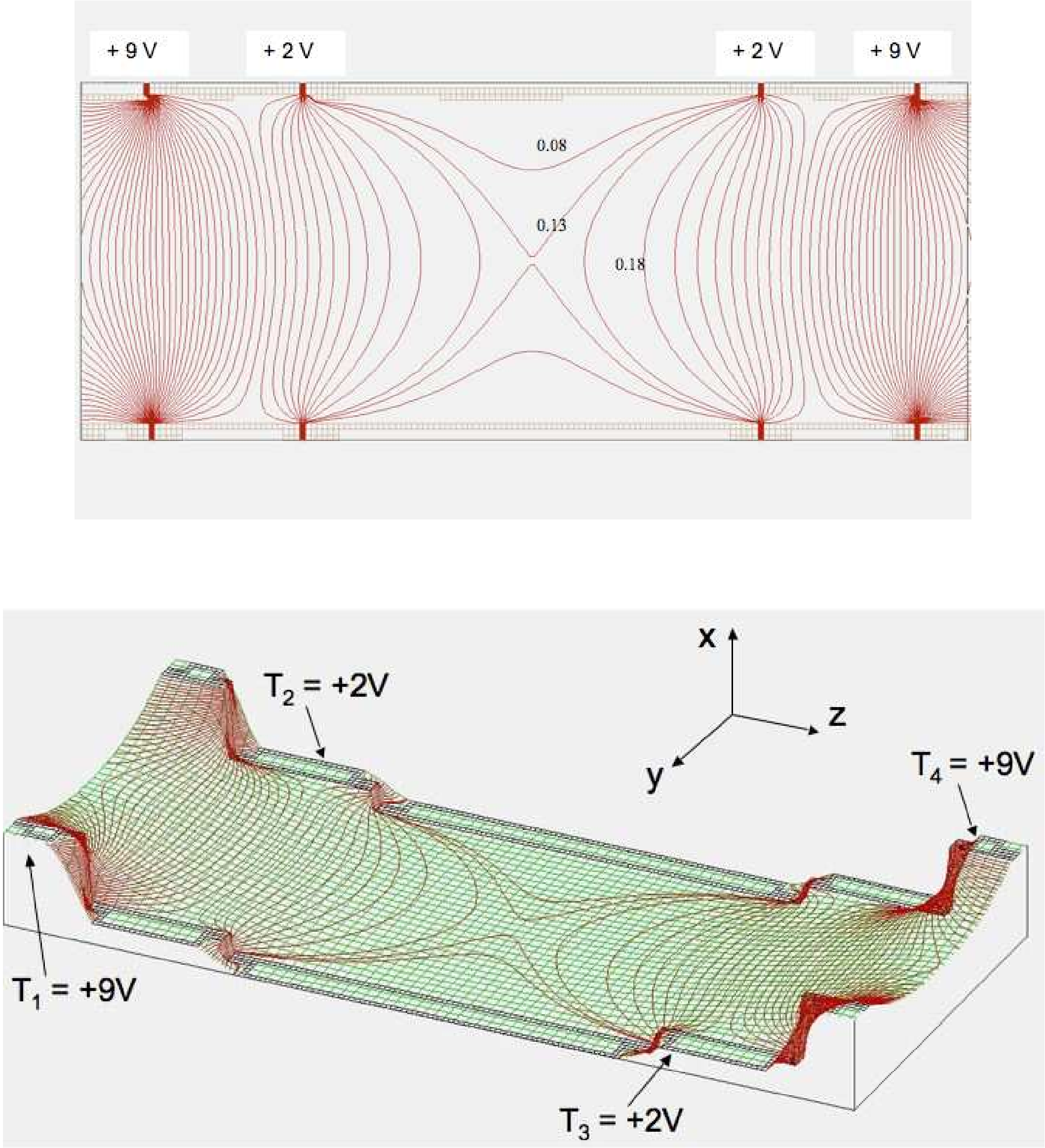

Figure 2.7: SIMION generated equipotential contours (red lines) of the electrostatic field inside the cylindrical ICR cell of PIRENEA. In the example shown, trapping potentials are set equal to 9 V on the external electrodes and equal to 2 V on the intermediate ones. Top: view of a longitudinal section of the cell (x-z plane). Bottom: 3D view of the section represented in the top panel.

A remarkable feature of this equation is that all ions of a given mass-to-charge ratio (*m*/z) have the same ICR frequency independent of their velocity. ICR frequencies for ions formed from typical molecules ($15 \leq m/z \leq 10000$) range from a few MHz down to a few KHz (cf.

Fig. 2.8).

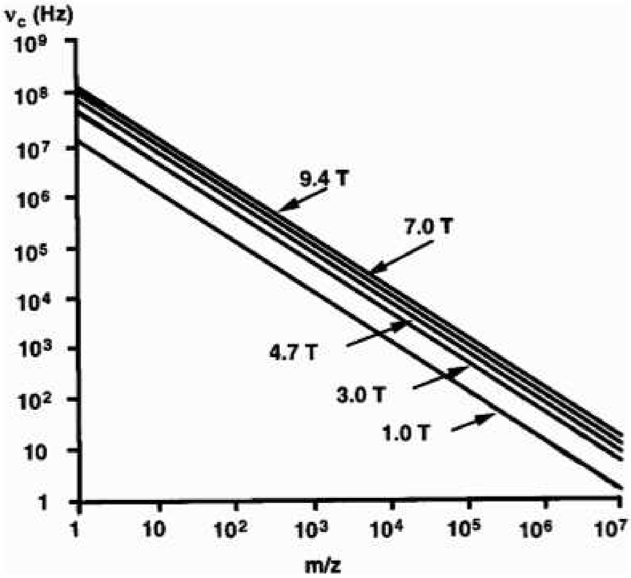

Figure 2.8: ICR orbital frequency in Hz as a function of ionic mass-to-charge ratio, m/z, for different magnetic field strengths (Figure taken from Marshall et al. (1998)).

In the presence of a trapping potential, pure cyclotron frequency is perturbed by the radial component of the electric field. The three-dimensional quadrupolar electrostatic trapping potential inside the cell has the form:

$$\Phi(x,y,z) = V_0\left(\frac{\alpha}{2d^2}(2z^2 - x^2 - y^2)\right) \tag{2.5}$$

in which V_0 is the potential applied on the trapping electrodes, d is the distance between the trapping electrodes (equal to the trap length) and α is a constant that depends on the trap shape. The radial electric field that acts on the ion produces an outward-directed electric force that opposes the inward-directed Lorentz magnetic force. We can obtain the equation for ion motion in the xy plane combining Eq. 2.5 with Eq. 2.3

$$m\omega^2 r = qB\omega r - \frac{qV_0\alpha}{d^2} r \tag{2.6}$$

This is a quadratic equation in ω. Making the substitution $\omega = 2\pi\nu_c$ and solving it for ν we obtain two solutions:

$$\nu_c{}' = \frac{\nu_c}{2} + \sqrt{\left(\frac{\nu_c{}^2}{2}\right) - \frac{\nu_z{}^2}{2}} \tag{2.7}$$

$$\nu_m = \frac{\nu_c}{2} - \sqrt{\left(\frac{\nu_c{}^2}{2}\right) - \frac{\nu_z{}^2}{2}} \tag{2.8}$$

in which $\nu_c{}'$ is the reduced cyclotron frequency, ν_c the original "unperturbed" cyclotron frequency, ν_m is the magnetron frequency and ν_z the oscillation frequency along the z axis. This latter can be determined solving the equation for the ion z-motion derived from Eq. 2.5

$$m\frac{d^2z}{dt^2} = -q\frac{d\Phi(z)}{dz} = -\frac{2qV_0\alpha z}{d^2} \tag{2.9}$$

$$\nu_z = \frac{1}{2\pi}\sqrt{\frac{2qV_0\alpha}{md^2}} \tag{2.10}$$

To summarise, the ions trapped in the ICR cell follow three different oscillatory motions (illustrated in Fig. 2.9) of respective frequencies $\nu_c{}'$, ν_m and ν_z. The three frequencies are related by the following expressions

$$\nu_c{}' + \nu_m = \nu_c \tag{2.11}$$

$$\nu_c{}' \times \nu_m = \frac{\nu_z{}^2}{2} \tag{2.12}$$

The magnetron and trapping frequencies are usually much less than the cyclotron frequency. In the case of the coronene cation, $C_{24}H_{12}{}^+$, (m/z = 300.0939), for example, we have calculated, in our experimental conditions, the following values for the four different frequencies: ν_c = 255.755 kHz, ν_m = 33 Hz, ν_z = 4102 Hz and $\nu_c{}'$ = 255.722 kHz.

2.3.4 Excitation and detection of ions

Excitation

The analysis of ions by FT-ICR mass spectrometry is based on the detection of the image current induced by the cyclotron ion motion on the central electrodes of the cell. Once trapped in the cell, all the ions with the same mass-to-charge ratio turn at their characteristic cyclotron frequency. The cyclotron radius of thermal ions is usually small compared with the dimension of the cell and cannot induce a detectable signal, considering further that the phase of each ion orbital motion is random. Thus for an ensemble of ions, any charge induced in either of the two opposed detection plates will be balanced, on the average, by an equal charge induced by an ion whose phase is 180 degrees different. In these conditions the net difference in detected charge between the two plates is zero.

A radio frequency (r.f.) sinusoidal voltage is applied to the excitation plates to induce a spatial

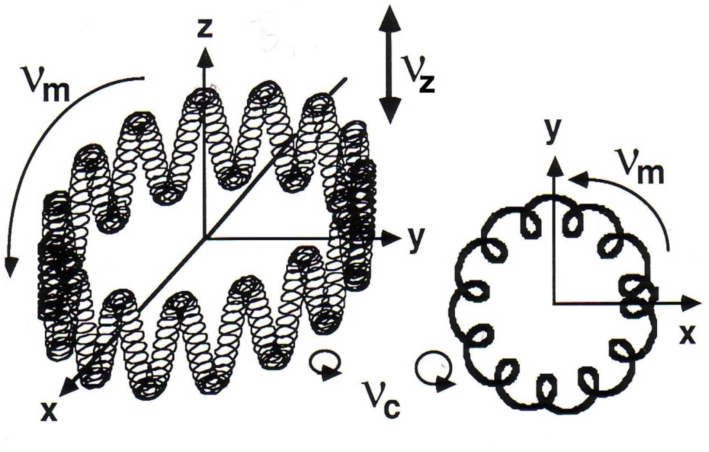
z
ν_m
ν_z
y
x
ν_c
y
ν_m
x

Figure 2.9: Motions followed by an ion trapped in the ICR cell.

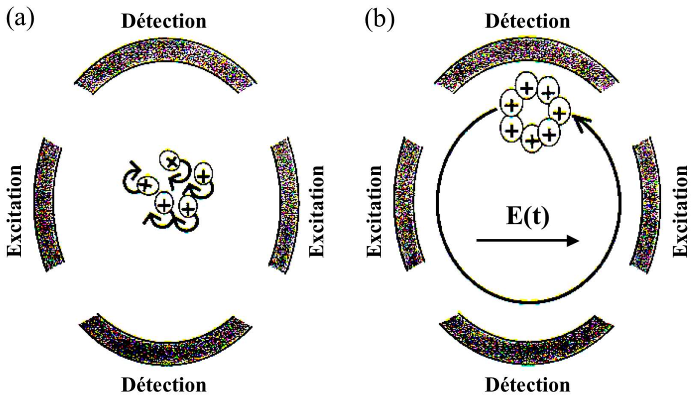
(a)
Détection
Excitation
Excitation
Détection
(b)
Détection
Excitation
E(t)
Excitation
Détection

Figure 2.10: Incoherent cyclotron movement of an ion packet (on the left) converted into a coherent movement (on the right) by resonant radio-frequency excitation at frequency ν_c'.

coherence in the ion packet and, thus, a detectable signal. Only ions that have their cyclotron frequency in resonance with the applied electric field are driven into a coherent motion, ions that are not in resonance do not absorb energy and remain at the centre of the cell. The coherently orbiting ion packet induces a differential current between the two opposed detection electrodes.

This time-domain signal, amplified and digitalised, is finally Fourier-transformed to retrieve a frequency domain spectrum. The mass spectrum is obtained from the frequency spectrum by applying a calibration formula derived from the cyclotron equation and using two calibration masses (Pech 2001; Ledford et al. 1984). If the r.f. voltage is applied continuously (or if it is strong enough) the ions that absorb energy will spiral outward until they collide with an excitation or detection plate where they will be neutralised. This technique, called ejection, is used to remove from the cell mass-selected ions within a mixture if they are of no immediate interest (for instance ^{13}C isotopic peaks in the case of PAHs).

In the experiments described here excitation is performed adopting the stored waveform inverse Fourier transform (SWIFT) excitation technique (Marshall et al. 1985) and using a broadband excitation to cover a mass range as broad as possible (this depends on the power of the amplifier for the excitation of the ions). The SWIFT technique consists in calculating the excitation signal from the inverse Fourier transform of the frequency range of interest and in supplying signals with a constant amplitude over the whole selected frequency range.

Detection

Image current detection is non-destructive as the ions remain in the analyser cell after the detection process has been completed. In this way trapped species can be subjected to consecutive analysis sequences without being lost. This allows to study sequential processes that can be quite complex, for instance isolation of the parent ions, fragmentation, selection of a daughter species and reactivity of this daughter species with molecules.

Detection is defined by two important parameters:

- the number of detected data points (N) (in our experiment $2^{11} < N_{PIRENEA} < 2^{20}$)
- the signal sampling frequency, $\Delta\nu_{sample} = 1/\Delta t_{sample}$ (0.05 < $\Delta t_{PIRENEA}$ < 10 μs/point).

As we will see in section 2.4.2, mass resolution improves in direct proportion to the length of the transient that is recorded (cf. Fig. 2.12), so for a given number of data points the resolution improves using small sampling frequencies (larger Δt_{sample}). The sampling frequency should however be at least twice the frequency of the ions (Nyquist sampling criterion). Also this requires to have a transient signal that is longer that the recording time (cf. Sect. 2.4.2).

2.4 Performance of the ICR trap

Fourier transform mass spectrometry (FTMS) is capable of achieving much higher mass resolution than any other type of mass spectrometry (except for the recently developed orbitrap technique, Makarov (2000); Hu et al. (2005)) and is capable of providing mass accuracies of

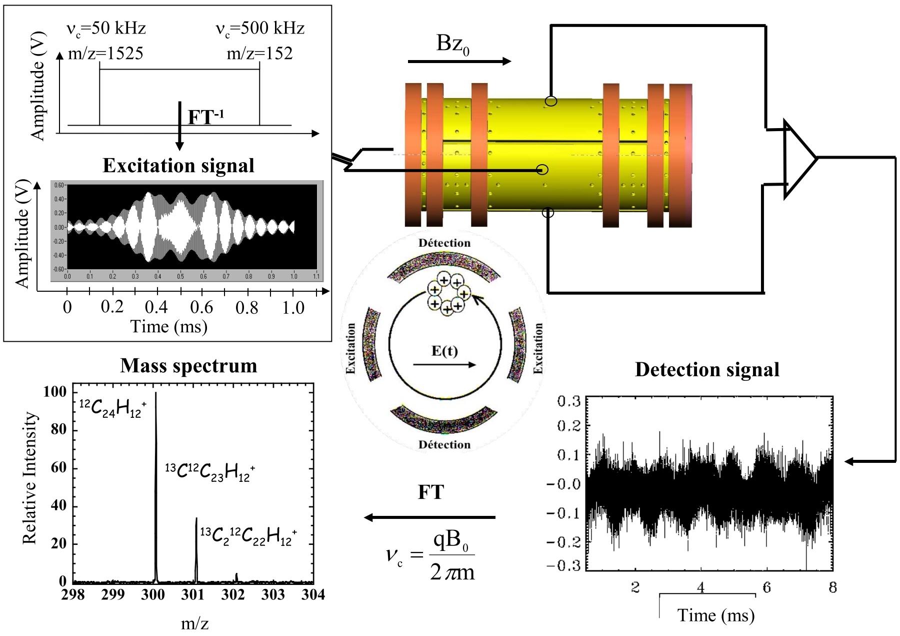
νc=50 kHz
m/z=1525
νc=500 kHz
m/z=152
Amplitude (V)
FT-1
Excitation signal
Amplitude (V)
0
0.2
0.4
0.6
0.8
1.0
Time (ms)
Bz0
Détection
Excitation
E(t)
Excitation
Détection
Detection signal
0.3
0.2
0.1
-0.0
-0.1
-0.2
-0.3
2
4
6
8
Time (ms)
Mass spectrum
Relative Intensity
100
80
60
40
20
0
12C24H12+
13C12C23H12+
13C212C22H12+
298
299
300
301
302
303
304
m/z
FT
νc = qB0 / 2πm

Figure 2.11: Example of a detection sequence: detection of coronene ions $C_{24}H_{12}^{+}$ and its ^{13}C isotopes.

the order of a few ppm over a fairly wide mass-to-charge range. Moreover, as it allows for extensive manipulation of stored ion populations, it represents a versatile tool for solving analytical problems in chemical and biological sciences, and it has, therefore, a variety of possible applications such as surface analysis, polymer studies, fullerene characterisation and proteomics (see the review papers of Dienes et al. (1996) and Bogdanov & Smith (2005) and references therein and the books of Asamoto (1991) and Lehman & Bursey (1976)).
In this section we will detail the characteristics of the FT-ICR trap of PIRENEA.

2.4.1 Number of ions in the cell

Ideally we can associate the ion cloud in the cell to an homogeneous sphere of radius R and uniform charge density ρ. The total charge Q in the sphere is then equal to $4\pi R^3\rho$ while the potential created on the sphere surface is $V_{sphere} = Q/4\pi\varepsilon_0 R$. In order to trap ions this V_{sphere} potential created by the cloud must be lower than the trapping potential. Typical trapping potentials that we have used in the experiments are 4 and 18 V, respectively applied on the intermediate and external trapping rings (cf. section 2.2.3), which correspond to a potential of ~ 0.2 V at the centre of the trap (value calculated with SIMION). Assuming for the sphere a diameter

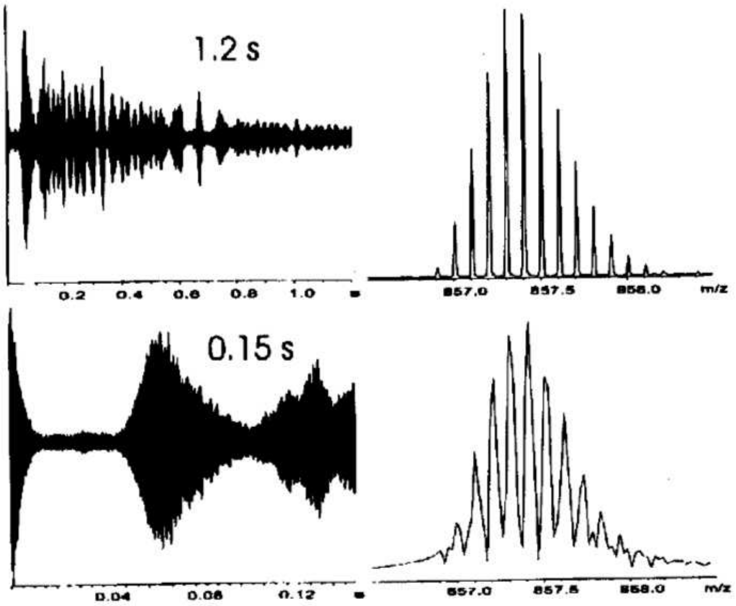

Figure 2.12: Illustration of the relationship between the length of the transient and the resolution that can be achieved: in the top mass spectrum resolution is $\sim$ 90000 while in the bottom spectrum $\sim$12000 (Figure taken from Amster (1996)).

equal to the trap diameter we can obtain an upper limit to the number of ions in the cell. A value of 10^6 ions has been estimated for the ICR cell of PIRENEA (cf. Pech (2001)). Ions exceeding this upper limit will be ejected from the trap. Space-charge effects due to Coulomb interactions between ions can also induce frequency shift and inhomogeneous line broadening (Seung-Jin & Seung 1997).

2.4.2 Mass resolution and mass accuracy

Resolution is the capability to separate closely spaced peaks. In mass spectrometry the mass resolution is usually defined by the ratio $m/\Delta m$, where Δm is the full linewidth at half maximum (FWHM) of a spectral mass peak. From the first derivative of Eq. 2.4 with respect to m we obtain the useful relation

$$\frac{d\nu_c}{dm} = -\frac{\nu_c}{m} \tag{2.13}$$

$$\frac{\nu_c}{d\nu_c} = -\frac{m}{dm} \tag{2.14}$$

For a normal Lorentzian peak shape $\Delta m = 2\sqrt{3}/\tau$, where τ is the signal relaxation time (time needed by ions to dampen back to their thermal energy cyclotron radius orbit). Therefore

$$\frac{m}{\Delta m} \propto \frac{qB\tau}{m} \tag{2.15}$$

So the longer it takes for the ions excited radius of orbit to dampen back to the thermal energy radius, the longer one can observe the time domain signal and the better the spectral resolution will be. At higher pressures τ is smaller and resolution diminishes, we can then understand the importance of working in low pressure conditions. A narrow peak, however, does not necessarily guarantee high resolution. Under some circumstances peaks that are closely spaced in frequency will coalesce into a single peak. The mechanism proposed for this behaviour is a collective motion of ion packets with close frequencies owing to an interaction between electric fields associated with each ion packet (Huang et al. 1994). The time needed for this collective motion to develop is a function of the number of ions in the cell, the frequency spacing between the ions, the amplitude of the trapping potential, the size of the analyser cell and the radius of the orbit of the ions (Nikolaev et al. 1995).

2.4.3 Detectable mass range

The lowest detectable value of m/z is limited by the highest frequencies provided by the excitation-detection electronics, whereas the highest m/z value depends on the trapping performances of the cell. Eq. 2.7 shows that the magnetron and reduced cyclotron frequencies converge to a common value $\nu_c{}' = \nu_m = \nu_c/2$ when

$$\left(\frac{\omega_c}{2}\right)^2 = \frac{\omega_z{}^2}{2} \tag{2.16}$$

Substituting the expressions of ω_c and ω_z in the previous equation we obtain the relation

$$m_{critical} = \frac{qB^2d^2}{4V_0\alpha} \tag{2.17}$$

For $m/z > m_{critical}/z$, ion cyclotron motion is no longer stable and the ions spiral outward until they are lost from the trap. The use of lower trapping potentials can help to increase the upper mass limit. The ICR cell of PIRENEA is designed to trap ions with *m*/z from 12 up to 30000.

2.5 Chemical interface

PIRENEA is equipped with four gas inlet lines, each one including a one-liter tank in which the gas is stored and a solenoid valve that controls the injection time. A metering leak valve allows to regulate the flow rate and therefore the pressure, in the vacuum chamber.

Non-reactive molecular or atomic gases can be injected in the vacuum chamber and reactivity of ions at different temperatures can be studied. Because of the interaction with the cold surfaces, one of the major difficulties in these reactivity experiments is to quantify the density of the gas to derive absolute reaction rates.

A method has been developed and tested on PIRENEA to quantify the gas density in the cell using the collisional damping of the ion cyclotron signal. This method was used to study the reactivity of $C_{24}H_{11}^{+}$ with H_2O (see Bruneleau (2007)).

Buffer gas

As discussed in section 2.3.4, selective ejection of ions can be carried out in order to isolate a particular species inside the cell when a mixture is present. This process is systematically performed at the beginning of each experiment in order to remove from the trap isotopes created with the main species by the laser ablation. During the ejection process, however, the ion cloud is perturbed to some extent and can undergo some expansion as remaining ions may retain some residual excitation energy. A cold buffer gas (helium) is then injected to cool the molecules through elastic collisions. The buffer gas acts as a medium to enable the ions to exchange kinetic energy with the cold walls of the trap so that the ion cloud can relax to the centre of the cell. Typical gas pressures of $\sim$0.1 mbar are usually set in the buffer gas tank that lead to pressures in the range of 10^{-7} mbar in the ICR cell.

2.6 Photophysical interface

2.6.1 The Xe arc lamp

A 150 W Xe arc lamp (Photomax model 60100, Oriel) is used to perform photo-dissociation studies. The lamp radiation is focused at the center of the cell by an aluminium elliptical mirror. This spectral source produces a broad continuum between 200 and 1600 nm, close to that of a 6000 K blackbody with additional lines (cf. Fig. 2.13). A water filter is installed below the lamp to remove infrared radiation beyond 950 nm and long-pass coloured filters, whose cut-off wavelength λ_c is defined at 50% of transmission, can be inserted to further select a particular range of wavelengths.

2.6.2 Lasers

In this section, we will describe the main characteristics of the ablation laser and of the two different OPO lasers used to perform spectroscopy experiments.

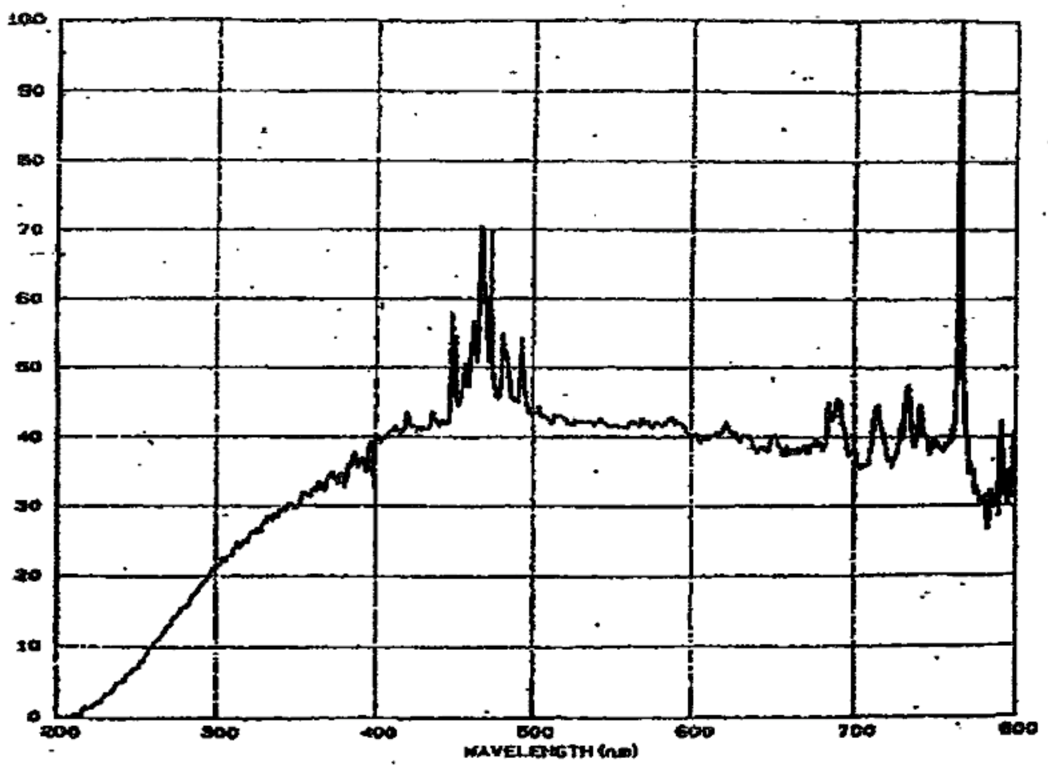

Figure 2.13: Xe arc lamp spectrum between 200 and 800 nm given by the constructor.

2.6.2.1 The Minilite II laser (*C*ontinuum)

This Nd:YAG laser is optically pumped using a flashlamp. It emits light with a wavelength of 1064 nm, with a 50 mJ energy and a pulsewidth of 5-7 ns. The high-intensity pulses may be efficiently frequency doubled to generate laser light at 532 nm, or higher harmonics at 355 and 266 nm. In our experiments we used the fourth harmonics, λ = 266 nm, to perform laser desorption and ionisation from the solid target. At this wavelength the typical output energy is $\sim$ 4 mJ.

2.6.2.2 Introduction to optical parametric oscillators (O.P.O.)

An optical parametric process relies on the nonlinear response of a medium (usually a crystal) to a driving field (the pump laser beam). In this process, the pump photon, propagating into the crystal, splits into a pair of less energetic ones. The resulting two photons will not, in general, have the same energies. The higher energy photon produced is referred to as the signal, while the lower energy photon is called the idler.

Energy and the momentum vector must be conserved in this process. Energy conservation

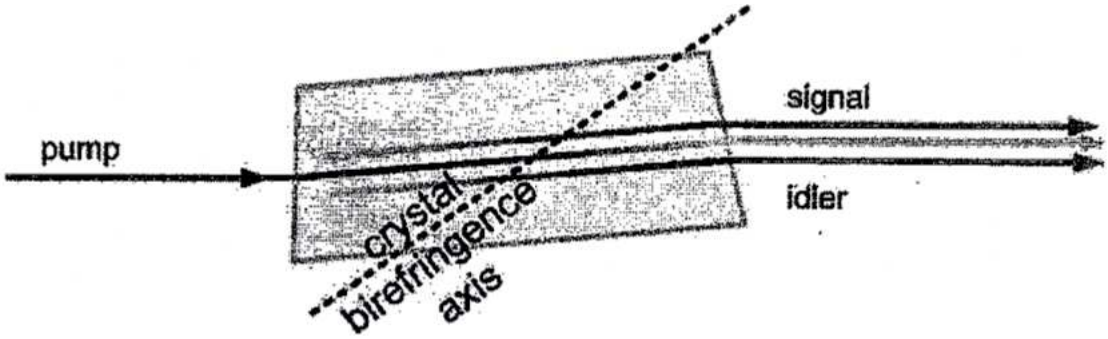

Figure 2.14: An optical parametric process.

is satisfied when the sum of signal and idler frequencies equals the pump frequency, that is

$$h\nu_p = h\nu_s + h\nu_i \tag{2.18}$$

where $h\nu$ is the photon energy. Linear momentum is conserved when

$$\overrightarrow{k_p} = \overrightarrow{k_s} + \overrightarrow{k_i} \tag{2.19}$$

where $\overrightarrow{k}$ is the photon momentum vector.
Linear momentum will not, in general, be conserved, because the two resultant photons have different frequencies than the pump and velocity is dependent on frequency. To achieve the simultaneous conservation of energy and momentum the system takes advantage of the birefringence of a transparent nonlinear crystal called BBO (beta-barium borate). Such materials have different indices of refraction for different polarizations of light. One index varies with changes in propagation direction with respect to the crystal angle.
The angle tuning to produce a particular signal / idler pair is called phase matching. An advanced computer control system settles the phase matching while moving over wide wavelength ranges. When the signal and idler beams exit the OPO oscillator, a pair of dichroics separate the two signals. At 710 nm the signal and idler become degenerate (have the same wavelength) so the dichroics cannot separate the two signals in the 690-730 nm region and the OPO laser cannot be used in this wavelength range.

In our experiments two different OPO laser systems have been used to perform multiphoton dissociation spectroscopy. Both systems were pumped by a 355 nm Nd:YAG laser beam. The main characteristics of the two lasers are described below.

The Surelite OPO laser (*C*ontinuum)

The broad band OPO laser (bandwidth > 50 cm^{-1}) provides an output signal continuously tunable between 410 nm and 2.6 μm, with a pulse repetition rate of 10 Hz and a pulse duration of 4 ns. The mean energy per pulse is E = 15 mJ ± 20 % between 440 and 500 nm (E_{max} =18 mJ at 470 nm), dropping to 5 mJ at 420 nm.

The Panther EX laser (*C*ontinuum)

The Panther EX OPO generates an output signal continuously tunable between 410 and 2550 nm. It operates at 10 Hz with a 5 ns pulse duration and a 5 cm^{-1} bandwidth. The system is also equipped of a doubling stage (doubler) capable to extend the lower wavelength limit from 410 down to 205 nm. The doubler can provide up to 10 mJ of UV energy (depending on the pump laser). The output mean energy per pulse, in the visible range, is shown in Fig. 2.15.

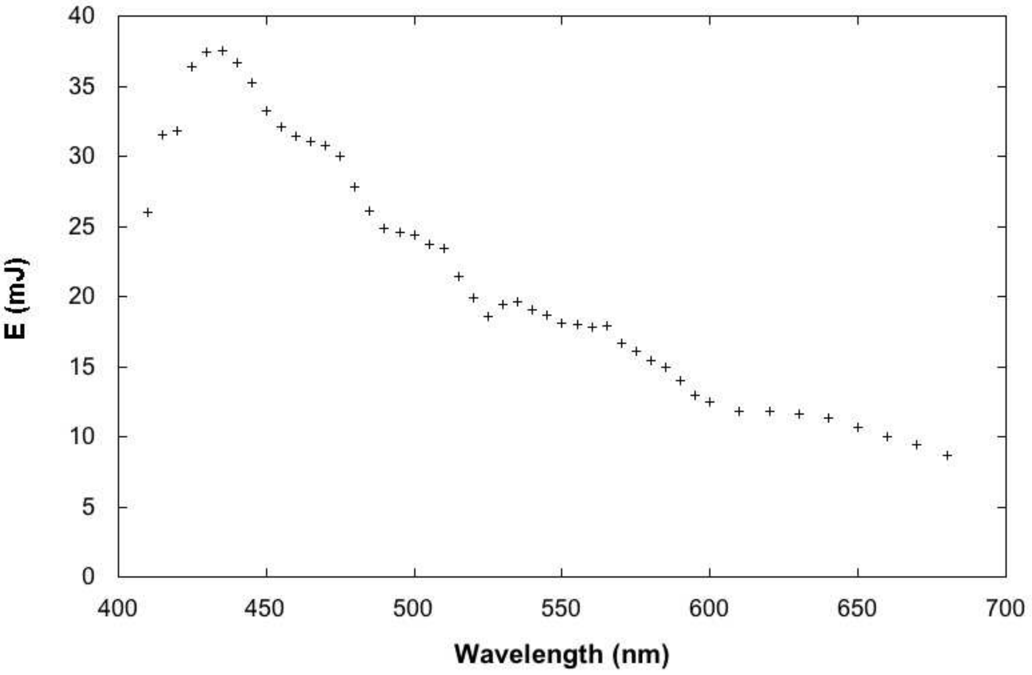

Figure 2.15: Panther EX OPO output mean energy per pulse measured in the visible range as a function of wavelength.

Chapter 3

Photofragmentation of isolated PAH cations

Omnia mutantur, nihil interit.
Everything changes, nothing perishes.

3.1 Introduction

Molecular photodissociation is the main limiting process for the survival of PAHs in the ISM. As seen in the first chapter upon absorption of UV photons, a highly vibrationally excited PAH molecule can relax through the emission of IR photons. In competition with this process the molecule may undergo fragmentation that can lead to hydrogen loss or to the destruction of the carbon skeleton. The study of the evolution of PAH molecules under UV irradiation is then of great importance to get an insight into the nature of species that can survive in the ISM.

There have been a significant number of experimental works on the photostability and photodissociation of PAHs. Dunbar (1992) performed time-resolved photodissociation mass spectrometry (TRPDMS) of PAH ions in an FT-ICR ion trap. In these experiments a laser pulse excite ions above the dissociation threshold, then the extent of photodissociation is determined as a function of the delay between the laser pulse and the ICR detection sequence.

Boissel et al. (1993, 1997) studied the photodissociation of PAH cations in an FT-ICR cell using the near UV-visible radiation of a Xe arc lamp. The same technique was used by Ekern et al. (1997, 1998) to record fragmentation products of a larger number of PAH cations. The authors classified the studied species as either photostable, losing hydrogen only, losing carbon and hydrogen or photodestroyed for particular photon fluxes. Further works using this technique have been performed by Banisaukas et al. (2004) and Dibben et al. (2001).

Another method extensively used to investigate photodissociation is the photoelectron photoion coincidence (PEPICO) spectroscopy (Ruehl et al. 1989; Baer et al. 1979). In this technique, ions are accelerated by a homogeneous electric field perpendicular to the photon beam while the photoelectrons are accelerated in the opposite direction. Emitted photoelectrons are collected in coincidence with the produced fragments so that their abundance can be measured as a function of the incident photon energy.

A series of studies using time-resolved photoionisation mass spectrometry (TPIMS) has been published by the group of Lifshitz (Gotkis & Lifshitz 1992; Gotkis et al. 1993; Ling & Lifshitz 1995, 1997, 1998). In these experiments the rate of dissociation of the cation under investigation is monitored versus the excitation energy or versus time. Finally several studies using collision-induced dissociation (CID) have been performed by Wang et al. (1997), Guo et al. (1999) and Shushan & Boyd (1980).

To retrieve molecular parameters of the dissociating species, in particular dissociation rate constants, as a function of the internal energy content, a modelling of these experimental results is necessary. These molecular parameters enter then in astrophysical models that try to estimate the lifetime of PAH species and their size distribution in interstellar environments in relation with their structure, degrees of ionisation and dehydrogenation (see for instance Allain et al. (1996), Le Page et al. (2001, 2003), Jochims et al. (1994) and Jochims et al. (1999)).

Recently the connection between PAHs and small hydrocarbons has gained significant interest thanks to the detection of species like C_3H_2, C_2H and C_4H in PDRs (Teyssier et al. 2004; Pety et al. 2005) whose abundances cannot be accounted for by PDR models. The study in the laboratory of the products and pathways of the photodissociation of PAHs in interstellar-like conditions is the first step to understand how PAHs could contribute to the formation of these smaller species, and to evidence the most photostable structures that are produced.

3.2 Study of the photodissociation pathways

3.2.1 Objectives

The aim of this study is to provide information on both destruction of PAHs by UV radiation and formation channels of small hydrocarbons and carbon clusters. The general question is whether the considered species can easily release some smaller fragments under photon irradiation in the gas-phase. Four different medium-sized PAHs, the pyrene cation ($C_{16}H_{10}{}^+$), the perylene cation ($C_{20}H_{12}{}^+$), the pentacene cation ($C_{22}H_{14}{}^+$) and the naphtho[2,3-a]pyrene cation ($C_{24}H_{14}{}^+$), illustrating the two main structural classes of pericondensed and catacondensed PAHs, are chosen for this study. A comparison among the photodissociation products and pathways identified for each species is made at the end of the chapter.

3.2.2 Fragmentation by multiple photon absorption

Continuous UV-visible irradiation from a Xe arc lamp (wavelengths between 200 and 800 nm) is used to perform dissociation of the selected species. As discussed by Boissel et al. (1997) such irradiation leads to sequential photon absorptions by the trapped species and, consequently, to an increase of their internal energy U. In Fig. 3.1 the internal energy distribution of a population of anthracene cations, ${C_{14}H_{10}}^+$, after three seconds of irradiation is reported together with curves showing the fragmentation rate and the IR cooling rate, in the energy region where they are comparable.

The whole process has, in fact, to be considered as a competition between the heating by absorption of photons and the radiative cooling. This competition leads to a statistical distribution of the internal energy of the ions and when the heating is sufficient the distribution extends up to the zone where fragmentation occurs. Otherwise stated, dissociation proceeds when the internal energy becomes higher than a critical value E_{th}, which corresponds to the dissociation threshold. In Fig. 3.1, for instance, dissociation only occurs for ions that are located in the high energy tail of the distribution when they absorb an additional photon.

The dissociation threshold is a function of the size of the considered species and of the chemical bond that has to be broken. For the medium-sized PAHs considered here (with a number of carbon atoms $N_c \leq 24$) E_{th} is on the order of 10 eV (for instance $E_{th} \sim 7$ eV for the anthracene cation, ${C_{14}H_{10}}^+$, cf. Fig. 3.1).

3.2.3 Experimental methods

The experimental procedure consists in the following steps:

- production and isolation of the ions of interest in the ICR cell of the PIRENEA set-up;
- cooling down of the ions by collision with a buffer gas (helium);
- photon irradiation of the selected species;
- recording of the dissociation products by mass spectrometry.

Parent ions are isolated using a SWIFT waveform (cf. sect. 2.3.4) to eject isotopic species, as shown in Fig. 3.2 for the pentacene cation. Selected species are then subjected to broad-band visible and UV radiation from the Xe arc lamp.

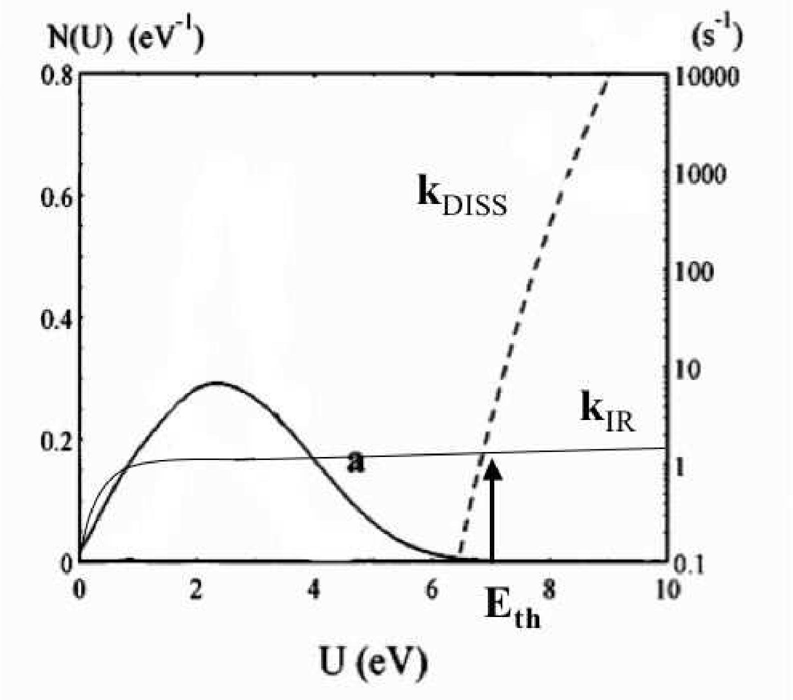

Figure 3.1: Representation of the calculated internal energy distribution (curve a), the fragmentation rate (k_{DISS}) and the IR cooling rate (k_{IR}) for a population of anthracene cations irradiated by 1.73 eV photons. Figure adapted from Boissel et al. (1997).

For all the considered PAHs an inventory of the formed species is made and the main fragmentation patterns are identified. Photofragmentation pathways can be investigated by two methods. In the first method, each fragment ion is isolated with a second SWIFT waveform and then photolysed to determine its fragmentation pattern. In the second method, individual fragment ions are continuously ejected during lamp irradiation eliminating daughter species produced by the fragmentation of the ejected ions. Evolution of an ion population can also be measured by isolating the species of interest and detecting its fragments as a function of irradiation time.

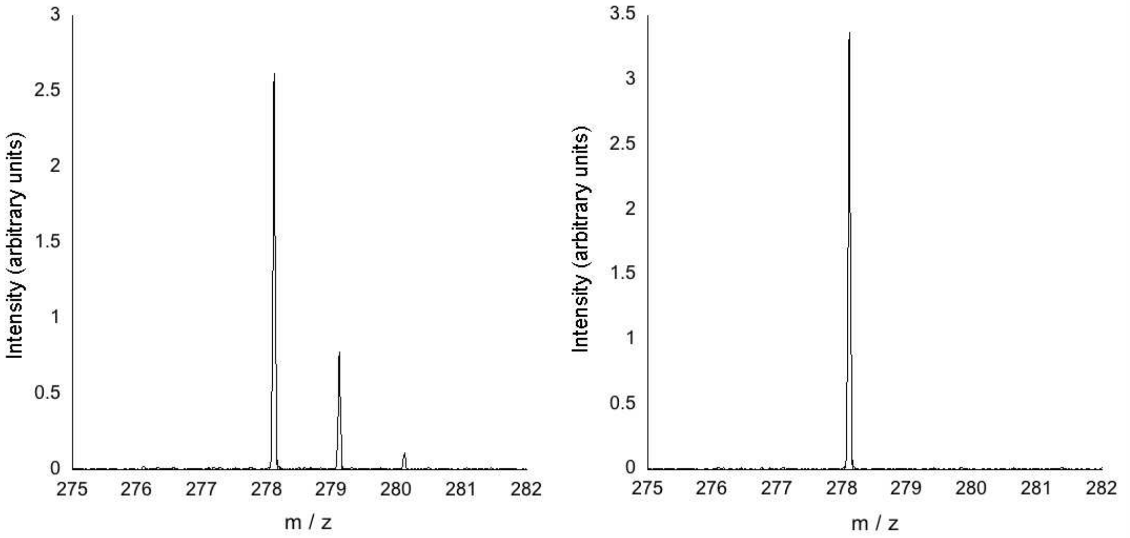

Figure 3.2: Left panel: detection of pentacene ions, $C_{22}H_{14}^{+}$, and its ^{13}C isotopes. Right panel: isolation of $^{12}C_{22}H_{14}{}^{+}$ parent ions after ejection of the isotopes.

3.3 Results

3.3.1 The Pyrene cation ($C_{16}H_{10}{}^{+}$, m/z = 202)

Figure 3.3 displays the photodissociation spectrum recorded for the pyrene cation after 10 s of irradiation with the Xe arc lamp. As the experiment is performed under continuous irradiation most of the peaks are not primary daughter species but produced by further fragmentation. Dehydrogenation of the parent ion up to six hydrogen atoms is observed together with the formation of smaller hydrocarbons and carbon cluster ions.

In order to investigate the different fragmentation pathways, each of the fragment peaks was isolated, in turn, and briefly irradiated to determine its dissociation products. In Fig. 3.4, we show the evolution of the relative abundances of the $C_{16}H_{8}{}^{+}$ fragment (doubly dehydrogenated pyrene) and its fragmentation products as a function of the irradiation time. The main dissociation pathway appears to be hydrogen atom loss but other dissociation paths involving the loss of acetylene (C_2H_2) and diacetylene (C_4H_2) molecules are also identified. The latter dissociations mainly occur from even-mass species $C_nH_{2m}{}^{+}$ with the exception of $C_{16}H_{5}{}^{+}$ for which the loss of C_2H_2 is also observed.

The complete photofragmentation cascade is shown in the bottom panel of Fig. 3.3. It can be noticed that all the detected hydrocarbons $C_nH_x{}^{+}$, with $n < 16$, completely dehydrogenate leading to the formation of the corresponding carbon clusters C_n^{+}, the only exception is C_{11}^{+} which comes from the fragmentation of C_{14}^{+}.

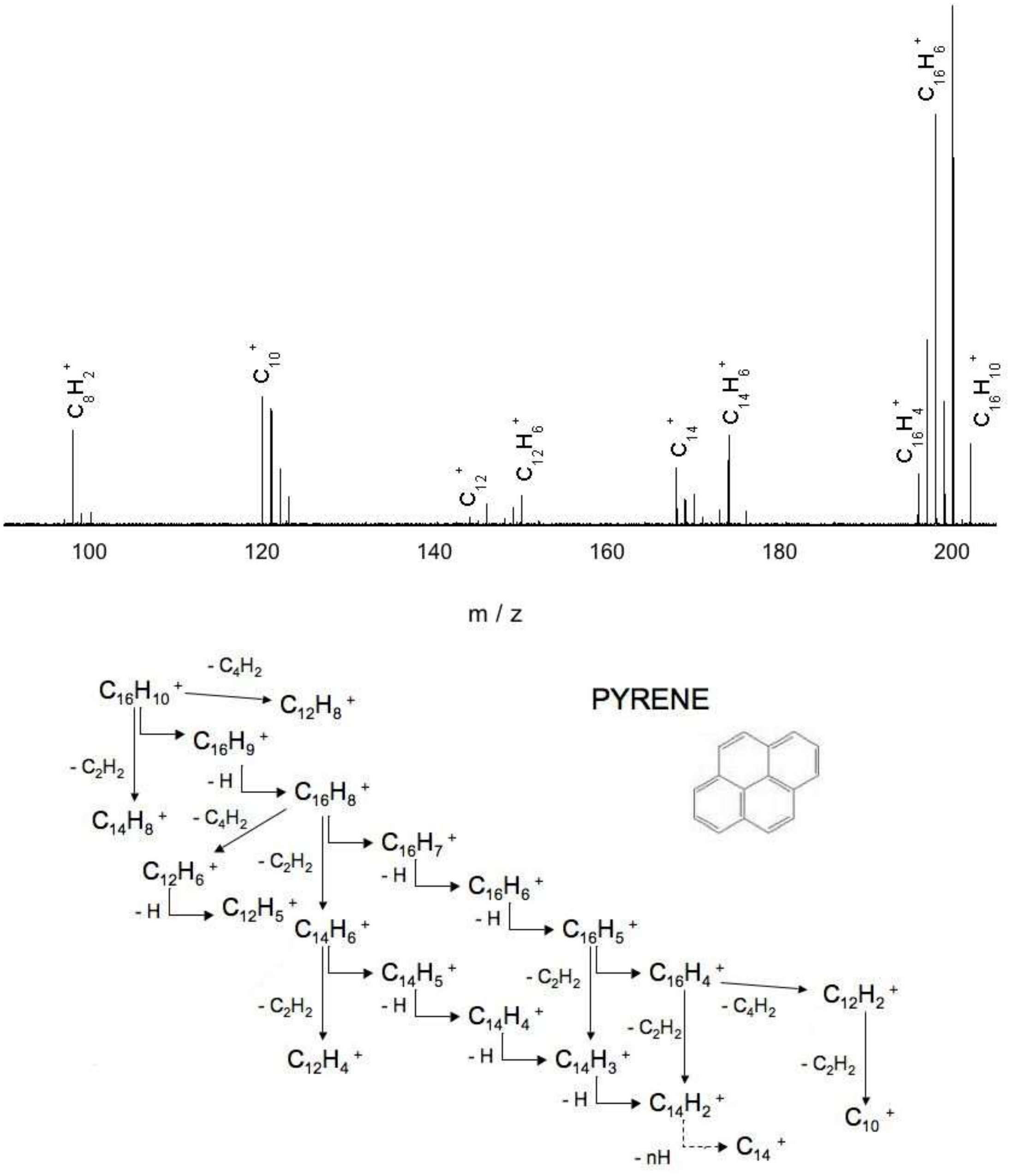

Figure 3.3: Top: FT-ICR mass spectrum of the pyrene cation after 10 s of irradiation with the Xe arc lamp. Bottom: identified pyrene photodissociation paths.

Longer irradiation up to one minute was performed. This led to the formation of decreasing in size hydrocarbon and carbon cluster cations down to C_7^+ (cf. Table 3.1).

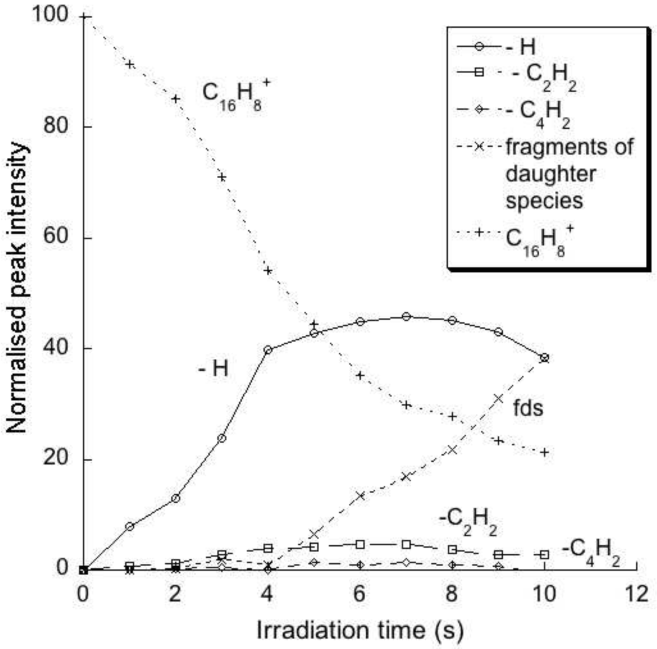

Figure 3.4: Normalised intensities of ${C_{16}H_8}^+$ (m/z = 200) and its photofragments as a function of irradiation time.

3.3.2 The Perylene cation (${C_{20}H_{12}}^+$, m/z = 252)

In the top panel of Fig. 3.5 we show the photofragmentation spectrum of ${C_{20}H_{12}}^+$ recorded after 1 s of irradiation with the Xe arc lamp. Three major peaks are observed at respectively m/z = 251, m/z = 250 and m/z = 226. The primary dissociation channel appears to be the loss of a single hydrogen atom, similarly to what is observed for the pyrene cation. Mass selective ejection is used to identify further dissociation paths, in particular possible loss of H_2 (or 2H atoms) is investigated. We have performed irradiation of the perylene cation with the m/z = 251 ions simultaneously ejected (cf. Fig. 3.5), the m/z = 250 peak is significantly decreased showing that most of dehydrogenation occurs by sequential H loss as shown on coronene ($C_{24}H_{12}$) by Joblin et al. (2009). In the same spectrum we can also notice the presence of the m/z = 226 peak (${C_{18}H_{10}}^+$) produced by acetylene loss from the parent ions (cf. the bottom panel of Fig. 3.5). Longer irradiation times (up to one minute) lead to further dehydrogenation of the parent species (dehydrogenation up to eight hydrogen atoms was observed). These results are consistent with previous studies performed by Ekern et al. (Ekern et al. 1998). We did not

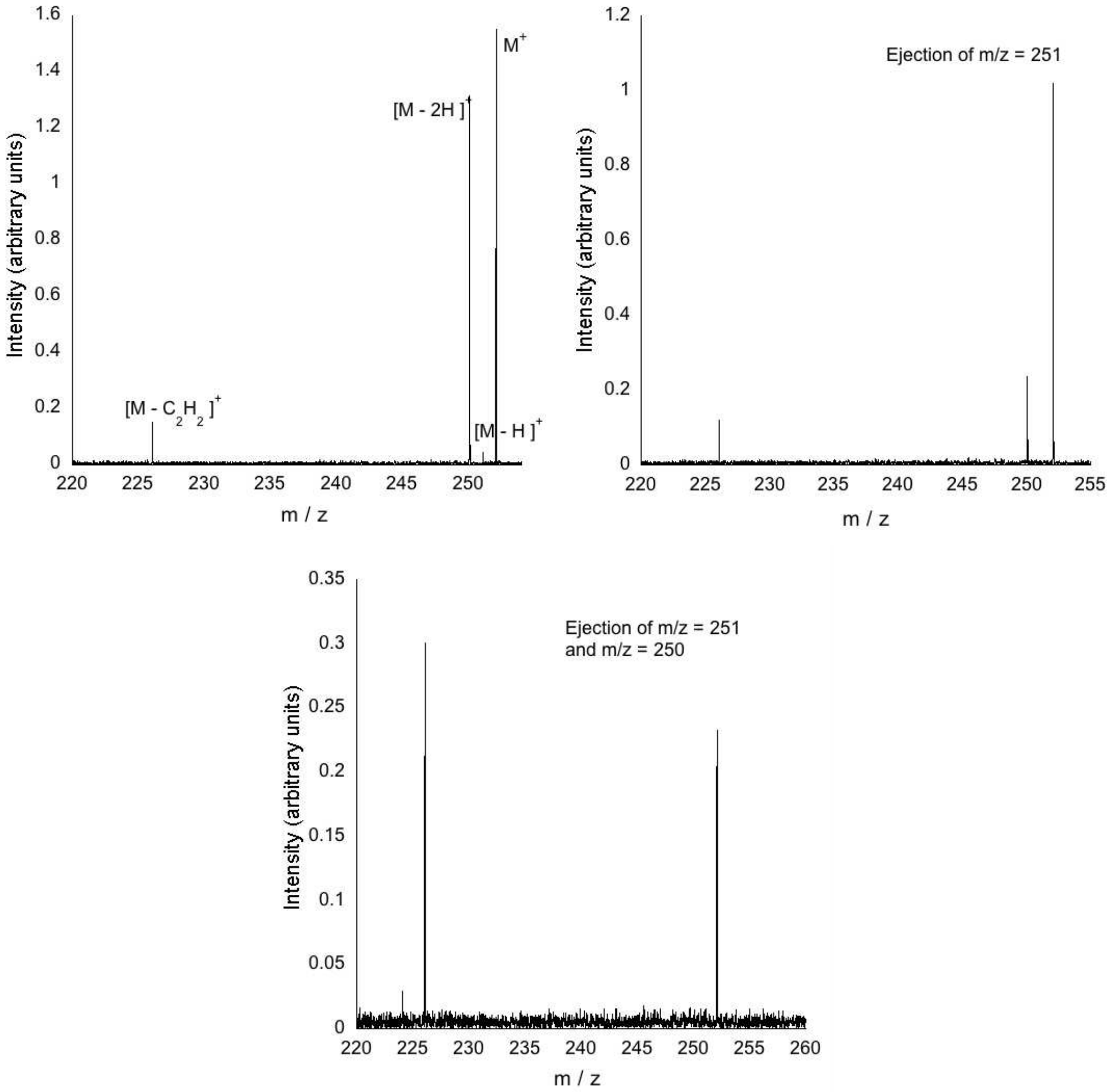

Figure 3.5: Top left: FT-ICR mass spectrum of the perylene cation (m/z 252) after 1 s of irradiation with the Xe arc lamp. Top right: Investigation of the fragmentation pathways of $C_{20}H_{12}^{+}$ parent ions through ejection of particular fragment ions during the lamp irradiation; FT-ICR spectrum taken after 1 s of irradiation with simultaneous ejection of the m/z = 251 ions. Bottom: FT-ICR spectrum taken after 8 s of irradiation with simultaneous ejection of the m/z = 251 and m/z = 250 ions. The m/z = 226 peak indicates the loss of an acetylene (C_2H_2) molecule from the parent ions.

observe, in this case, the formation of carbon clusters but this was probably due to a reduced reflectivity of the elliptical mirror which focuses the lamp radiation at the centre of the trap when

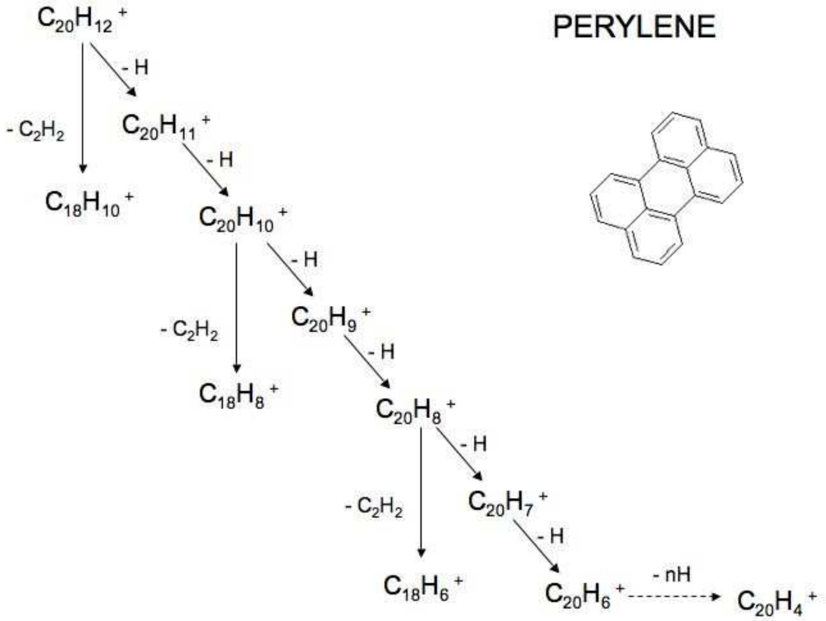

Figure 3.6: Perylene photodissociation patterns.

we performed the experiment. The identified photodissociation paths are illustrated in Fig. 3.6.

3.3.3 The Pentacene cation ($C_{22}H_{14}{}^+$, m/z = 278)

Continuous irradiation of the pentacene cation leads to dehydrogenation of the parent ion up to ten hydrogen atoms and to the formation of several hydrocarbons and carbon cluster ions (cf. Fig. 3.7). Interestingly, as observed also for the two PAHs previously examined, pyrene and perylene, the partial dehydrogenation of the parent ions ends up with the production of $C_nH_4{}^+$. The absence of more dehydrogenated species suggests that further photodissociation step will proceed through destruction of the carbon skeleton possibly involving a structural rearrangement.

The main identified dissociation patterns in the case of the pentacene cation dissociation cascade are the loss of a single hydrogen atom, the loss of an acetylene molecule and the loss of C_nH_m molecules with $n = 1, 2$. In particular the loss of C_2H_4 from the pentacene parent ion was evidenced through selective ejection of the other daughter species during irradiation. Moreover the loss of CH$_n$ species appears to be responsible for the formation of the C_{21}^+ carbon cluster from the dehydrogenated pentacene fragments. All the other smaller carbon clusters observed in the cascade likely originate from the fragmentation of C_{21}^+. Among them C_{10}^+ is the species that exhibits the most intense peak.

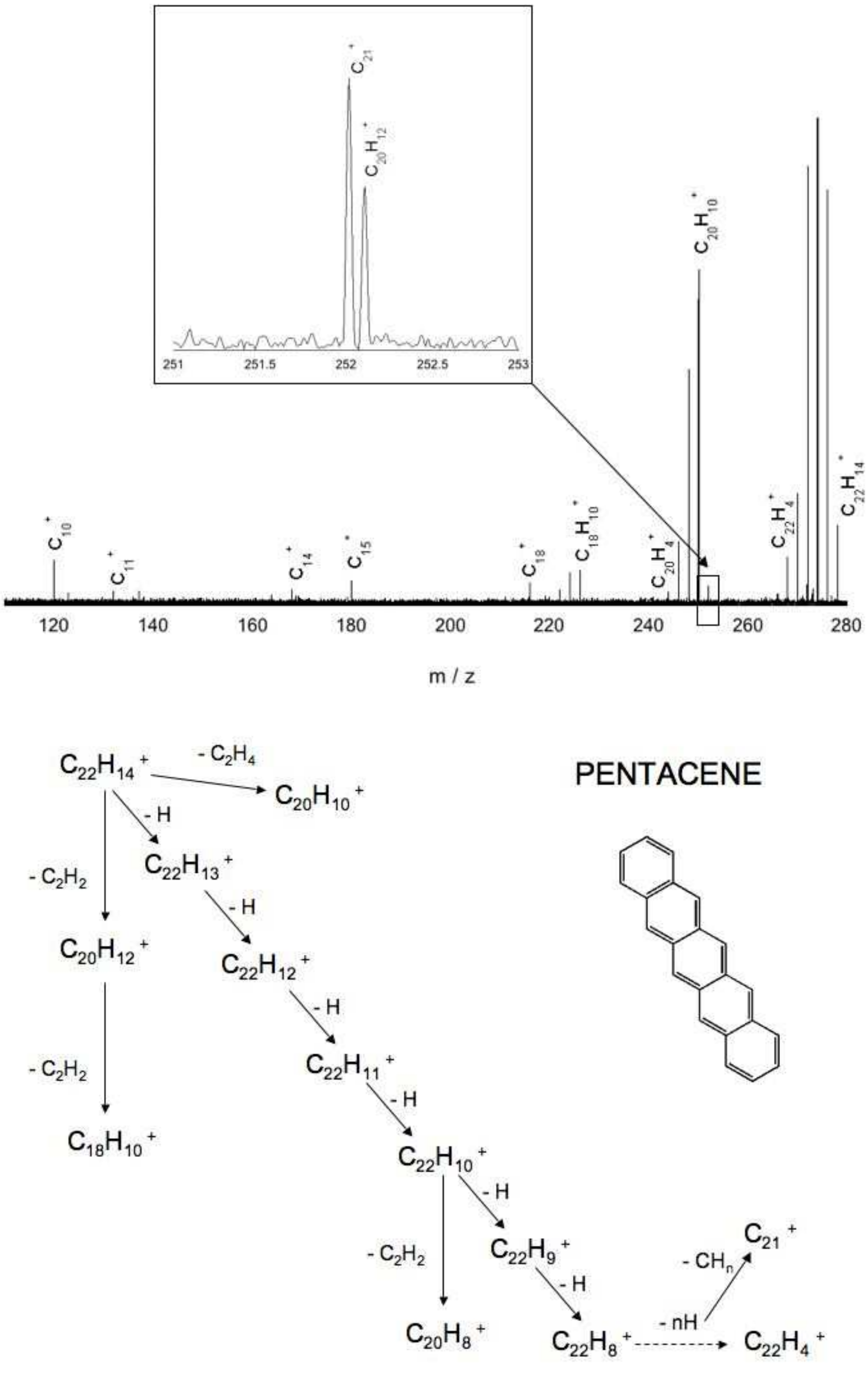

Figure 3.7: Top: FT-ICR mass spectrum of the pentacene cation after 1 minute of irradiation with the Xe arc lamp. The zoom on the spectrum evidences the presence of two separate peaks at slightly different m/z values: m/z = 252.00 (C_{21}^{+}) and m/z = 252.09 ($C_{20}H_{12}{}^{+}$). Bottom: identified pentacene photodissociation paths.

3.3.4 The Naphtho[2,3-a]Pyrene cation (${C_{24}H_{14}}^{+}$, m/z = 302)

Previous work has shown that the naphtho[2,3-a]pyrene cation completely dehydrogenates when exposed to irradiation by the Xe arc lamp (Ekern et al. 1997). This behaviour is confirmed also by our experiment, however, contrary to what previously observed, the destruction of the carbon skeleton occurs before completely dehydrogenation of the parent ions as shown in Fig. 3.9 where fragments having mass-to-charge ratio lower than m/z = 288 (C_{24}^{+}) are already distinguishable before the formation of this carbon cluster.
The global photodissociation cascade of the naphtho[2,3-a]pyrene cation after one minute of irradiation with the Xe arc lamp is displayed in Fig. 3.8. The origin of each observed peak was investigated, as usual, through isolation of selected species and selective ejection of fragments during irradiation. The identified photodissociation patterns are illustrated in Fig. 3.8. The formation of several carbon clusters proceeds in this case from the common progenitor C_{24}^{+}. The strongest peak, among these carbon clusters, appears to be the one corresponding to C_{14}^{+}, as already observed by Joblin (2003). The different C_{24}^{+} isomeric forms are not distinguishable by mass spectrometry, and several of them could probably be simultaneously produced in our experiment (cf. Sect. 4.8). We can therefore expect different dissociation paths for these species involving the loss of C, C_2 and C_3 fragments.

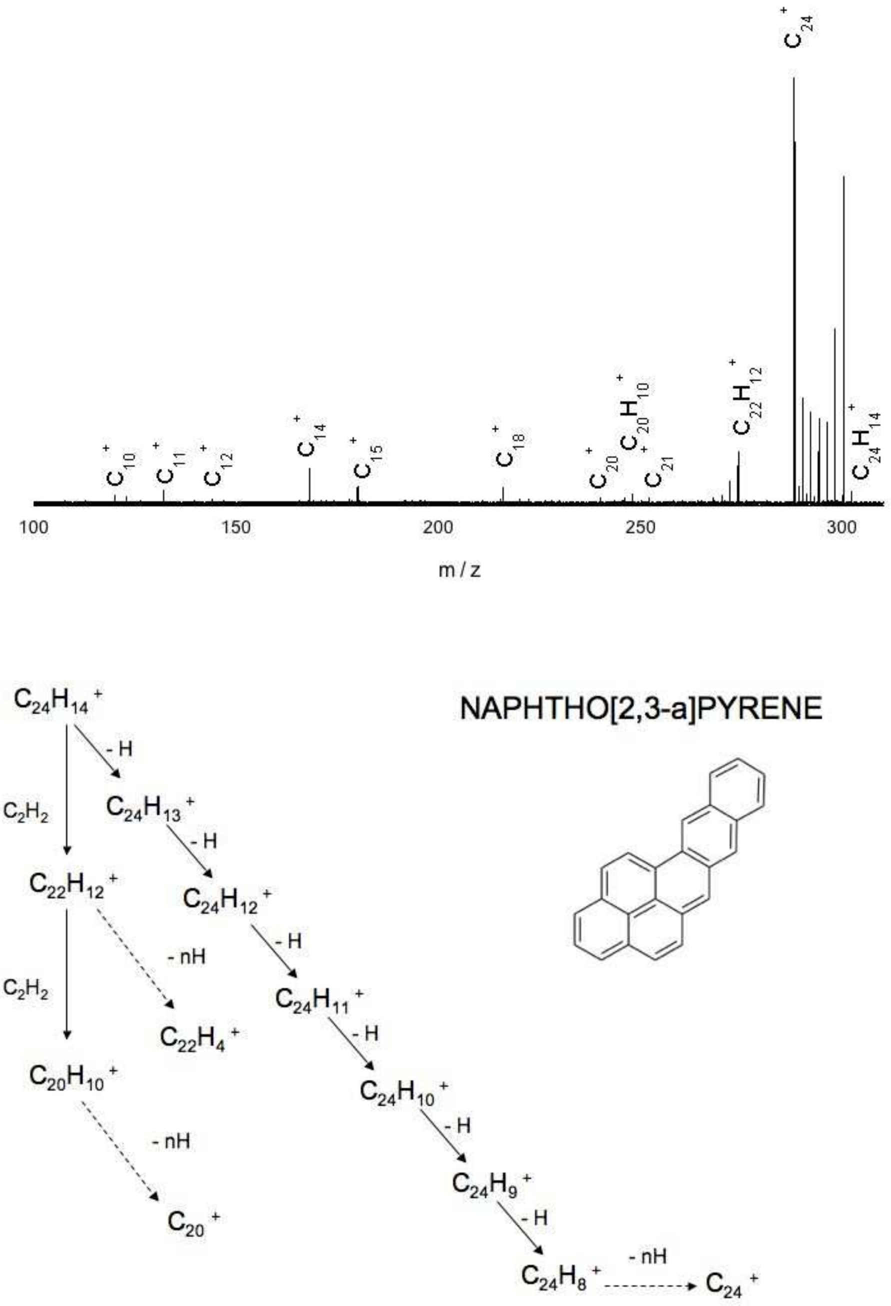

Figure 3.8: Top: FT-ICR mass spectrum of the naphtho[2,3-a]pyrene cation after 1 minute of irradiation with the Xe arc lamp. Bottom: proposed photodissociation pathways for the naphtho[2,3-a]pyrene cation.

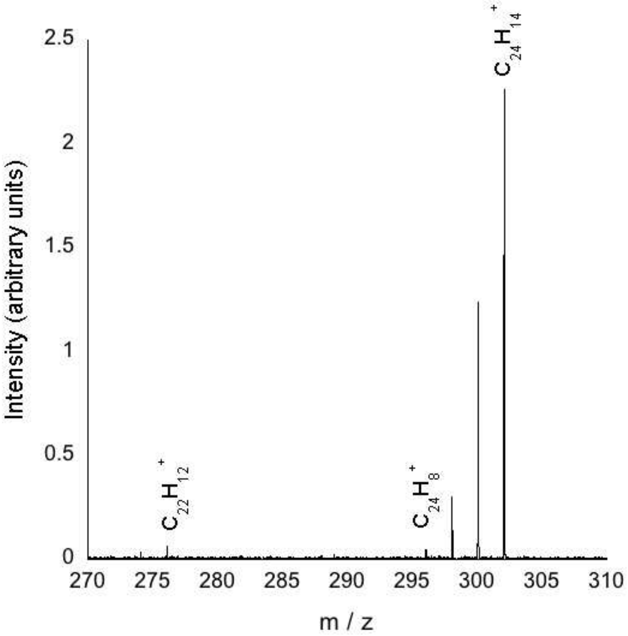

Figure 3.9: FT-ICR mass spectrum of $C_{24}H_{14}{}^{+}$, naphtho[2,3-a]pyrene cation, after 10 s of irradiation with the Xe arc lamp. Formation of the $C_{22}H_{12}{}^{+}$ fragment species is observed.

3.4 Discussion

Comparing the results obtained for the four medium-sized PAH cations examined here, we can draw some general conclusions on the behaviour of these species exposed to the continuous irradiation from a Xe arc lamp. The experiment probes the energy region where fragmentation is in competition with radiative cooling, so a key region for the study of the survival of PAHs in the interstellar medium. Stepwise elimination of single hydrogen atoms appears as the main dissociation pathway for all the considered species.

Complete dehydrogenation of the parent ion was observed only for the naphtho[2,3-a]pyrene species while all the other examined cations showed only partial dehydrogenation ending up with the production of $C_nH_4{}^{+}$ species. Studies on the structures and formation of $C_nH_x{}^{+}$ species by Lee et al. (1997), in a laser desorption ion source, have shown that a new bicyclic isomer appears at $n = 15$ for $x \geq 4$ during the formation process of these species and that this isomer became more rapidly abundant with increasing n suppressing both linear and monocyclic structures in most cases. Calculations of the stable structures of $C_{16}H_4{}^{+}$ isomers also confirm that the bicyclic structure is, for this species, the most stable one (Lee et al. 1997). A structural rearrangement could then be responsible for the absence of dehydrogenation from $C_nH_4{}^{+}$ species.

Besides hydrogen atom loss, acetylene molecule loss was observed for all the studied species. This fragmentation pathway is expected in the case of non compact PAHs but there are several exceptions at this behaviour (Ekern et al. 1998). The pyrene cation, being a compact PAH, seems here to be an exception.

The C_2H_2 dissociation pathway was mainly observed from the even-mass fragments ${C_nH_{2m}}^+$. Species with an odd number of hydrogen atoms are, in fact, expected to be more fragile and to easily lose one H as observed for ${C_{24}H_{2n+1}}^+$ species (n = 0 - 5) by Joblin et al. (2009). Further dissociation reactions were also evidenced: the loss of a diacetylene molecule in the case of the pyrene cation and the loss of CH_n and C_2H_4 species in the case of the pentacene cation. These dissociation pathways were already observed for these species in CID experiments (Shushan & Boyd 1980).

An inventory of the fragments produced in the photodissociation cascades of the four different PAH cations studied here is presented in Table 3.1. Formation of carbon clusters ions is observed for all the studied species. Different dissociation paths can be inferred mainly involving the loss of C, C_2 and C_3 neutral fragments. In particular it must be noticed that the presence of C_{14}^+ in the dissociation cascade always entails the detection of C_{11}^+ and C_{10}^+ species while C_{18}^+ is responsible for the formation of C_{15}^+. These observations are consistent with previous photodissociation studies on ${C_n}^+$ by Geusic et al. (1987) and Pozniak & Dunbar (1997).

The results obtained here put forward the possible contribution of medium-sized ($N_c \leq 24$) PAH dissociation to the formation of small hydrocarbons and carbon clusters. As already emphasised by Allain et al. (1996), the loss of C_2H_2 appears as the main channel for the destruction of the carbon skeleton of PAHs. Still, an important aspect to consider is the competition between dehydrogenation and recombination with H atoms that can be efficient in interstellar environments considering the high abundance of H atoms. This competition has an essential role in the survival of the carbon skeleton since highly dehydrogenated forms may rapidly isomerise into bicyclic forms that photodissociate through carbon loss.

Le Page et al. (2001, 2003) developed a model to study the hydrogen coverage of PAHs calculating the equilibrium between the processes of photodissociation and recombination with hydrogen atoms. The authors found that small PAHs with fewer than about 15-20 carbon atoms are quickly destroyed in the normal UV field, while intermediate-size PAHs (20-30 carbon atoms) lose most of their peripheral hydrogen atoms and larger PAHs may be fully hydrogenated and even surhydrogenated with competition from the protonated form. It must be noticed, however, that the carbon loss channel has been neglected in this model. Our results have shown that acetylene loss can be an important fragmentation channel for medium-sized PAHs and it should then be taken into account.

Quantitative studies on the photophysics of each ion would be necessary to use the results presented here in astrophysical models. These studies would require, in particular, the determination, for each species, of molecular parameters such as the absorption cross sections at the different wavelengths considered, the photodissociation rates, the branching ratios (fractions of parent ions which fragment through each individual fragmentation path) and the threshold energies for dissociation.

PYRENE		PERYLENE		PENTACENE		NAPHTHO[2,3-a]PYRENE	
				Fragments			
m/z	Formula	m/z	Formula	m/z	Formula	m/z	Formula
201	$C_{16}H_{9}{}^{+}$	251	$C_{20}H_{11}{}^{+}$	277	$C_{22}H_{13}{}^{+}$	301	$C_{24}H_{13}{}^{+}$
200	$C_{16}H_{8}{}^{+}$	250	$C_{20}H_{10}{}^{+}$	276	$C_{22}H_{12}{}^{+}$	300	$C_{24}H_{12}{}^{+}$
199	$C_{16}H_{7}{}^{+}$	249	$C_{20}H_{9}{}^{+}$	275	$C_{22}H_{11}{}^{+}$	299	$C_{24}H_{11}{}^{+}$
198	$C_{16}H_{6}{}^{+}$	248	$C_{20}H_{8}{}^{+}$	274	$C_{22}H_{10}{}^{+}$	298	$C_{24}H_{10}{}^{+}$
197	$C_{16}H_{5}{}^{+}$	247	$C_{20}H_{7}{}^{+}$	273	$C_{22}H_{9}{}^{+}$	297	$C_{24}H_{9}{}^{+}$
196	$C_{16}H_{4}{}^{+}$	246	$C_{20}H_{6}{}^{+}$	272	$C_{22}H_{8}{}^{+}$	296	$C_{24}H_{8}{}^{+}$
176	$C_{14}H_{8}{}^{+}$	245	$C_{20}H_{5}{}^{+}$	271	$C_{22}H_{7}{}^{+}$	295	$C_{24}H_{7}{}^{+}$
174	$C_{14}H_{6}{}^{+}$	244	$C_{20}H_{4}{}^{+}$	270	$C_{22}H_{6}{}^{+}$	294	$C_{24}H_{6}{}^{+}$
173	$C_{14}H_{5}{}^{+}$	226	$C_{18}H_{10}{}^{+}$	269	$C_{22}H_{5}{}^{+}$	293	$C_{24}H_{5}{}^{+}$
172	$C_{14}H_{4}{}^{+}$	224	$C_{18}H_{8}{}^{+}$	268	$C_{22}H_{4}{}^{+}$	292	$C_{24}H_{4}{}^{+}$
171	$C_{14}H_{3}{}^{+}$	222	$C_{18}H_{6}{}^{+}$	252	$C_{20}H_{12}{}^{+}$	291	$C_{24}H_{3}{}^{+}$
170	$C_{14}H_{2}{}^{+}$			252	$C_{21}{}^{+}$	290	$C_{24}H_{2}{}^{+}$
169	$C_{14}H^{+}$			250	$C_{20}H_{10}{}^{+}$	289	$C_{24}H^{+}$
168	$C_{14}{}^{+}$			248	$C_{20}H_{8}{}^{+}$	288	$C_{24}{}^{+}$
152	$C_{12}H_{8}{}^{+}$			246	$C_{20}H_{6}{}^{+}$	276	$C_{22}H_{12}{}^{+}$
150	$C_{12}H_{6}{}^{+}$			240	$C_{20}H_{4}{}^{+}$	274	$C_{22}H_{10}{}^{+}$
149	$C_{12}H_{5}{}^{+}$			226	$C_{18}H_{10}{}^{+}$	272	$C_{22}H_{8}{}^{+}$
148	$C_{12}H_{4}{}^{+}$			224	$C_{18}H_{8}{}^{+}$	270	$C_{22}H_{6}{}^{+}$
146	$C_{12}H_{2}{}^{+}$			222	$C_{18}H_{6}{}^{+}$	268	$C_{22}H_{4}{}^{+}$
144	$C_{12}{}^{+}$			216	$C_{18}{}^{+}$	266	$C_{22}H_{2}{}^{+}$
132	$C_{11}{}^{+}$			180	$C_{15}{}^{+}$	252	$C_{20}H_{12}{}^{+}$
123	$C_{10}H_{3}{}^{+}$			168	$C_{14}{}^{+}$	250	$C_{20}H_{10}{}^{+}$
122	$C_{10}H_{2}{}^{+}$			132	$C_{11}{}^{+}$	248	$C_{20}H_{8}{}^{+}$
121	$C_{10}H^{+}$			120	$C_{10}{}^{+}$	246	$C_{20}H_{6}{}^{+}$
120	$C_{10}{}^{+}$					240	$C_{20}{}^{+}$
100	$C_{8}H_{4}{}^{+}$					216	$C_{18}{}^{+}$
99	$C_{8}H_{3}{}^{+}$					180	$C_{15}{}^{+}$
98	$C_{8}H_{2}{}^{+}$					168	$C_{14}{}^{+}$
97	$C_{8}H^{+}$					144	$C_{12}{}^{+}$
85	$C_{7}H^{+}$					132	$C_{11}{}^{+}$
84	$C_{7}{}^{+}$					120	$C_{10}{}^{+}$

Table 3.1: List of the fragments detected in the photodissociation cascade of each of the four considered PAH cations: pyrene $C_{16}H_{10}{}^{+}$, perylene $C_{20}H_{12}{}^{+}$, pentacene $C_{22}H_{14}{}^{+}$ and naphtho[2,3-a]pyrene $C_{24}H_{14}{}^{+}$.

Chapter 4

Visible photodissociation spectroscopy of PAH^+

Per aspera ad astra.
Through difficulties to the stars.

4.1 Diffuse Interstellar Bands and PAHs: the astrophysical problem

Diffuse Interstellar Bands (DIBs) are a set of discrete absorption features superposed on the interstellar extinction curve. The first two bands were discovered in 1921 by Heger (1921) and nowadays close to 400 DIBs are catalogued (Hobbs et al. 2008). Since Merrill (Merrill 1934), who first recognised them as ubiquitous interstellar features, DIBs were seen towards more than a hundred sight lines, showing varying relative strengths from one environment to another. They fall in the range from ~ 0.4 to ~ 1.3 μm, and exhibit a full width at half maximum ranging from less than 1 up to 40 Å (Tielens & Snow 1995). The correlation between their intensity and the interstellar extinction constrains their origin to the interstellar medium, while their independence towards light polarisation (caused by interaction between starlight and the dust particles) is in favour of gas-phase carriers (Herbig 1995), however no definitive match between any DIB and any individual molecule still exists.

Potential DIB carriers proposed so far range from carbon chains (Maier 1998) to PAHs and their cations (Léger & D'Hendecourt 1985; van der Zwet & Allamandola 1985; Crawford et al. 1985; Allamandola et al. 1985; Salama et al. 1999), to fullerenes (Kroto & Jura 1992). PAH cations

seem to be the most promising candidates as carriers of the DIBs since these species have electronic transitions in the spectral region of interest, are stable against UV photo-dissociation and their estimated abundance is large enough to be consistent with the observed DIB strengths.
During the past two decades an extensive laboratory effort has been done to find the most suitable techniques to characterise the spectroscopic signatures of these species under conditions that are relevant for astrophysical applications. This represents a demanding experimental task because of the difficulty of producing and isolating such large nonvolatile and often reactive molecules and because of the huge number of possible candidates to test. In Chapter 1 we summarised the main spectroscopic techniques used so far to face this problem. In this chapter we report the study we performed to measure the visible multiphoton dissociation spectra of gas-phase cationic PAHs, produced and isolated in the PIRENEA ion trap mass spectrometer and irradiated with a mid-band OPO tunable laser.

4.2 Presentation of the study

4.2.1 Objectives

The purpose of our study is to obtain gas-phase spectroscopic data on different ionised PAHs and derivatives, that can be useful for the pre-selection of the most promising candidates for some of the DIBs. The band profile obtained with this technique is not that of cold ions, which is a necessary condition to match the experimental spectra to the astronomical ones and definitively identify DIB carriers. That is why the technique applied here can only be used to make a pre-selection of possible DIB candidates. However the coupling with the ICR cell allows to easily study various species including dehydrogenated PAH cations and carbon cluster cations.
We have investigated, in particular, the 430-480 nm spectral range in which the strongest optical DIB, the 4428 Å band, falls. In Fig. 4.1 we report a table which compares the characteristics of the electronic bands of cold gas-phase PAH ions measured so far to the characteristics of the strong 4428 Å DIB.

No successful identification was possible yet. This emphasises the need for more observational data and dedicated surveys on different interstellar environments and lines of sight, to correlate these bands with local physical conditions. From the laboratory point of view, there is a need for a systematic study on all the species considered as potential DIB carriers.
Using the PIRENEA set-up we have measured the MPD spectra of six different species of increasing size, namely the pyrene cation ($C_{16}H_{10}{}^+$), the 1–methylpyrene cation ($CH_3 - C_{16}H_9{}^+$), the coronene cation and its dehydrogenated derivatives ($C_{24}H_p{}^+$ with p= 0, 10, 11, 12) (see Fig. 4.2 and Fig. 4.10).

The matrix and gas-phase spectra of pyrene and 1–methylpyrene cations have already been

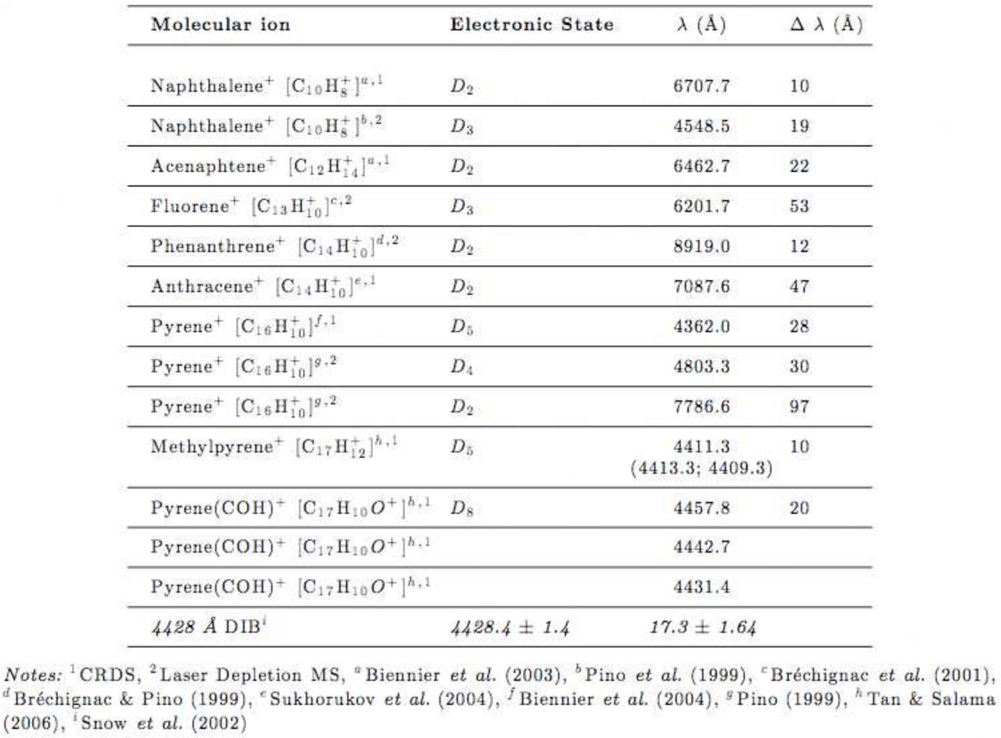

Molecular ion	Electronic State	λ (Å)	Δ λ (Å)
Naphthalene$^+$ $[C_{10}H_8^+]^{a,1}$	D_2	6707.7	10
Naphthalene$^+$ $[C_{10}H_8^+]^{b,2}$	D_3	4548.5	19
Acenaphtene$^+$ $[C_{12}H_{14}^+]^{a,1}$	D_2	6462.7	22
Fluorene$^+$ $[C_{13}H_{10}^+]^{c,2}$	D_3	6201.7	53
Phenanthrene$^+$ $[C_{14}H_{10}^+]^{d,2}$	D_2	8919.0	12
Anthracene$^+$ $[C_{14}H_{10}^+]^{e,1}$	D_2	7087.6	47
Pyrene$^+$ $[C_{16}H_{10}^+]^{f,1}$	D_5	4362.0	28
Pyrene$^+$ $[C_{16}H_{10}^+]^{g,2}$	D_4	4803.3	30
Pyrene$^+$ $[C_{16}H_{10}^+]^{g,2}$	D_2	7786.6	97
Methylpyrene$^+$ $[C_{17}H_{12}^+]^{h,1}$	D_5	4411.3 (4413.3; 4409.3)	10
Pyrene(COH)$^+$ $[C_{17}H_{10}O^+]^{h,1}$	D_8	4457.8	20
Pyrene(COH)$^+$ $[C_{17}H_{10}O^+]^{h,1}$		4442.7	
Pyrene(COH)$^+$ $[C_{17}H_{10}O^+]^{h,1}$		4431.4	
4428 Å DIB^i	*4428.4 ± 1.4*	*17.3 ± 1.64*	

Notes: ^{1}CRDS, ^{2}Laser Depletion MS, ^{a}Biennier *et al.* (2003), ^{b}Pino *et al.* (1999), ^{c}Bréchignac *et al.* (2001), ^{d}Bréchignac & Pino (1999), ^{e}Sukhorukov *et al.* (2004), ^{f}Biennier *et al.* (2004), ^{g}Pino (1999), ^{h}Tan & Salama (2006), ^{i}Snow *et al.* (2002)

Figure 4.1: Electronic state peak positions and band widths of cold gas-phase PAH ions measured in the laboratory and compared to the characteristics of the strong 4428 Å DIB (Figure taken from Salama (2008)).

measured before. The comparison of our measurements with these data and, in particular, with gas-phase data on cold ions, allows us to assess the validity of our experimental method in obtaining the band positions. In the case of the coronene cation and its dehydrogenated derivatives, including ${C_{24}}^+$ that has recently been proposed among the possible candidates for some of the DIBs, including the 4428 Å DIB (Duley 2006), the spectra measured here are the first available data in the gas-phase.

All the experimental data are complemented with the use of time-dependent density functional theory (TD-DFT) calculations, which allow us to identify the measured bands.

The ionic species produced with our technique can include different isomeric forms (species with the same chemical formula but different structures). This aspect is investigated in the case of ${C_{24}}^+$ for which we have computed the electronic spectra of different isomers and compared them to the measured experimental spectrum. Finally, a modelling study is performed at the end of the chapter to derive the absorption cross-sections. The measured action spectra do not provide direct information on the absorption cross-section of the ions however this latter is related to the measured dissociation yield and we will show that it can be derived from the

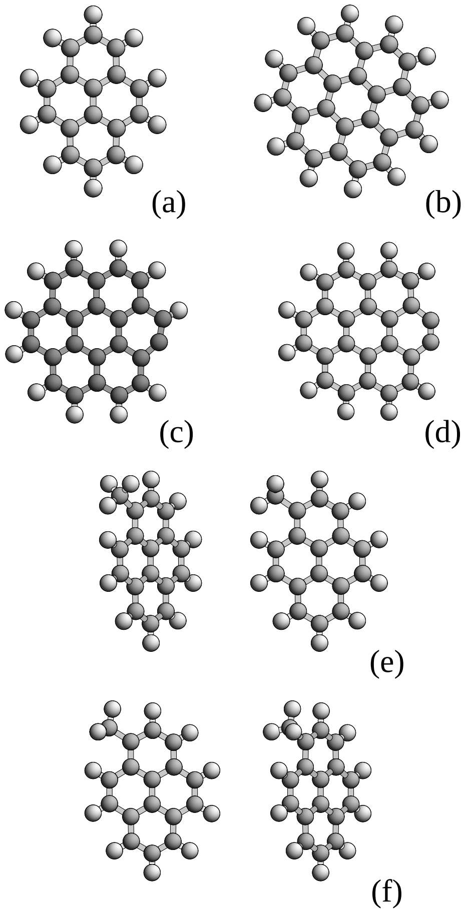

Figure 4.2: Structures of the studied molecules: (a) pyrene cation; (b) coronene cation; (c) simply dehydrogenated coronene cation; (d) doubly dehydrogenated coronene cation; (e) and (f) the two stable conformations of the 1–methylpyrene cation, each viewed from two different angles to better show the 3–D configuration of the methyl group.

experimental data by describing the photophysics of the ions in our experimental conditions, as illustrated for two of the studied species: the coronene and the pyrene cations.

4.2.2 Experimental procedure

As previously described, PAH molecular ions are produced in the PIRENEA set-up by laser ablation-ionisation from a solid target and trapped in the ICR cell. The species of interest can then be selected by ejection of all the unwanted species (isotopomers and parent ions if the species of interest is a fragment). Dehydrogenated species can be formed in the ICR cell by UV-photofragmentation of the parent ion with the Xe arc lamp and then mass-selected. As seen in chapter 2 in the selective ejection process the ion cloud is perturbed to some extent making it necessary to inject buffer gas (He) in order to relax it.

Once cooled down, selected ions are irradiated with the OPO laser. At the beginning of each experiment, preliminary tests are systematically made to optimise the ion signal, the laser energy that has to be used to perform dissociation and the overlap between the laser spot and the ion cloud (see section 4.4). The spectra are recorded monitoring the relative fragmentation yield of the species (ratio between the photofragment abundance and the total abundance of ions, parent ion plus photofragments) as a function of the OPO laser wavelength. The Panther EX laser was used to perform dissociation of all the species apart from $C_{24}H_{11}{}^{+}$ and $C_{24}{}^{+}$ whose spectra were recorded using the broad band Surelite OPO laser that was initially the only one available on the experimental set-up. We have scanned with the laser the spectral range between 430 and 480 nm, with a 2 nm scan step, recording a 10 mass-spectra average (10 laser cycles) at each wavelength. The laser energy is generally kept constant during the wavelength scan with the exception of the $C_{24}{}^{+}$ spectrum (see discussion in section 4.8). The recorded spectra are discussed separately in the next sections.

4.2.3 Computational details

To help the interpretation of the measured spectra we computed the energies and intensities for vertical transitions to the low-lying electronic states of the species under investigation. We used the density functional theory (DFT) (Hohenberg & Kohn 1964; Kohn & Sham 1965; Jones & Gunnarsson 1989) and its time-dependent extension (TD-DFT) (Runge & Gross 1984; Casida 1995; Bauernschmitt & Ahlrichs 1996), which are the methods of choice for such large molecules. We used the `TURBOMOLE V6.0.1` package (Ahlrichs et al. 1989) making use of the resolution of identity approximation for computing the electronic Coulomb interaction (Eichkorn et al. 1995). This approach is based on the expansion of molecular electron densities in a set of atom-centered auxiliary basis sets leading to expressions involving three-center electron repulsion integrals; this usually leads to a more than tenfold speedup compared to the conventional method based on four-center electron repulsion integrals.

The calculation of the electronic absorption spectra requires the previous knowledge of the ground-state optimised geometries. In all cases, with the exception of coronene cation (see section 4.3.3), no symmetry constraints were adopted by assuming the C_1 point group. The ground-state of the pyrene cation ($C_{16}H_{10}{}^{+}$), 1-methylpyrene cation ($CH_3 - C_{16}H_9{}^{+}$), coronene cation ($C_{24}H_{12}{}^{+}$), $C_{24}H_{10}{}^{+}$ and $C_{24}{}^{+}$ was found to be a doublet, while for $C_{24}H_{11}{}^{+}$ our calculations predict a triplet ground-state.

Based on calibration calculations performed for small PAHs, we used the split valence polarisation (SVP) basis set (Schafer et al. 1992) in conjunction with the BP86 exchange-correlation functional, a combination of the Becke's 1988 exchange functional (Becke 1988), and the

Vosko-Wilk-Nusair (Vosko et al. 1980) and Perdew's 1986 (Perdew 1986) correlation functionals. Despite the smallness of the basis set, the computed transition energies in the spectral range of interest (430 - 480 nm) are found to be systematically in closer agreement with experiments as compared to results obtained with the larger basis TZVP of triple zeta valence quality (Schafer et al. 1994). Typical errors in the computed values are of the order of a few tenths of eV.

4.3 Results

4.3.1 The pyrene cation ($C_{16}H_{10}{}^+$)

The MPD spectrum of the pyrene cation (see (a) in Fig. 4.2) measured with the PIRENEA experiment is shown in Fig. 4.3. We have recorded fragmentation of the ions after one laser pulse with a laser energy of 6 mJ.

We can distinguish in the spectrum a main band at about 436 nm followed by two other peaks at about 444 and 450 nm. The band measured at 436 nm compares quite well with measurements in the gas phase made by Biennier (2004) who assigned this feature to the (0-0) vibrational band of the $D_5 \longleftarrow D_0$ electronic transition (cf. Table 4.1). Our spectrum is also in good agreement with neon-matrix data taken by Salama & Allamandola (1992). The blue shift of about 3.5 nm that we measure relative to the matrix spectrum is consistent with the shifts measured by Biennier (2004) and with the predicted limits of the neon-matrix to gas-phase shift (Romanini et al. 1999; Salama et al. 1999).

Our theoretical calculations predict, in the considered spectral range, one electronic transition at 426 nm, with an oscillator strength f = 0.206 (cf. Table 4.1). This value is in line with previous calculations made by Hirata et al. (1999) and is in very good agreement with our experimental result ($\Delta\lambda$ = 10 nm or ΔE = 0.07 eV with respect to our measured position).

The two features observed at 444 and 450 nm are probably a vibronic progression of the observed electronic transition, since our calculations do not predict any other suitable electronic transition in this energy range. The fact that they are on the red side of the 0–0 band probably means that they are hot bands of the same electronic transition, in which the absorption takes place from a vibrationally excited state of the D_0 electronic state to a vibrationally less excited state of the D_5 electronic state. This indicates that the studied ions were initially carrying some internal energy possibly transferred to them during the collisions with the buffer gas. The buffer gas, injected to enable the ions to exchange kinetic energy with the cold walls of the trap so that the cloud can cool down, mediates, as a side effect, the exchange of energy among translational and internal degrees of freedom of the molecules. Therefore if the ion cloud has a large residual energy, this can populate significantly some vibrational levels of the ions.

More vibronic structure can be present on the blue side of the band origin but we have not detected it because it is outside the probed spectral range.

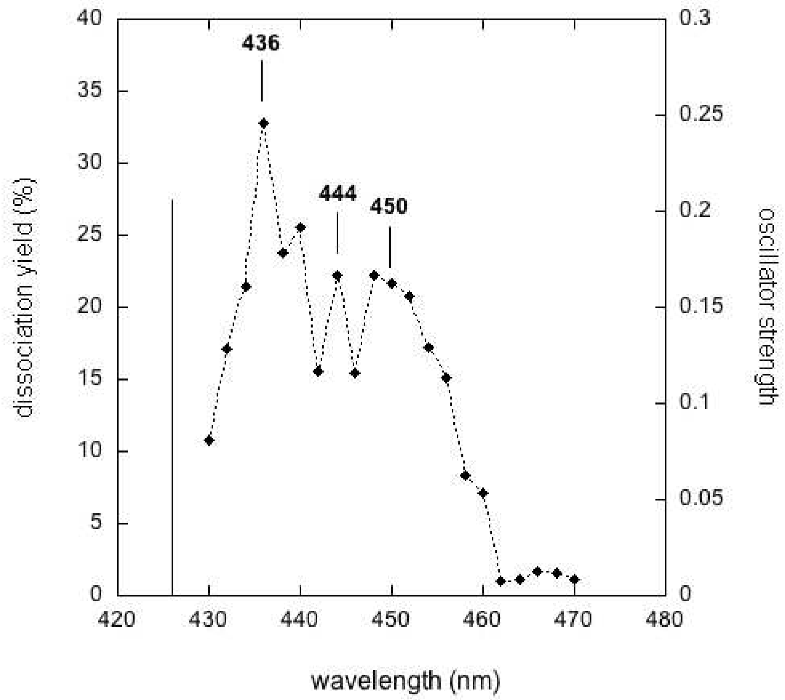

Figure 4.3: MPD spectrum of gas-phase pyrene cation isolated in the ICR cell of PIRENEA. Computed transitions are superimposed on the experimental spectrum and represented by vertical bars with an height proportional to the computed oscillator strength.

4.3.2 The 1–methylpyrene cation ($CH_3 - C_{16}H_9{}^+$)

Figure 4.4 shows the spectrum measured for the 1–methylpyrene cation. We performed experiments with one laser pulse, with a laser energy of 3 mJ. The recorded spectrum presents three bands at the following positions: 442, 454 and 480 nm.

We can compare our results with the spectrum of UV-irradiated 1-methylpyrene isolated in a neon matrix recorded by Léger et al. (1995) (cf. Table 4.1). The authors measured four bands respectively at 418, 444, 456 and 482.5 nm. Considering that some of the species present in the matrix could be PAH radicals that have lost an H atom, the authors incorporated atomic hydrogen (H^0) in the matrix and examined the evolution of the relative intensities of the bands

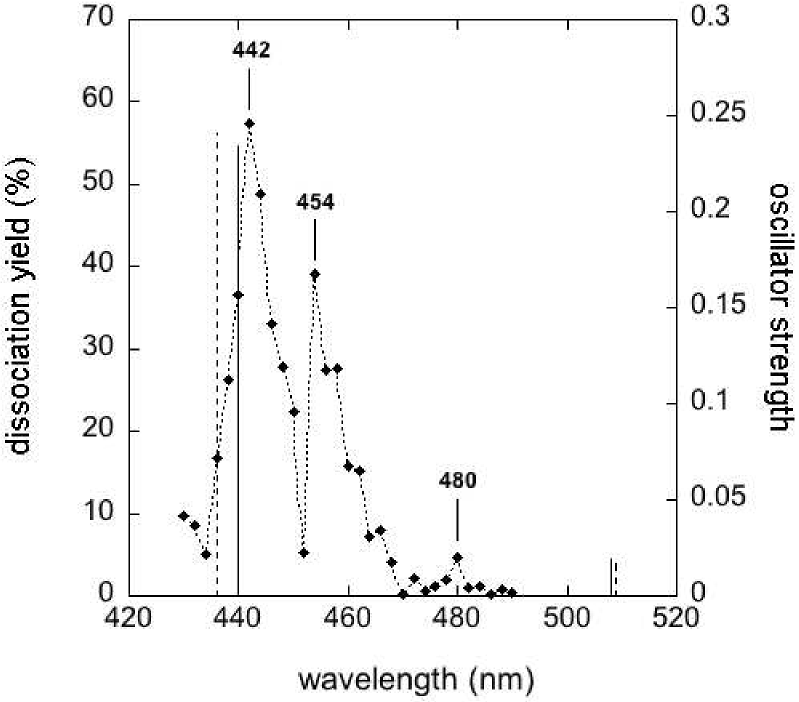

Figure 4.4: MPD spectrum of gas-phase 1–methylpyrene cation measured with the PIRENEA set-up. The electronic transitions calculated for the two different isomers (e) and (f) (see Fig. 4.2) are represented in continuous and dashed lines, respectively.

in order to determine to which species they belong. They therefore tentatively attributed to the 1–methylene –pyrene cation, presumably formed inside the matrix after irradiation, all the above-mentioned bands apart from the one at 456 nm ascribed to 1–methylpyrene cation.

Taking into account the precision of our technique and the matrix to gas-phase shift, all these bands are likely to correspond, in position, to the bands measured in the matrix at 444, 456 and 482.5 nm. Band profiles and relative intensities also compare well with matrix data (cf. Léger et al. (1995)). The gas-phase spectrum of 1-methylpyrene cation has been previously measured by Tan & Salama (2006). The authors assigned to the $D_5 \longleftarrow D_0$ electronic transition of the molecule a spectral feature measured at ∼441 nm and estimated for it an oscillator strength $f \sim 0.2$. This value matches well with our theoretical calculations, which predict an electronic transition with the same oscillator strength at ∼440 nm (cf. Table 4.1) and with our experimental measurement. Unfortunately, the authors only report on a narrow spectral window around the ∼441 nm feature, saying nothing about the other features. Given the technique we use here, the additional features we see at 454 and 480 nm cannot be ascribed to the 1–methylene–pyrene cation, but only to the 1–methylpyrene cation. TD–DFT calculations, on the other hand, only predict one additional transition in that spectral region, namely the, $D_4 \longleftarrow D_0$, at a wavelength of 507 nm with an oscillator strength of $f = 1.9 \times 10^{-2}$. This band probably corresponds to the transition we observed at 480 nm. The band at 454 nm in our spectrum could, in principle, be due to hot bands, as discussed above for pyrene, but then it should not be present in the cold neon-matrix spectra. Our calculations show, however, that there are two stable configurations for the methyl group, differing by a 180^o rotation of the torsional angle (see (e) and (f) in Fig. 4.2).

The conformation (f) in Fig. 4.2 results to be marginally more stable by $\sim$0.04 eV, but such a difference is so small that it is within the error of DFT. With such a small energy difference, both structures can be expected to be simultanously present both in our experiment and in cold matrix spectra. Their electronic transitions differ slightly in position and intensity, so that all well–resolved bands are expected to be double. We therefore attribute the two bands at 442 and 454 nm to the same $D_5 \longleftarrow D_0$ transition, predicted to be at 436 nm with f = 0.241 for the (f) isomer and at 440 nm with f = 0.234 for the (e) isomer.

4.3.3 The coronene cation ($C_{24}H_{12}{}^{+}$)

Dissociation of the coronene cation (see (b) in Fig. 4.2) was performed with one OPO laser shot and with a laser energy of 14 mJ. Our spectrum (see Fig. 4.5) presents a broad feature at about 457 nm with some vibronic structure on the blue side of the band.

Identification of this band through comparison with theoretical calculations is not trivial for several reasons: with our experimental technique we have no information on the absolute intensity of the transition and the small spectral range analysed makes it difficult to unambiguously assign bands. To ease the problem of the small spectral window, we can first compare calculations with experimental matrix data taken from (Ehrenfreund et al. 1992) that include all the visible spectral range, and systematically assign the transitions on it.

TD–DFT predicts four electronic transitions between 400 and 500 nm, respectively at 425, 433, 478, and 491 nm (cf. Table 4.2). In the matrix spectrum published by Ehrenfreund et al. (1992), the most intense band in this interval is detected at 459 nm and matches the one we detect at 457 nm. We tentatively assign it to the $D_{10} \longleftarrow D_0$, calculated to be at 433 nm with an oscillator strength $f = 2.7 \times 10^{-2}$. The partially resolved structure on the blue side, which is visible both in our experiments and in the neon-matrix spectrum, is likely to be a vibronic sequence of the same electronic transition. The band that we detect at 432 nm would then be the $D_{11} \longleftarrow D_0$, calculated to be at 425 nm with an oscillator strength $f = 8.0 \times 10^{-3}$. We further detect another weak band at 473 nm, which is also visible in the neon-matrix spectrum in Ehrenfreund

	Experiment		TD-DFT		
Transition	PIRENEA	Previous	BP/SVP		Previous
Pyrene$^+$ ($C_{16}H_{10}^+$)					
$D_5 \longleftarrow D_0$	436	439.5[c], 436.2[d]	426(0.206)		419(0.291)[b]
$D_4 \longleftarrow D_0$		486.8[a]	508(0.012)		498(0.017)[b]
1-Methylpyrene$^+$ (CH_3-$C_{16}H_9^+$)					
			isomer (e)	isomer (f)	
$D_5 \longleftarrow D_0$	442	444.0[e], ∼441[f]		436(0.241)	
	454	456.0[e]	440(0.234)		440(0.233)[g]
$D_4 \longleftarrow D_0$	480	482.5[e]	508(0.019)	509(0.017)	507(0.019)[g]

[a] Argon matrix (Vala et al. 1994); [b] TD-DFT calculations at the BLYP/6-31G** level (Hirata et al. 1999); [c] Neon matrix (Salama & Allamandola 1992); [d] Multiplex integrated cavity output spectroscopy (Biennier 2004); [e] Neon matrix (Léger et al. 1995); [f] Cavity ring-down spectroscopy (Tan & Salama 2006); [g] TD-DFT calculations at the BP86/SVP level (Tan & Salama 2006).

Table 4.1: Positions of the bands (expressed in nm) as measured in the MPD experiments with PIRENEA for the pyrene cation ($C_{16}H_{10}{}^+$) and the 1-methylpyrene cation ($CH_3 - C_{16}H_9{}^+$). Band origins are identified through the comparison with the electronic transitions and the corresponding oscillator strengths (within parentheses) as computed using the split valence polarization (SVP) basis set in conjunction with the BP86 exchange-correlation functional. For comparison we list also previous experimental and theoretical data.

et al. (1992), even if unlisted in this paper, which would be the $D_9 \longleftarrow D_0$, calculated to be at 478 nm with an oscillator strength $f = 9.2 \times 10^{-3}$. Finally, the band detected at 502 nm in the neon-matrix spectrum would then be the $D_5 \longleftarrow D_0$, calculated to be at 491 nm with an oscillator strength $f = 7.6 \times 10^{-3}$, even if at least part of this band could be due to a coincident very strong band in benzo(g,h,i)perylene (Salama et al. 1999), which could be present as an impurity in the coronene vapour or could be formed in the matrix experiment by fragmentation of coronene.

The ground state of the coronene cation slightly breaks the D_{6h} symmetry due to the Jahn–Teller effect. This affects excited states in a different way (some states are not affected at all, depending on symmetry of the state) and is relatively subject to numerical errors, since Jahn–Teller minima are usually very shallow. Symmetry–broken states, in principle, should be properly treated by taking into account the dynamic interaction of the two splitted electronic configurations, since they are separated by a very small energy barrier.

We can estimate the expected error range of the calculations by comparing the same vertical electronic transitions, as computed by enforcing D_{6h} symmetry, with those calculated in the geometry obtained optimising the ground state (which results in D_{2h} symmetry due to Jahn–Teller distortion). The comparison between the two theoretical calculations (cf. Table 4.2), obtained with and without the D_{6h} symmetry constraint, and corresponding to very close geometries, show the sensitivity of band positions and intensities to the conformation of the molecule. This stresses the difficulty in interpreting the intensities in MPD spectra in terms of absorption intensities: since several photons are needed to achieve photodissociation, all but the first one are absorbed by a hot molecule, in which the band position and intensities may be shifted by variable amounts. This means that a band whose position is more sensitive to geometry changes will appear weaker on MPD spectra, since the absorption of the subsequent photons will be less likely. Conversely, a band relatively insensitive to small geometry changes will appear stronger.

4.3.4 Simply dehydrogenated coronene cation ($C_{24}H_{11}{}^{+}$)

The $C_{24}H_{11}{}^{+}$ spectrum (cf. Fig. 4.6) is very similar to the one measured for the coronene cation, we observe, in particular, the same broad band at ~ 458 nm with a vibronic progression on the blue side of the band. We further observe a small feature standing out at ~ 442 nm and another weak band at 478 nm. TD–DFT predicts four electronic transitions between 400 and 500 nm, respectively at 420, 432, 471, and 492 nm (cf. Table 4.2). We tentatively assign the main observed band at 458 nm to the $T_{10} \longleftarrow T_0$ transition, calculated at 432 nm with an oscillator strength $f = 2.2 \times 10^{-2}$. The feature observed at 442 nm, instead, cannot be attributed to the predicted transition at 420 nm because it is too strong compared to the calculated intensity ($f = 2.3 \times 10^{-3}$), so it probably belongs to the vibronic progression of the 458 nm band. Another

	Experiment		TD-DFT		
Transition	PIRENEA	Previous	BP/SVP		Previous
Coronene$^+$ ($C_{24}H_{12}^+$)					
			D_{2h}	D_{6h}	
$D_{12} \longleftarrow D_0$				419.8(0.007)	
$D_{11} \longleftarrow D_0$	432		425(0.008)	420.3(0.007)	
$D_{10} \longleftarrow D_0$	457	459.0[a]	433(0.030)		427(0.030)[b]
$D_9 \longleftarrow D_0$				470(0.008)	
$D_7 \longleftarrow D_0$	473		478(0.009)		
$D_6 \longleftarrow D_0$				505(0.002)	
$D_5 \longleftarrow D_0$		502[a]	491(0.008)		
Simply dehydro-coronene$^+$ ($C_{24}H_{11}^+$)					
$T_{12} \longleftarrow T_0$			420(0.002)		
$T_{10} \longleftarrow T_0$	458		432(0.022)		
$T_7 \longleftarrow T_0$			471(0.016)		
$T_6 \longleftarrow T_0$	478		492(0.006)		
Doubly dehydro-coronene$^+$ ($C_{24}H_{10}^+$)					
$D_{17} \longleftarrow D_0$	442		421(0.018)		
$D_{16} \longleftarrow D_0$	458		433(0.033)		
$D_{11} \longleftarrow D_0$			475(0.019)		
$D_9 \longleftarrow D_0$			485(0.009)		

[a] Neon matrix (Ehrenfreund et al. 1992); [b] TD-DFT calculations at the BLYP/6-31G* level (Weisman et al. 2003).

Table 4.2: Positions of the bands (expressed in nm) as measured in the PIRENEA experiment in the wavelength range 430 - 480 nm for the coronene cation ($C_{24}H_{12}{}^+$) and two of its dehydrogenated derivatives ($C_{24}H_{11}{}^+$ and $C_{24}H_{10}{}^+$). Electronic transitions and the corresponding oscillator strengths (within parentheses) are computed using the split valence polarization (SVP) basis set in conjunction with the BP86 exchange-correlation functional. Previous experimental and theoretical data are reported, for comparison, in the case of coronene cation.

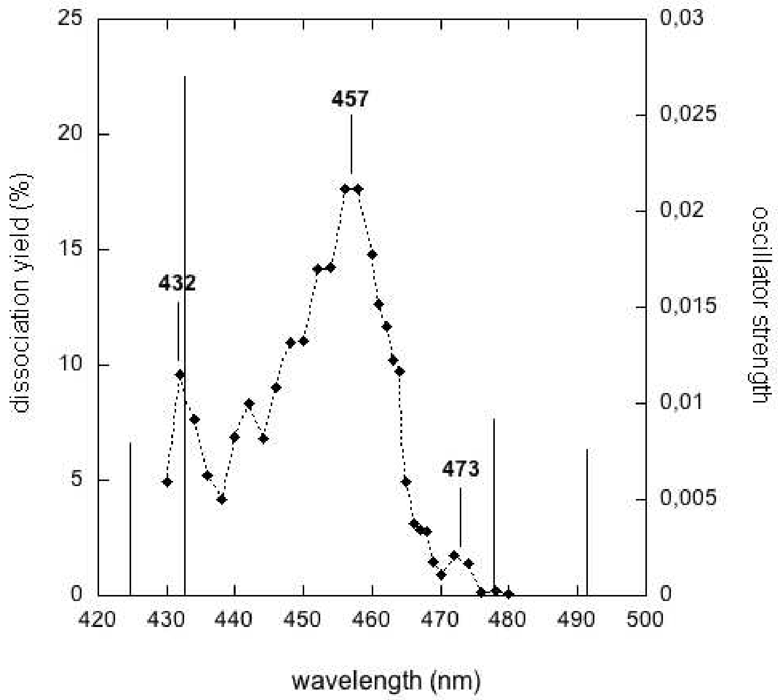

Figure 4.5: MPD spectrum of the coronene cation measured with the PIRENEA set-up. Only the electronic transitions calculated with D_{2h} symmetry are shown.

transition is predicted by calculations at $\sim$ 471 nm with an oscillator strength $f = 1.6 \times 10^{-2}$. In our spectrum we cannot identify any other feature next to this position, however, considering the broadening that affects our spectra, this transition could be blended with the broad structure of the 458 nm band. More precise spectroscopic techniques should improve the identification. Finally, the weak band detected at 478 nm could likely be the $T_6 \longleftarrow T_0$ transition, calculated to be at 492 nm with an oscillator strength $f = 5.7 \times 10^{-3}$.

4.3.5 Doubly dehydrogenated coronene cation ($C_{24}H_{10}{}^{+}$)

$C_{24}H_{10}{}^{+}$ (see (d) in Fig. 4.2) can, in principle, have six nonequivalent isomers corresponding to different distances between the photoejected H atoms, which cannot be distinguished *a priori* in our setup. Previous photodissociation experiments performed on the coronene cation in PIRENEA, provide however strong evidence that only isomer with adjacent H atoms missing have to be considered (Joblin et al. 2009). This is further confirmed by calculations on the binding

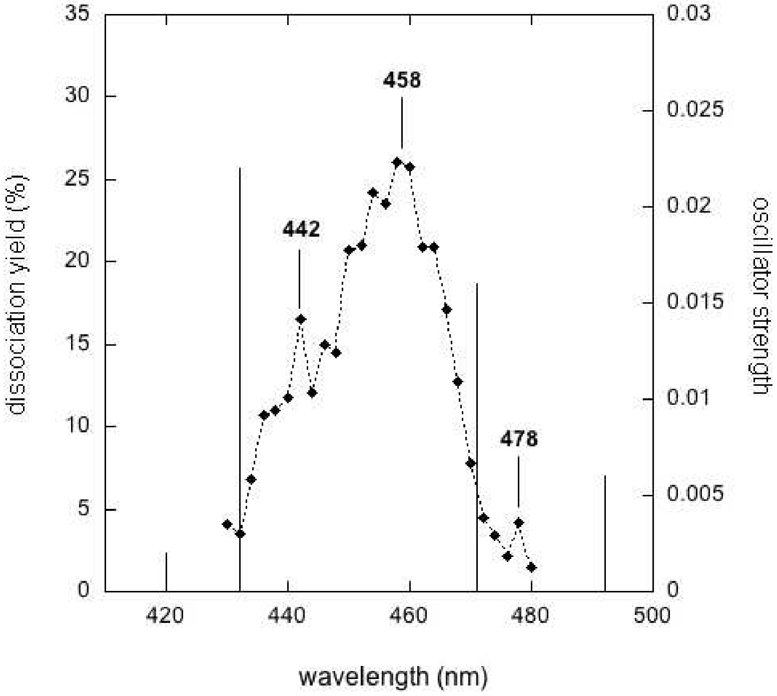

Figure 4.6: MPD spectrum of the simply-dehydrogenated coronene cation measured with the PIRENEA set-up.

energies of the isomers which show that this isomer is, by far, the most stable one (about 1.2 eV lower in energy). MPD of this species is performed with one laser pulse at 12 mJ. In the $C_{24}H_{10}{}^+$ spectrum (cf. Fig. 4.7) two closely spaced electronic transitions stand out, at $\sim$ 442 and 458 nm. We observe also what could be interpreted as a vibronic progression on the red side of the 458 nm band.

The presence of these hot bands, as discussed in the case of pyrene cation, is not unexpected, as the ion cloud may retain some residual excitation energy due to the photofragmentation of the parent and to the procedure of ejection of other species.
The strongest calculated transition in this spectral range is predicted to be the $D_{16} \longleftarrow D_0$ at 433 nm, with $f = 3.3 \times 10^{-2}$ (cf. Table 4.2). This transition is therefore the most likely assignment for the strongest peak we observe at 458 nm. The band we observe at 442 nm can then be associated to the $D_{17} \longleftarrow D_0$ transition predicted to be at 421 nm with $f = 1.8 \times 10^{-2}$ (see Table 4.2). The other two transitions predicted by calculations at respectively 475 and 485 nm are probably blended with the observed vibronic progression.

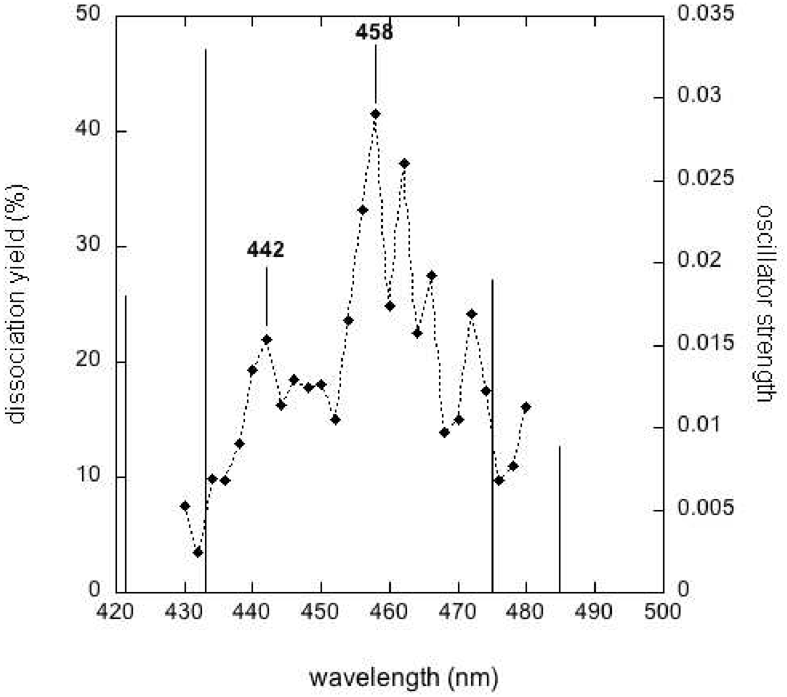

Figure 4.7: MPD spectrum of doubly-dehydrogenated coronene cation measured with the PIRENEA set-up.

4.3.6 Completely dehydrogenated coronene cation (C_{24}^{+})

C_{24}^{+} was produced by UV-photofragmentation of the parent ion with the Xe arc lamp. MPD of this species was performed with ten laser pulses and without keeping constant the laser energy. We can distinguish in the measured spectrum two main features standing out at about 439 and 444 nm, and a series of smaller peaks between 450 and 480 nm.

Previous experiments performed on the photodissociation of the coronene cation in PIRENEA, evidenced the presence of two different fragmentation paths, which suggests that different isomeric forms of C_{24}^{+} could be simultaneously produced in the dissociation process (Joblin 2003). Jones et al. (Jones & Seifert 1999) have calculated energies and structures of various isomeric forms of C_{24}, in particular they have found 12 different stable isomers for this species (cf. Fig. 4.10).

The results of these studies show that fullerene or graphitic-type structures are the lowest energy structures, however neither fullerene-like nor graphite-like isomers have been experimentally

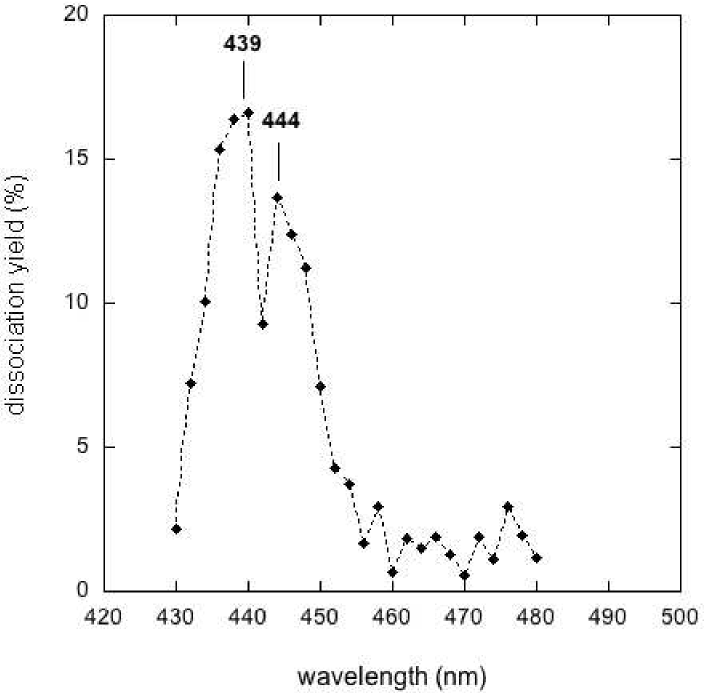

Figure 4.8: MPD spectrum of completely dehydrogenated coronene cation measured with the PIRENEA set-up.

observed so far for C_{24}^{+} (von Helden et al. 1993; Shelimov et al. 1994). Experimental measurements, in fact, seem rather to give evidence for the presence of bicyclic rings in the gas phase. To identify the bands observed in our measurements we computed the electronic transitions of C_{24}^{+} relative to all the twelve structures predicted by Jones and we compared them to our spectrum. The results of our calculations are listed in Table 4.3.

Calculated electronic transitions with oscillator strengths $f \leq 0.001$ are not reported (for instance the cage isomer 2 has no transitions with $f \geq 0.001$ in the considered spectral range). Values relative to the ring form (isomer 6) are not reported as well because calculations do not predict any transition in the spectral range considered in our experiment.

Comparing the experimental spectrum to calculations, the planar isomer seems to be a plausible candidate for identification of the structure detected in our experiment, having two close bands at respectively 446 and 451 nm (for both bands $\Delta\lambda$ = 7 nm with respect to our measured positions) with similar oscillator strenghts. Other possible candidates are the two-rings isomers 9, 10 and 11 (cf. Fig. 4.9), which also have transitions that are close (within the precision of the calculations) to the experimental measurements in the considered spectral window. Inter-

estingly, the oscillator strengths obtained for the electronic transitions of isomers 10 and 11 are almost two orders of magnitudes larger than those found for the planar form in the same region. As we do not know the absolute intensity of the measured bands a definite identification based only on this comparison is not possible. Furthermore, the simultaneous presence of more than one isomer cannot be excluded. Considering their close positions, some of the electronic transitions could be merged resulting in only two distinct peaks in our spectrum.
Comparing the spectrum of C_{24}^{+} to those recorded for the other dehydrogenated coronene derivatives, we can also observe the effect of progressive dehydrogenation of the parent cation, which results in a blue shift of the main electronic transitions (cf. Malloci et al. (2008)).

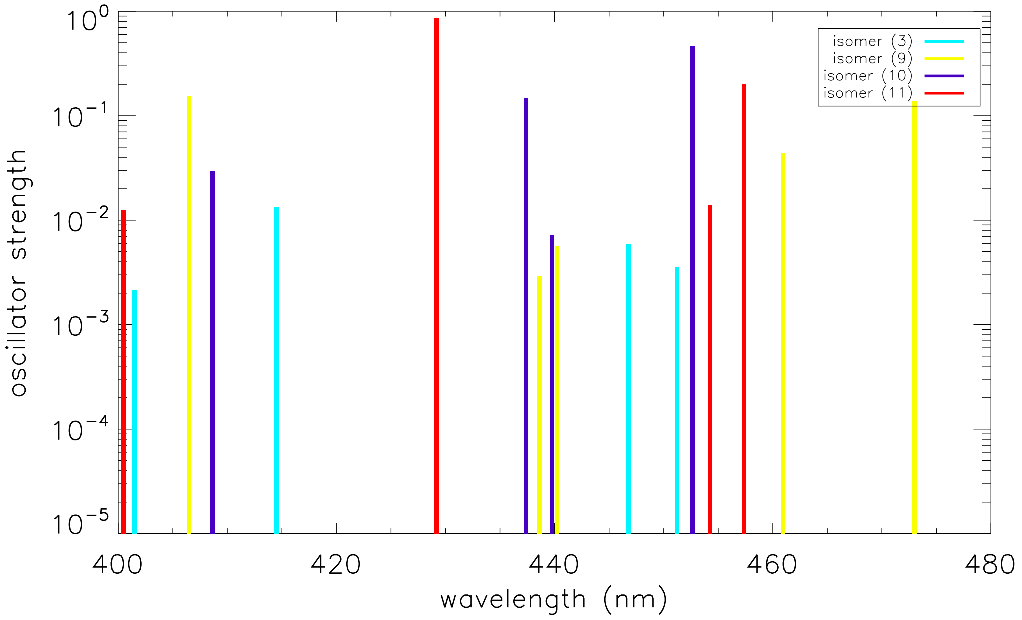

Figure 4.9: Calculated electronic transitions, with corresponding oscillator strengths, of four different isomers of $C_{24}{}^{+}$, whose geometry is represented in Fig. 4.10, which seem to be plausible structures produced in our experiment.

PIRENEA		Cage (1)*		Cage (2)*		Planar (3)*	
λ (nm)		λ (nm)	*f*	λ (nm)	*f*	λ (nm)	*f*
439		407.4	0.002			401.5	0.002
444		408.8	0.001			414.5	0.010
		439.6	0.001			446.8	0.006
		483.9	0.003			451.2	0.004

Graphitic (4)*		Cage (5)*		Double rings (7)*		Double rings (8)*	
λ (nm)	*f*	λ (nm)	*f*	λ (nm)	*f*	λ (nm)	*f*
416.2	0.004	435.8	0.001	401.9	0.046	415.9	0.109
418.4	0.002	486.5	0.002	402.4	0.009		
421.1	0.002	497.7	0.004	404.1	0.003		
422.4	0.002			408.9	0.046		
426.9	0.002			413.4	0.016		
465.8	0.002			422.1	0.054		
469.8	0.009			458.3	0.001		
				473.0	0.192		
				498.9	0.019		

Double rings (9)*		Double rings (10)*		Double rings (11)*		Linear (12)*	
λ (nm)	*f*	λ (nm)	*f*	λ (nm)	*f*	λ (nm)	*f*
406.5	0.155	408.6	0.029	400.5	0.012	492.5	1.526
438.6	0.003	437.4	0.148	429.2	0.866	497.5	0.658
440.2	0.006	439.8	0.007	454.2	0.014		
460.9	0.044	452.6	0.467	457.3	0.202		
472.9	0.139						

* cf. Fig. 4.10

Table 4.3: Calculated electronic transitions and corresponding oscillator strengths for ten different isomers of the $C_{24}{}^+$ cation compared to the spectral features measured in the PIRENEA experiment. All the calculations are made using the split valence polarization (SVP) basis set in conjunction with the BP86 exchange-correlation functional.

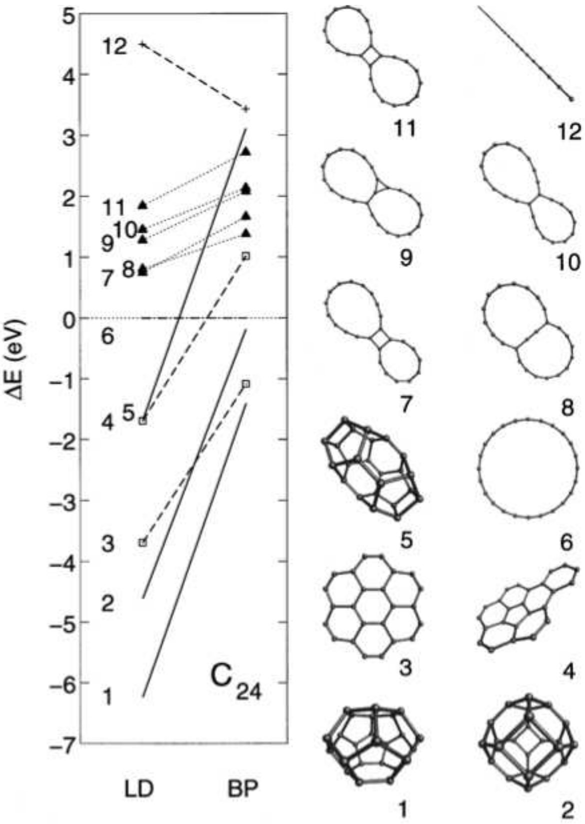

Figure 4.10: Structures and energies of the isomers of C_{24} (Figure taken from Jones & Seifert (1999)).

4.4 Modelling the photophysics of PAH cations

The dissociation yield that is measured in our experiments depends on the absorption cross-section, σ_{abs}, of the studied species and on the local intensity of the radiation field over the ion cloud. In order to retrieve the value of σ_{abs} it is necessary to interpret the experimental data using a model that describes the photophysics of the ions. To achieve this goal we have used a kinetic Monte Carlo code (Rapacioli et al. 2006; Joblin et al. 2002) that provides a description of the photoabsorption and dissociation processes and the time evolution of the internal energy of the considered species as a function of the flux density of photons. The method has been initially described by Boissel et al. (1997).

In our experimental conditions, involving low values of the laser fluence, multiphoton events are negligible. However during a laser pulse (t_{pulse} = 5 ns), the ion has enough time to absorb sequential photons leading to an increase of its internal energy. If this energy is above the dissociation threshold the ion may fragment. The absorption rate constant, k_{abs}, can be expressed by the following equation

$$k_{abs} = \frac{\sigma_{abs}}{S}\phi = \frac{\sigma_{abs}}{S}\frac{\lambda}{hc}\frac{E_{laser}}{t_{pulse}} \tag{4.1}$$

where σ_{abs} is the absorption cross-section of the electronic state of the molecule averaged over the spectral profile of the laser, S the laser spot surface, ϕ is the photon flux (number of photons per unit time), λ is the wavelength of the excitation photon and E_{laser} and t_{laser} are respectively the laser pulse energy and the pulse duration. According to Boissel et al. (1997) the fragmentation rate k_d as a function of the internal energy U, is given by

$$k_d(U) = A_d\frac{\rho(U - E_d)}{\rho(U)} \tag{4.2}$$

where ρ is the density of states of the parent ion, E_d is the binding energy which is taken to be 4.8 eV for the loss of an H atom (Pino et al. 2007; Jolibois et al. 2005) and A_d is a preexponential factor. The density of states is calculated using the list of modes determined by DFT for the parent ion and applying the Beyer-Swinehart algorithm (Stein & Rabinovitch 1973). The value of A_d was calculated using the results of Jochims et al. (1994): $k_d = 10^4\ s^{-1}$ at U = 9.06 and 12.05 eV for $C_{16}H_{10}{}^+$ and $C_{24}H_{12}{}^+$ respectively.

We have observed that the experimental conditions strongly influence the measurement of the dissociation yield. Two additional parameters, in particular, have to be considered when modelling the data: the overlap between the laser spot and the ion cloud, which can change due to possible variations of the ion cloud size, shape and position, and the photon local density in the laser spot, which in turn depends on the laser beam profile.

The ion cloud spatial distribution and position inside the cell depend on the details of ion formation and injection into the trap, which can to some extent vary from shot to shot. This affects the overlap between the laser spot and the ion cloud, and consequently the measured dissociation yield of the species. This is taken into account in our measurements by averaging, at each wavelength, the recorded dissociation yield over several spectra.

The second effect we have to consider is the variation of the local photon flux (number of photons per unit time per unit surface) in the laser spot. This parameter plays an important role on dissociation, especially in the case of molecules that need to absorb a large number of photons to dissociate (e.g. coronene cation). The OPO beam intensity follows a gaussian profile over an elliptical surface with semi-axis of respectively 3 and 2.55 mm (values obtained from the FWHM of the x and y beam profiles, cf. Fig. 4.11). The beam profile gives us the spatial distribution of the laser intensity over the laser spot surface from which we can determine the spatial distribution of the photon flux in the laser spot.

Using the Monte Carlo model, we were able to derive the number of photons absorbed per pulse and the corresponding dissociation counts for different values of the absorption cross-section (see Figs. 4.14 and 4.13). As can be seen, the dissociation is dominated, in the case of

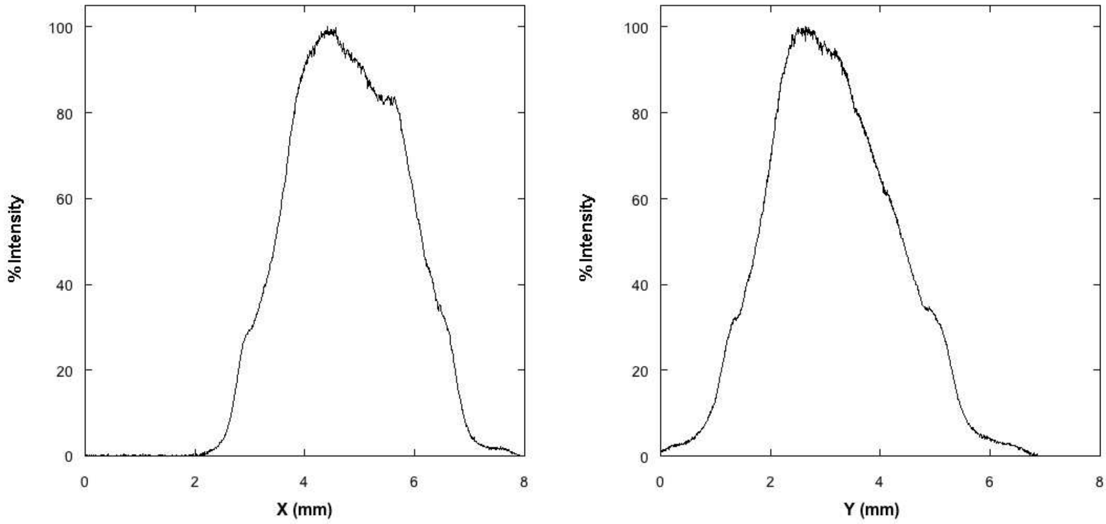

Figure 4.11: Intensity mean profiles (averaged over 50 laser shots) of the Panther EX OPO laser beam along the x and y directions measured with a LaserCam-HR beam profiler (*C*oherent) at 1 m from the laser.

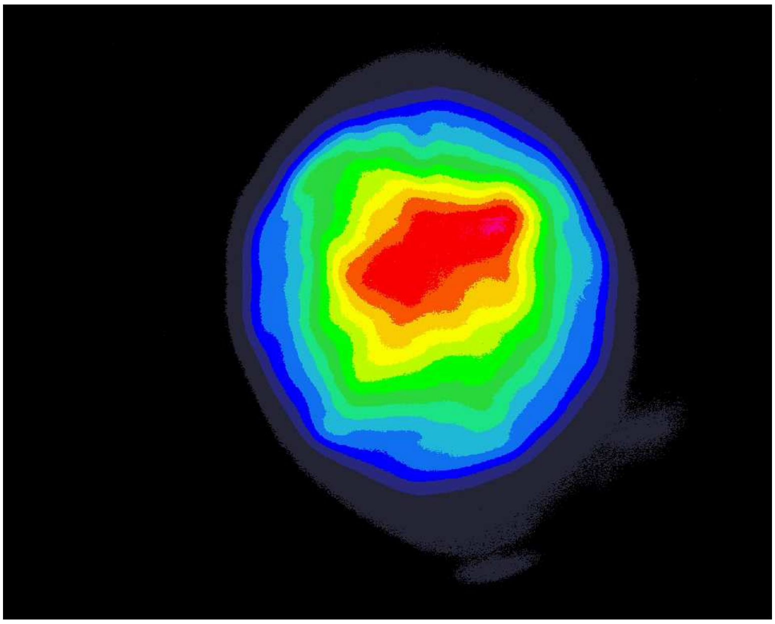

Figure 4.12: Image of the OPO laser beam mean profile (averaged over 50 laser shots) in the x-y plane. The different colours corresponds to decreasing laser intensities going from the centre of the spot to the edges.

the pyrene cation, by the ions that have absorbed at least three photons of 2.84 eV (λ = 436 nm) while for the coronene cation, the absorption of four photons of 2.71 eV (λ = 457 nm) is required to efficiently dissociate.

Studies on the photofragmentation of the fluorene cation using sequential multiphoton absorption have shown that the absorption cross-section may vary with the number of absorbed photons (Nguyen-Thi et al. 2006b,a). We have considered this hypothesis in our calculations running simulations for the pyrene cation with a variable cross-section but we could not evidence such an effect from our measurements.

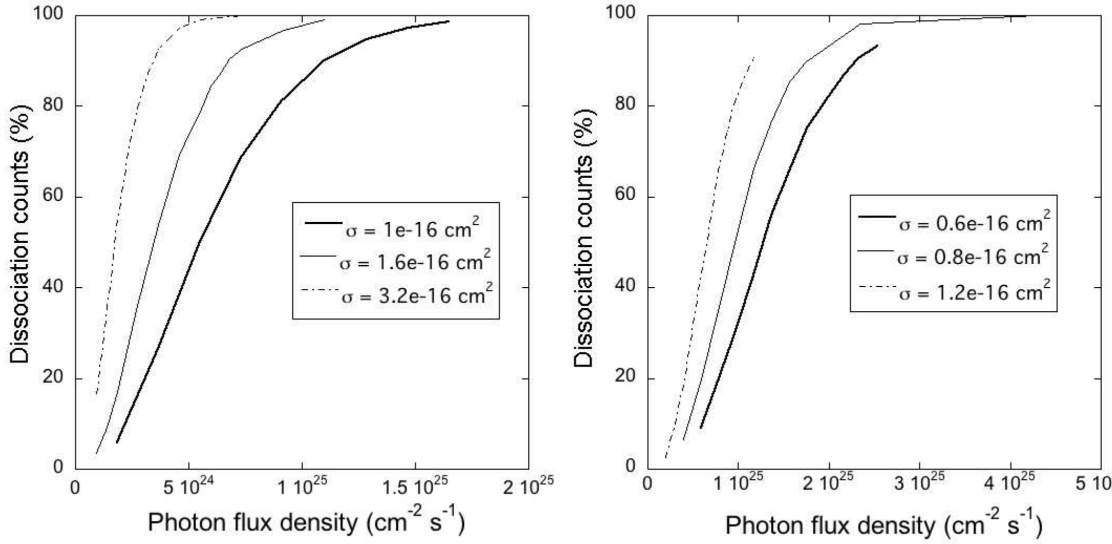

Figure 4.13: Relative dissociation counts as a function of the photon flux density obtained from the model considering different values for the absorption cross-sections, for pyrene cation (left panel) and coronene cation (right panel).

To derive the absorption cross-section from the fit of the experimental data with our model, we have measured the dissociation yield as a function of the laser energy. We observed an increase of this yield with the energy up to a saturation value that is on average 50% and 60% for $C_{16}H_{10}{}^+$ and $C_{24}H_{12}{}^+$ respectively, and up to 80% when considering individual shots (cf. Tab. 4.4). An important aspect that arise from these measurements is that while in the case of the pyrene cation the mean and maximum values of the dissociation yield are always very similar, meaning that the ions are efficiently dissociated at each laser shot. This is not the case for the coronene cation for which dissociation can noticeably vary from one shot to another. This effect is related to the variation of the local photon flux in the laser beam, discussed above, to which bigger molecules are more sensitive. We can further infer from these data that the size of the ion cloud is of the same order as the laser beam.

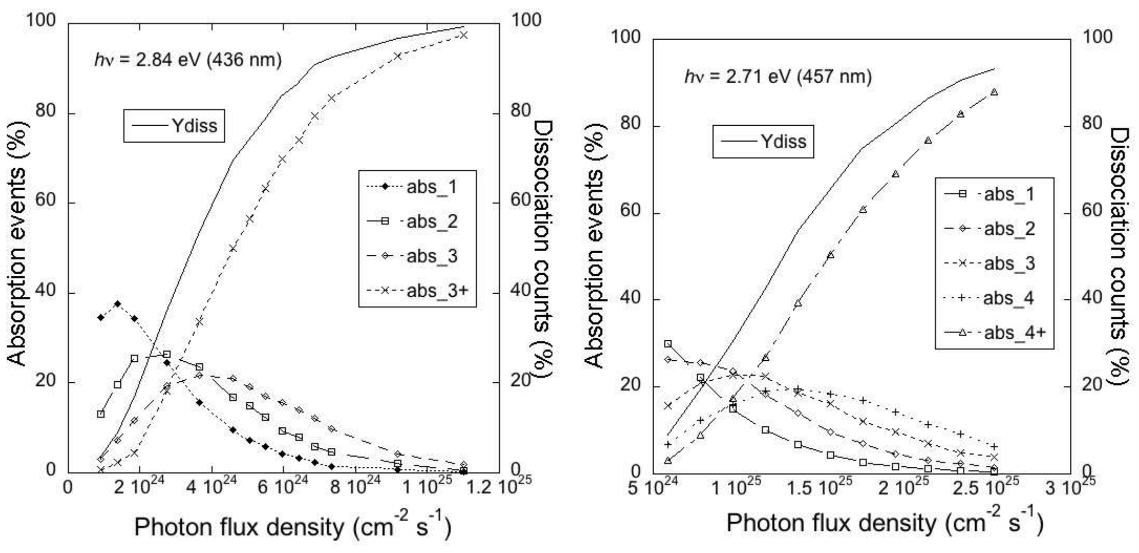

Figure 4.14: Photoabsorption events (abs_n is the fraction of events with n absorbed photons, abs_n+ with more than n photons) and total dissociation yield (Ydiss) calculated with the model as a function of the photon flux density. The left panel shows the results obtained for the pyrene cation for $\sigma_{abs} = 1.6 \times 10^{-16} cm^2$ while the right panel shows the results obtained for the coronene cation for $\sigma_{abs} = 0.6 \times 10^{-16} cm^2$.

The calculated dissociation yield is obtained combining the results of the Monte Carlo simulations (Fig. 4.13) and the spatial information on the photon flux density derived from measurements of the laser beam profile. Relative dissociation yields were used to obtain values that are independent of the ion cloud size. The fitting of the experimental data allows then to constrain the absorption cross-section of the studied species. We derived a value of 1.6×10^{-16}cm^2 for the pyrene cation at λ = 436 nm and of 0.6×10^{-16}cm^2 for the coronene cation at λ = 457 nm (cf. Fig. 4.15).

The value obtained for the pyrene cation results to be the same estimated by Biennier (2004). In the case of the coronene cation our data represent the first estimation of its cross-section coming from gas-phase experimental measurements. An absorption cross-section $\sigma_{abs} \simeq 0.9 \times 10^{-16}$cm^2 for the 459 nm band can be derived from the matrix data of Ehrenfreund et al. (1992). This value is very close to our result. All these results justify *a posteriori* that our physical description, in which we consider only sequential absorption of photons and neglect true multi-photon events, is correct.

Energy OPO (mJ)	Max Diss Yield (%)	Mean Diss Yield (%)
Pyrene$^+$ [$C_{16}H_{10}^+$] at λ = 436 nm		
4	20.6	19.4
8	39.5	34.5
12	47.9	43.5
16	48.6	46.2
20	55.6	51.2
Coronene$^+$ [$C_{24}H_{12}^+$] at λ = 457 nm		
10	48.2	28.7
12	64.9	38.2
14	85.7	42.6
16	81.0	52.3
20	88.3	62.0

Table 4.4: Measurements of the dissociation yield of coronene and pyrene cations as a function of the OPO laser energy. For a given energy the mean and maximum values of the dissociation yield are calculated over a series of 20 dissociation spectra.

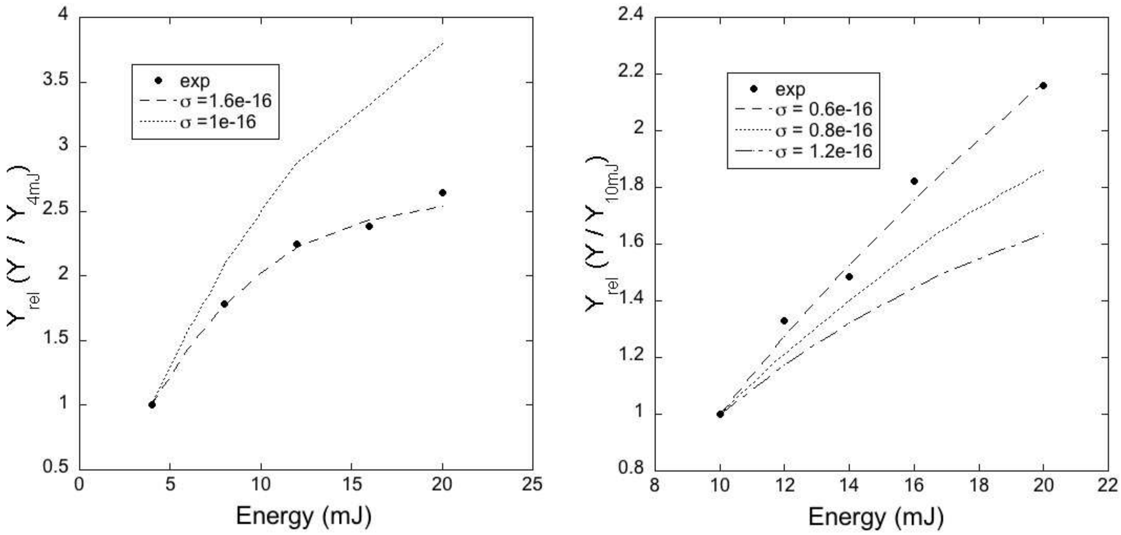

Figure 4.15: Relative dissociation yields measured experimentally (dots) and normalised to the lowest value, compared with the results obtained from the model considering different values for the absorption cross-sections (lines), for pyrene cation (left panel) and coronene cation (right panel).

4.5 General remarks and astrophysical implications

The ion-trap technique used here offers a relatively straightforward way to produce, isolate and study species, which is difficult to achieve with other techniques. The drawback of the technique is that the multiple photon absorption process raises considerably the internal energy of the probed molecular ions so even if the species are cold before the beginning of the MPD scan, they are hot after absorbing the first of the series of photons needed to dissociate them. In these hot molecules band positions and intensities may differ from those of the cold ions, making more difficult the analysis of the resulting MPD spectrum. Furthermore, possible excitation of the ground state levels through fast energy redistribution must be taken into account (cf. sect. 4.3.1).

Despite these difficulties the results obtained here have shown a good agreement with previous experimental data, when available, and have provided a first understanding of the electronic structure of species never studied before. Theoretical calculations helped us to identify the measured bands and represent, in some cases, an essential tool for the interpretation of the experimental spectra, as shown in the case of 1–methylpyrene cation (cf. sect. 4.3.2) and of C_{24}^{+} (cf. sect. 4.8).

From an astrophysical point of view, our spectra are not directly comparable to observational data for the reasons explained above, however they give us the possibility to outline which species are suitable candidates as carriers of the DIBs. Among the species studied here, only three of them exhibit spectral features at a position close to the 4428 Å DIB: the 1–methylpyrene cation ($\lambda_{PIRENEA}$ = 442 nm), the doubly dehydrogenated coronene cation ($\lambda_{PIRENEA}$ = 442 nm) and the completely dehydrogenated coronene cation ($\lambda_{PIRENEA}$ = 444 nm). For the first of them, $CH_3 - C_{16}H_9{}^{+}$, measurements made on cold gas-phase ions by Tan & Salama (2006) have already shown that the characteristics of the observed band are not correlated with those of the 4428 Å DIB. Still, an interesting result we have obtained with our measurements is the identification of the simultaneous presence of two different structures for this species. This aspect could not be evidenced in matrix experiments in which the contribution of another species (the 1–methylene–pyrene cation) was invoked to interpret the spectrum.

In the case of the doubly dehydrogenated coronene cation, two electronic transitions are present in the considered spectral range, at 442 and 458 nm, the second one being much stronger. This automatically excludes this species as a possible carrier for the 4428 Å DIB.

Concerning $C_{24}{}^{+}$, proposed to be a possible DIB carrier by Duley (2006), our gas-phase spectrum was found to have two main bands at 439 and 444 nm. Because of the small spectral window sampled in our experiment, we are not able to conclude if both these bands belong to a same species or if they have to be attributed to different isomers. The first scenario would exclude C_{24}^{+} as a possible carrier for the 4428 Å band. In the case of the simultaneous presence of different isomers (a combination of bicyclic rings 9, 10 and 11, cf. section 4.8), instead, we could propose that one of them absorbs only at 444 nm and not at 439 nm. In particular, among the considered species, isomer 11 presents a strong isolated band close to the 4428 Å DIB position. This second scenario is however questionnable. If $C_{24}{}^+$ species coming from the dehydrogenation of $C_mH_n{}^+$ PAHs (with $m \geq 24$) can survive in the interstellar medium, as suggested by Le Page et al. (2003), different isomeric forms are expected to exist and different bands should be simultaneously present. A natural way to produce $C_{24}{}^+$ is by dehydrogenation of coronene, which is expected to be a prototype of medium-sized interstellar PAHs. We have seen that the spectrum of $C_{24}{}^+$ produced in these conditions already leads to two distinct bands that are not observed in the ISM.

Chapter 5

Summary and perspectives

Mihi cura futuri.
My concern is the future.

The PIRENEA set-up has been used in this work to study the properties of polycyclic aromatic hydrocarbons (PAHs), a class of large molecules proposed to account for the AIBs, a set of discrete emission bands dominating the mid-infrared spectra of many galactic and extragalactic objects. Two different questions have been approached: (i) investigate the photodissociation of PAHs under UV photon irradiation in astrophysically relevant conditions, (ii) characterise the visible spectroscopic properties of several PAH cations and dehydrogenated derivatives.
The main results obtained are summarised in the following section.

5.1 Summary of the results

5.1.1 Photofragmentation of isolated PAH ions

The photofragmentation of four different medium-sized PAH cations has been performed with the continuous irradiation of a Xe arc lamp. The main fragmentation pathways of each species have been identified showing that:

- The loss of a single hydrogen atom is the primary fragmentation channel for all the studied species.

- Completely dehydrogenation of the parent ion was observed only for the naphtho[2,3-a]pyrene species while all the other examined cations showed only partial dehydrogenation ending up with the production of ${C_nH_4}^+$ species.

- Elimination of an acetylene molecule was observed for all the studied species. Other fragmentation pathways involving the loss of a diacetylene molecule and small hydrocarbons (C_nH_m, with n = 1, 2) were also observed respectively in the case of the pyrene and pentacene cations.

- All the examined species exhibited, in their dissociation cascade, the presence of several carbon clusters. Dissociation paths involving the loss of C, C_2 and C_3 neutral carbon fragments were evidenced for these species.

These results put forward the possible contribution of PAHs to the formation of small hydrocarbons and carbon clusters in the interstellar medium as already suggested from observations of PDRs.

5.1.2 Visible photodissociation spectroscopy of $PAHs^+$

The MPD technique used in this work enabled us to indirectly study the visible absorption spectrum of non volatile reactive ions isolated in a cold ICR cell. Since all species with a different m/z ratio are ejected before recording the spectrum, the technique is free from contaminants (with the exception of isomers) that are difficult to avoid by other methods. The technique has the limitation of recording an action spectrum that does not provide direct information on the cross-section. For this reason theoretical calculations and modelling have been used to complement it, in particular a kinetic Monte Carlo code has been used, for two of the studied species, to constrain the photophysics of these ions and to derive their absorption cross-section. The obtained results can be summarised as follows:

- Comparison with gas-phase spectra of cold PAHs has shown a very good agreement with the measured band positions in the case of pyrene and 1–methylpyrene cations, confirming the validity of our experimental method in obtaining the band positions in the gas-phase. Still the technique does not allow to measure the band profile of cold ions.

- The gas-phase spectra of the coronene cation, ${C_{24}H_{12}}^+$, and some of its dehydrogenated derivatives (${C_{24}H_p}^+$ with p = 0, 10, 11), have been measured and discussed here for the first time. The progressive dehydrogenation is shown to induce a blue shift in the band positions as predicted by theory.

- Different isomeric forms were considered in the case of C_{24}^+ species. By comparison with theoretical calculations different isomers were identified as possible structures produced in our experiment.

- Absorption cross-sections were derived for the pyrene and coronene cations. The obtained values seem to be in satisfactory agreement with previous experimental results.

Our results have shown that none of the species studied here can be retained as a possible carrier for the 4428 Å DIB.

5.2 Perspectives

The photodissociation study performed here offers a qualitative analysis of the behaviour of PAHs exposed to continuous UV-visible radiation. More work should however be performed to obtain molecular data that can be used in astrophysical models, for instance time-resolved experiments could be used to measure photo-dissociation kinetics and the dissociation constants. The determination of branching ratios should also be considered. This study cannot be accomplished with the use of the Xe lamp because under continuous irradiation all the species, parent ions and fragments, simultaneously absorb photons and fragment preventing from measurements of the branching ratios. The use of a source of FUV photons (10.5 eV), currently under installation on PIRENEA, in future experiments could help in this analysis.

Concerning the study of the spectroscopic properties of PAH cations in the gas-phase, both laboratory experiments and calculations are challenging as shown by the lack, still today, of accurate quantitative data on the photo-absorption properties of a large number of PAH ions and derivative species. Even if the technique presented here does not provide spectra which are directly comparable to the astronomical ones, these data are useful for the pre-selection of the most promising interstellar candidates for the DIBs.

Perspectives for this work will include: (i) the extension of the spectral window of investigation to a larger spectral range; (ii) the recording of spectra of other species which are relevant according to astrophysical models, and the estimation of the corresponding absorption cross-sections; (iii) from an experimental point of view a better control of the ion temperature in the trap; (iv) from a theoretical point of view the modelling of the vibrational dynamics of hot ions to more accurately reconstruct the absorption spectrum from the MPD measurements.

Conclusions [en]

An original set-up dedicated to astrochemistry, PIRENEA (Piège à Ions pour la Recherche et l'Etude de Nouvelles Espèces Astrochimiques), has been used in this work to study the properties of polycyclic aromatic hydrocarbons (PAHs), a class of large molecules that has been proposed to be abundant in the ISM.

In this study, we have first investigated the photodissociation of different medium-sized PAHs under UV photon irradiation, which is the main process responsible for the destruction of these species in the interstellar medium. We have identified the main fragmentation paths and obtained the photofragmentation cascade of the studied species. These experimental results fit into a scenario in which PAHs could contribute to the formation of small hydrocarbons and carbon clusters in the interstellar medium as has been already suggested from observations of photodissociation regions.

As the only direct diagnostics for the presence of particular species in the ISM are their spectral fingerprints, we have also characterised the visible spectroscopic properties of several PAH cations and dehydrogenated derivatives using a laser multiphoton dissociation technique. Our results have provided first information on the electronic spectra of species never studied before. Furthermore we have shown how, with the help of a model that describes the photophysics of these ions, we can derive their absorption cross-section.

The identification of specific PAHs in space is, probably, still a long way. However new generations of laboratory experiments are in progress and upcoming data with space missions, in particular the Herschel Space Observatory, will soon offer concrete opportunities for a better understanding of the nature of these species and their formation mechanisms.

Conclusions [fr]

PIRENEA (Piège à Ions pour la Recherche et l'Etude de Nouvelles Espèces Astrochimiques), qui est un dispositif expérimental dédié à l'étude de la physico-chimie interstellaire, a été utilisé dans ce travail pour effectuer une étude expérimentale sur les molécules polycycliques aromatiques hydrogénées (PAH), une classe de macromolécules reconnue comme une composante très importante de la matière interstellaire.

Au cours de ce travail, nous avons tout d'abord étudié la photodissociation de différentes espèces PAH de taille moyenne irradiées par des photons UV, processus qui est principalement responsable de la destruction de ces molécules dans le milieu interstellaire. Pour chaque espèce étudiée, nous avons déterminé la cascade des fragments produits et identifié les principales voies de fragmentation. Ces résultats expérimentaux s'intègrent dans un scénario, déjà suggéré par les observations des régions de photodissociation du milieu interstellaire, selon lequel les PAH peuvent contribuer à la formation de petits hydrocarbures et agrégats carbonés dans ces milieux. Les signatures spectrales représentent le seul moyen direct pour pouvoir diagnostiquer la présence d'une espèce donnée dans le milieu interstellaire. Nous avons donc caractérisé les propriétés spectroscopiques de différents PAH et de leurs dérivés déshydrogénés dans le domaine visible en utilisant une technique de dissociation multiphotonique par laser. Nos résultats ont fourni les premières données spectroscopiques sur des espèces jamais étudiées auparavant. Nous avons aussi montré, en utilisant un modèle décrivant la photophysique de ces ions, qu'il est possible par l'analyse de ces mesures de déterminer la section efficace d'absorption de ces ions.

L'identification de PAH spécifiques dans l'espace nécessite, probablement, encore du temps pour aboutir. Néanmoins une nouvelle génération d'expériences de laboratoire, qui est en train d'être mise en place, ainsi que les prochaines données provenant des missions spatiales, comme l'Observatoire Spatial Herschel, vont bientôt offrir de nouvelles opportunités pour caractériser la nature de ces espèces et les mécanismes qui sont à la base de leur formation.

Bibliography

Ahlrichs, R., Bär, M., Häser, M., Horn, H., & Kölmel, C. 1989, Chem. Phys. Lett., 162, 165

Allain, T., Leach, S., & Sedlmayr, E. 1996, *A&A*, 305, 602

Allamandola, L. J., Tielens, A. G. G. M., & Barker, J. R. 1985, *ApJ Letters*, 290, L25

Amster, I. J. 1996, J. Mass Spectrom., 31, 1325

Andriesse, C. D. 1978, *A&A*, 66, 169

Asamoto, B. 1991, Analytical Applications of FT-ICR Mass Spectrometry (VCH, New York)

Baer, T., Willet, G. D., Smith, D., & Phillips, J. S. 1979, J. Chem. Phys., 70, 4076

Bakes, E. L. O. & Tielens, A. G. G. M. 1994, *ApJ*, 427, 822

Bakes, E. L. O., Tielens, A. G. G. M., & Bauschlicher, Jr., C. W. 2001a, *ApJ*, 556, 501

Bakes, E. L. O., Tielens, A. G. G. M., Bauschlicher, Jr., C. W., Hudgins, D. M., & Allamandola, L. J. 2001b, *ApJ*, 560, 261

Banisaukas, J., Szczepanski, J., Eyler, J., & Val, M. 2004, J. Phys. Chem. A, 108, 3723

Bauernschmitt, R. & Ahlrichs, R. 1996, Chem. Phys. Lett., 256, 454

Becke, A. D. 1988, Phys. Rev. A, 38, 3098

Bernard, J. P., Boulanger, F., Desert, F. X., & Puget, J. L. 1992, *A&A*, 263, 258

Berné, O., Joblin, C., Deville, Y., et al. 2007, *A&A*, 469, 575

Bernstein, M. P., Sandford, S. A., & Allamandola, L. J. 1996, *ApJ Letters*, 472, L127

Betts, N. B., Stepanovic, M., Snow, T. P., & Bierbaum, V. M. 2006, *ApJ Letters*, 651, L129

Biennier, L. 2004, Chem. Phys. Lett., 387, 287

Biennier, L., Salama, F., Allamandola, L. J., & Scherer, J. J. 2003, J. Chem. Phys., 118, 7863

Bogdanov, B. & Smith, R. D. 2005, Mass Spectrom. Rev., 24, 168

Boissel, P., de Parseval, P., Marty, P., & Lefèvre, G. 1997, J. Chem. Phys., 106, 4973

Boissel, P., Lefevre, G., & Thiébot, P. 1993, in Molecules and grains in space, ed. I. Nenner, American Institute of Physics Press: New York, 667

Bosci, R., Clar, E., & Schmidt, W. 1974, J. Chem. Phys., 60, 4406

Boudin, N., Pino, T., & Bréchignac, P. 2001, Journal of Molecular Structure, 563-564, 209

Boulanger, F., Falgarone, E., Puget, J. L., & Helou, G. 1990, *ApJ*, 364, 136

Bréchignac, P. & Pino, T. 1999, *A&A*, 343, L49

Bréchignac, P., Pino, T., & Boudin, N. 2001, Spectrochimica Acta, 57, 745

Brenner, J. & Barker, J. R. 1992, *ApJ Letters*, 388, L39

Bruneleau, N. 2007, PhD thesis, Université Toulouse III - Paul Sabatier

Casida, M. E. 1995, Recent Advances in Density Functional Theory Vol. I (D. P. Chong (Ed.), Singapore: World Scientific)

Cernicharo, J., Heras, A. M., Tielens, A. G. G. M., et al. 2001, *ApJ Letters*, 546, L123

Cherchneff, I., Barker, J. R., & Tielens, A. G. G. M. 1992, *ApJ*, 401, 269

Cook, D. J., Schlemmer, S., Balucani, N., et al. 1998, J. Phys. Chem. A, 102, 1465

Crawford, M. K., Tielens, A. G. G. M., & Allamandola, L. J. 1985, *ApJ Letters*, 293, L45

Désert, F.-X., Boulanger, F., & Puget, J. L. 1990, *A&A*, 237, 215

D'Hendecourt, L. B. & Léger, A. 1987, *A&A*, 180, L9

Dibben, M. J., Kage, D., Szczepanski, J., Eyler, J. R., & Vala, M. 2001, J. Phys. Chem. A, 105, 6024

Dienes, T., Pastor, S. J., Schürch, S., et al. 1996, Mass Spectrom. Rev., 15, 163

Draine, B. T. 2003, *Annual Review of Astronomy and Astrophysics*, 41, 241

Draine, B. T. & Li, A. 2001, *ApJ*, 551, 807

Draine, B. T. & Li, A. 2007, *ApJ*, 657, 810

Duley, W. W. 2006, *ApJ Letters*, 643, L21

Dunbar, R. C. 1992, Mass Spect. Rev., 11, 309

Ehrenfreund, P., D'Hendencourt, L., Verstraete, L., et al. 1992, *A&A*, 259, 257

Eichkorn, K., Treutler, O., Öhm, H., Häser, M., & Ahlrichs, R. 1995, Chem. Phys. Lett., 242, 652

Ekern, S. P., Marshall, A. G., Szczepanski, J., & Vala, M. 1997, *ApJ Letters*, 488, L39

Ekern, S. P., Marshall, A. G., Szczepanski, J., & Vala, M. 1998, J. Phys. Chem. A, 102, 3498

Flagey, N., Boulanger, F., Verstraete, L., et al. 2006, *A&A*, 453, 969

Frenklach, M. & Feigelson, E. D. 1989, *ApJ*, 341, 372

Geballe, T. R., Joblin, C., D'Hendecourt, L. B., et al. 1994, *ApJ Letters*, 434, L15

Geusic, L., Jarrold, M. F., McIlrath, T. J., Freeman, R. R., & Brown, W. L. 1987, J. Chem. Phys., 86, 3862

Gotkis, Y. & Lifshitz, C. 1992, J. Mass Spectrom., 28, 372

Gotkis, Y., Oleinkova, M., Naor, M., & Lifshitz, C. 1993, J. Phys. Chem., 97, 12282

Goulay, F., Rebrion-Rowe, C., Biennier, L., et al. 2006, J. Phys. Chem. A, 110, 3132

Goulay, F., Rebrion-Rowe, C., Le Garrec, J. L., et al. 2005, J. Chem. Phys., 122, 104308

Grosshans, P., Shields, P., & Marshall, A. G. 1991, J. Chem. Phys., 94, 5341

Guan, S. & Marshall, A. G. 1995, Int. J. Mass Spectrom. Ion Processes, 146-147, 261

Guo, X., Sievers, H. L., & Grutzmacher, H. F. 1999, International journal of mass spectrometry, 185/186/187, 1

Güthe, F., Ding, H., Pino, T., & Maier, J. P. 2001, Chem. Phys., 269, 347

Hager, J. W. & Wallace, S. C. 1988, Anal. Chem., 60, 5

Halasinski, T. M., Salama, F., & Allamandola, L. J. 2005, *ApJ*, 628, 555

Heger, M. L. 1921, Lick. Obs. Bull., 10, 146

Herbig, G. H. 1995, *Annual Review of Astronomy and Astrophysics*, 33, 19

Hirata, S., Lee, T. J., & Head-Gordon, M. 1999, J. Chem. Phys., 111, 8904

Hobbs, L. M., York, D. G., Snow, T. P., et al. 2008, *ApJ*, 680, 1256

Hohenberg, P. & Kohn, W. 1964, Phys. Rev., 136, B864

Hu, Q., Noll, R. J., Li, H., et al. 2005, Journal of mass spectrometry, 40, 430

Huang, J. Y., Tiedemann, P. W., Land, D. P., McIver, R. T. J., & Hemminger, J. C. 1994, Int. J. Mass Spectrom. Ion. Proc., 134, 11

Hudgins, D. M. & Allamandola, L. J. 1999, *ApJ*, 513, L69

Hudgins, D. M. & Allamandola, L. J. 2000, J. Phys. Chem., 104, 3655

Iglesias-Groth, S., Manchado, A., García-Hernández, D. A., González Hernández, J. I., & Lambert, D. L. 2008, *ApJ Letters*, 685, L55

Jenniskens, P. & Désert, F.-X. 1994, *A&A Suppl.*, 106, 39

Joblin, C. 2003, in SF2A-2003: Semaine de l'Astrophysique Francaise, ed. F. Combes, D. Barret, T. Contini, & L. Pagani, 175

Joblin, C., Armengaud, M., Frabel, P., & Boissel, P. 2009, in preparation

Joblin, C., Boissel, P., Leger, A., D'Hendecourt, L., & Defourneau, D. 1995, *A&A*, 299, 835

Joblin, C., D'Hendecourt, L., Leger, A., & Defourneau, D. 1994, *A&A*, 281, 923

Joblin, C., Leger, A., & Martin, P. 1992, *ApJ Letters*, 393, L79

Joblin, C., Tielens, A. G. G. M., Allamandola, L. J., & Geballe, T. R. 1996a, *ApJ*, 458, 610

Joblin, C., Tielens, A. G. G. M., Geballe, T. R., & Wooden, D. H. 1996b, *ApJ Letters*, 460, L119+

Joblin, C., Toublanc, D., Boissel, P., & Tielens, A. G. G. M. 2002, Mol. Phys., 100, 3595

Jochims, H. W., Baumgärtel, H., & Leach, S. 1999, *ApJ*, 512, 500

Jochims, H. W., Ruhl, E., Baumgartel, H., Tobita, S., & Leach, S. 1994, *ApJ*, 420, 307

Jolibois, F., Klotz, A., Gadéa, F. X., & Joblin, C. 2005, *A&A*, 444, 629

Jones, R. O. & Gunnarsson, O. 1989, Rev. Mod. Phys., 61, 689

Jones, R. O. & Seifert, G. 1999, J. Chem. Phys., 110, 5189

Keheyan, Y. 2001, Chem. Phys. Lett., 340, 405

Kim, H. & Saykally, R. J. 2003, Rev. Sci. Instrum., 74, 2488

Kohn, W. & Sham, L. J. 1965, Phys. Rev., 140, A1133

Kokkin, D. L., Troy, T. P., Nakajima, M., et al. 2008, *ApJ Letters*, 681, L49

Kroto, H. W. & Jura, M. 1992, *A&A*, 263, 275

Kurtz, J. 1992, *A&A*, 255, L1

Le Page, V., Keheyan, Y., Snow, T. P., & Bierbaum, V. M. 1999, J. Am. Chem. Soc., 121, 9435

Le Page, V., Snow, T. P., & Bierbaum, V. M. 2001, *ApJ Suppl.*, 132, 233

Le Page, V., Snow, T. P., & Bierbaum, V. M. 2003, *ApJ*, 584, 316

Ledford, E. B. J., Rempel, D. L., & Gross, M. L. 1984, Anal. Chem., 56, 2744

Lee, S., Gotts, N., von Helden, G., & Bowers, M. T. 1997, J. Phys. Chem. A, 101, 2096

Léger, A. & D'Hendecourt, L. 1985, *A&A*, 146, 81

Léger, A., D'Hendecourt, L., & Défourneau, D. 1989, *A&A*, 216, 148

Léger, A., D'Hendecourt, L., & Défourneau, D. 1995, *A&A*, 293, L53

Léger, A. & Puget, J. L. 1984, *A&A*, 137, L5

Lehman, T. A. & Bursey, M. M. 1976, Ion Cyclotron Resonance Spectrometry (Wiley, New York)

Ling, Y. & Lifshitz, C. 1995, J. Phys. Chem., 99, 11074

Ling, Y. & Lifshitz, C. 1997, J. Mass Spectrom., 32, 1219

Ling, Y. & Lifshitz, C. 1998, J. Phys. Chem. A, 102, 708

Maier, J. P. 1998, J. Phys. Chem. A, 102, 3462

Maier, J. P. & Turner, D. W. 1972, Discuss. Faraday Soc., 54, 149

Makarov, A. 2000, Anal. Chem., 72, 1156

Malloci, G., Mulas, G., Cecchi-Pestellini, C., et al. 2008, in IAU Symposium, Vol. 251, IAU Symposium, ed. S. Kwok & S. Sandford, 75–76

Marshall, A. G., Hendrickson, C. L., & Jackson, G. S. 1998, Mass Spectrometry Reviews, 17, 1

Marshall, A. G. & Schweikhard, L. 1992, Int. J. Mass Spectrom. Ion. Proc., 118, 37

Marshall, A. G., Wang, T. C., & Wang, J. R. 1985, J. Am. Chem. Soc., 107, 7893

Mattioda, A. L., Hudgins, D. M., & Allamandola, L. J. 2005, *ApJ*, 629, 1188

Mattioda, A. L., Ricca, A., Tucker, J., Bauschlicher, C. W., & Allamandola, L. J. 2009, *AJ*, 137, 4054

McKee, C. F. & Ostriker, J. P. 1977, *ApJ*, 218, 148

Merrill, P. 1934, Publ. Astron. Soc. Pac., 46, 206

Mulas, G., Malloci, G., Joblin, C., & Toublanc, D. 2006, *A&A*, 460, 93

Nguyen-Thi, V.-O., Désesquelles, P., & Bréchignac, P. 2006a, J. Phys. Chem. A, 110, 5599Ð5606

Nguyen-Thi, V.-O., Désesquelles, P., Douin, S., & Bréchignac, P. 2006b, J. Phys. Chem. A, 110, 5592Ð5598

Nikolaev, E. N., Miluchihin, N. V., & Inoue, M. 1995, Int. J. Mass Spectrom. Ion. Proc., 148, 145

Omont, A. 1986, *A&A*, 164, 159

Oomens, J., Sartakov, B. G., Meijer, G., & von Helden, G. 2006, Int. J. Mass Spectrom., 254, 1

Oomens, J., Sartakov, B. G., Tielens, A. G. G. M., Meijer, G., & von Helden, G. 2001, *ApJ Letters*, 560, L99

Oomens, J., Tielens, A. G. G. M., Sartakov, B. G., von Helden, G., & Meijer, G. 2003, *ApJ*, 591, 968

Oomens, J., van Roij, A. J. A., Meijer, G., & von Helden, G. 2000, *ApJ*, 542, 404

Pech, C. 2001, PhD thesis, Université Toulouse III - Paul Sabatier

Perdew, J. P. 1986, Phys. Rev. B, 33, 8822

Pety, J., Teyssier, D., Fossé, D., et al. 2005, *A&A*, 435, 885

Pilleri, P., Herberth, D., Giesen, T. F., et al. 2009, *MNRAS*, 397, 1053

Pino, T., Boudin, N., & Bréchignac, P. 1999, J. Chem. Phys., 111, 7337

Pino, T., Bréchignac, P., Dartois, E., Demyk, K., & d'Hendecourt, L. 2001, Chem. Phys. Lett., 339, 64

Pino, T., Parneix, P., Calvo, F., & Bréchignac, P. 2007, J. Phys. Chem. A, 111, 4456

Pozniak, B. P. & Dunbar, R. C. 1997, Int. J. Mass Spectrom. Ion Processes, 165/166, 299

Rapacioli, M., Calvo, F., Joblin, C., et al. 2006, *A&A*, 460, 519

Rapacioli, M., Joblin, C., & Boissel, P. 2005, *A&A*, 429, 193

Rolland, D., Specht, A. A., & W., B. M. 2003, Chem. Phys. Lett., 373, 292

Romanini, D., Biennier, L., & F., S. 1999, Chem. Phys. Lett., 303, 165

Romanini, D., Kachanov, A. A., Sadeghi, N., & Stoeckel, F. 1997, Chem. Phys. Lett., 264, 316

Ruehl, E., Price, S. D., & Leach, S. 1989, J. Phys. Chem., 93, 6312

Ruiterkamp, R., Halasinski, T., Salama, F., et al. 2002, *A&A*, 390, 1153

Runge, E. & Gross, E. K. U. 1984, Phys. Rev. Lett., 52, 997

Salama, F. 2008, in IAU Symposium, Vol. 251, IAU Symposium, ed. S. Kwok & S. Sandford, 357–366

Salama, F. & Allamandola, L. J. 1991, J. Chem. Phys., 94, 6964

Salama, F. & Allamandola, L. J. 1992, Nature, 358, 42

Salama, F., Bakes, E. L. O., Allamandola, L. J., & Tielens, A. G. G. M. 1996, *ApJ*, 458, 621

Salama, F., Galazutdinov, G. A., Krełowski, J., Allamandola, L. J., & Musaev, F. A. 1999, *ApJ*, 526, 265

Salama, F., Joblin, C., & Allamandola, L. J. 1994, J. Chem. Phys., 101, 10252

Savage, B. D. & Mathis, J. S. 1979, *Annual Review of Astronomy and Astrophysics*, 17, 73

Schafer, A., Horn, H., & Ahlrichs, R. 1992, J. Chem. Phys., 97, 2571

Schafer, A., Huber, C., & Ahlrichs, R. 1994, J. Chem. Phys., 100, 5829

Schmidt, W. 1977, J. Chem. Phys., 66, 828

Schutte, W. A., Tielens, A. G. G. M., & Allamandola, L. J. 1993, *ApJ*, 415, 397

Scott, A., Duley, W. W., & Pinho, G. P. 1997, *ApJ Letters*, 489, L193

Sellgren, K. 1984, *ApJ*, 277, 623

Seung-Jin, H. & Seung, K. S. 1997, J. Am. Soc. Mass Spectrom., 8, 319

Shan, J., Suton, M., & Lee, L. C. 1991, *ApJ*, 383, 459

Shelimov, K. B., Hunter, J. M., & Jarrold, M. F. 1994, International journal of mass spectrometry and ion processes, 138, 17

Shushan, B. & Boyd, R. K. 1980, Org. Mass Spectrom., 15, 445

Snow, T. P. & McCall, B. J. 2006, *Annual Review of Astronomy and Astrophysics*, 44, 367

Stein, S. E. & Rabinovitch, B. S. 1973, *Journal of Chemical Physics*, 58, 2438

Sukhorukov, O., Staicu, A., Diegel, E., et al. 2004, Chem. Phys. Lett., 386, 259

Szczepanski, J., Roser, D., Personette, W., et al. 1992, J. Phys. Chem., 96, 7876

Szczepanski, J. & Vala, M. 1993, *ApJ*, 414, 646

Szczepanski, J., Wehlburg, C., & Vala, M. 1995, Chem. Phys. Lett., 232, 221

Tan, X. & Salama, F. 2006, Chem. Phys. Lett., 422, 518

Teyssier, D., Fossé, D., Gerin, M., et al. 2004, *A&A*, 417, 135

Tielens, A. G. G. M. 2005, The Physics and Chemistry of the Interstellar Medium (The Physics and Chemistry of the Interstellar Medium, by A. G. G. M. Tielens, Cambridge, UK: Cambridge University Press, 2005.)

Tielens, A. G. G. M. & Snow, T. P., eds. 1995, Astrophysics and Space Science Library, Vol. 202, The diffuse interstellar bands

Vala, M., Szczepanski, J., Pauzat, F., et al. 1994, J. Phys. Chem., 98, 9187 van der Zwet, G. P. & Allamandola, L. J. 1985, *A&A*, 146, 76

Verstraete, L. 1990, PhD thesis, Université Paris 7

Verstraete, L., Leger, A., D'Hendecourt, L., Defourneau, D., & Dutuit, O. 1990, *A&A*, 237, 436

von Helden, G., Hsu, M. T., Gotts, N. G., Kemper, P. R., & Bowers, M. T. 1993, Chem. Phys. Lett., 204, 15

Vosko, S., Wilk, L., & Nusair Can., M. 1980, Can. J. Phys., 58, 1200

Wang, X., Becker, H., Hopkinson, A. C., et al. 1997, I. J. M. S. & I. P., 161, 69

Weisman, J. L., Lee, T. J., Salama, F., & Head-Gordon, M. 2003, *ApJ*, 587, 256

List of Acronyms

Acronym	**Definition**
AIB	Aromatic Infrared Band
BG	Big Grain
CID	Collision Induced Dissociation
CNM	Cold Neutral Medium
CRDS	Cavity Ring-Down Spectroscopy
CRESU	Cinétique de Réaction en Ecoulement Supersonique Uniforme
DIB	Diffuse Interstellar Band
FELIX	Free Electron Laser for Infrared Experiment
FT	Fourier Transform
FUV	Far UltraViolet
FWHM	Full Width at Half Maximum
HIM	Hot Ionised Medium
IC	Internal Conversion
ICR	Ion Cyclotron Resonance
IR	InfraRed
ISM	Interstellar Medium
IVR	Internal Vibrational Redistribution
MIS	Matrix Isolation Spectroscopy
MPD	MultiPhoton Dissociation
MS	Mass Spectrometry
OPO	Optical Parametric Oscillator
PAH	Polycyclic Aromatic Hydrocarbon
PES	PhotoElectron Spectroscopy
PDR	PhotoDissociation Region
PEPICO	PhotoElectron PhotoIon Coincidence
PIRENEA	Piège à Ions pour la Recherche et l’Etude de Nouvelles Espèces Astrochimiques
REMPI	Resonantly Enhanced Multi-Photon Ionization

SIFT	Selected Ion Flow Tube
SVP	Split Valence Polarisation
SWIFT	Stored Waveform Inverse Fourier Transform
TD- DFT	Time-Dependent Density Functional Theory
TOF	Time Of Flight
TPIMS	Time-Resolved PhotoIonisation Mass Spectrometry
TRPD	Time-Resolved PhotoDissociation
UIR	Unidentified InfraRed
UV	UltraViolet
VSG	Very Small Grain
WIM	Warm Ionised Medium
WNM	Warm Neutral Medium

Abstract

One of the interesting discoveries of infrared astronomy is the ubiquitous presence of polycyclic aromatic hydrocarbons (PAHs) in interstellar and circumstellar environments. These macromolecules play a key role in the physics and chemistry of the interstellar medium (ISM). However, despite a lot of observational, laboratory and modelling studies, no definite identification of individual species has been possible yet. The identification process requires both an understanding of the nature of these large carbon molecules, which is driven by their formation and further evolution under the action of UV photodissociation and chemistry, and the search for specific spectroscopic fingerprints. These subjects are experimentally approached in this work, taking advantage of the PIRENEA set-up dedicated to astrochemistry.

In the first part of this thesis a study of the photodissociation cascade of several medium-sized PAHs isolated in the ion trap of PIRENEA is performed. The aim of this study is to provide information on both destruction of PAHs by UV radiation and formation channels of small hydrocarbons and carbon clusters through destruction of a larger precursor. An inventory of the formed species is made and the main fragmentation patterns are identified.

The second part of the thesis focuses on the visible spectroscopy of different PAH cations and dehydrogenated derivatives. Multiphoton dissociation spectroscopy is performed to measure the electronic spectra of these species. The experimental results are interpreted with the help of theoretical spectra calculated in the frame of the time-dependent density functional theory and laboratory data obtained in rare-gas matrices. The photophysics of the laser-irradiated ions is also modelled to derive, for some of the studied species, the absorption cross-sections of the measured electronic transitions. The purpose of this second study is to obtain gas-phase spectroscopic data on different ionised PAHs and derivatives, that can be useful for the pre-selection of the most promising candidates for some of the diffuse interstellar bands, a set of absorption bands observed in the ISM since almost a century but still unidentified.

Résumé

Une des découvertes majeures faites par l'astronomie infrarouge est la présence de molécules polycycliques aromatiques hydrogénées (PAH) dans les milieux interstellaires et circumstellaires. Ces macromolécules jouent un rôle essentiel dans la physique et chimie du milieu interstellaire (MIS). Cependant aucune espèce individuelle n'a pu être identifiée jusqu'à présent malgré de nombreuses études observationnelles, des travaux de modélisation et des expériences dédiées en laboratoire.

Progresser dans cette identification nécessite de caractériser la nature de ces PAH qui est conditionnée par les processus de formation et d'évolution par photodissociation UV et réactivité chimique. Il s'agit ensuite d'obtenir des signatures spectroscopiques spécifiques. Ces sujets sont abordés expérimentalement dans ce travail en utilisant l'expérience PIRENEA dédiée à l'étude de la physico-chimie interstellaire.

Dans la première partie de cette thèse, nous avons mesuré la photodissociation de ces espèces isolées dans le piège à ions de PIRENEA. L'objectif scientifique de cette étude est d'apporter des informations sur le processus de destruction des PAH par irradiation UV-visible et d'évaluer leur contribution à la formation de petits hydrocarbures et d'agrégats carbonés dans le MIS. Un inventaire des espèces produites par photodissociation a été fait pour chacune des molécules considerées et les principales voies de dissociation ont été identifiées.

Dans la deuxième partie du travail, je présenterai une étude sur la spectroscopie visible de différents cations PAH et dérivés déshydrogénés réalisée par dissociation multiphotonique. Les résultats expérimentaux ont été comparés à des spectres théoriques obtenus avec un modèle de la théorie de la fonctionnelle de la densité et à des données spectroscopiques mesurées en matrices de gaz rare. Un modèle décrivant la photophysique des ions a été utilisé pour déterminer les sections efficaces d'absorption de certaines espèces étudiées. Ces données peuvent être utiles pour la pré-sélection de candidats aux bandes diffuses interstellaires, bandes qui sont observées en absorption dans le MIS depuis près d'un siècle et qui restent non identifiées.